CHAPTER 7

MATERIALS CHARACTERIZATION

Thus far, we have focused on the relationship between the structure of a material and its properties/applications. However, we have not yet focused on how one is able to determine the structure and composition of materials. That is, when a material is fabricated in the lab, how are we able to assess whether our method was successful? Depending on the nature of the material being investigated, a suite of techniques may be utilized to assess its structure and properties. Whereas some techniques are qualitative, such as providing an image of a surface, others yield quantitative information such as the relative concentrations of atoms that comprise the material. Recent technological advances have allowed materials scientists to accomplish something that was once thought to be impossible: to obtain actual two-dimensional/three-dimensional images of atomic positions in a solid, in real time. It should be noted that the sensitivity of quantitiative techniques also continues to be improved, with techniques now being able to easily measure parts per trillion (ppt) concentrations of impurities in a bulk sample.

This chapter will focus on the most effective and widely used techniques available to characterize solid-state compounds. The primary objective of this chapter is to provide a practical description of the methods used to characterize a broad range of materials. Rather than focusing on the theoretical aspects of each technique, which may be found in many other textbooks (see "Further Reading" section), our treatment will focus on method suitabilities, sample preparation, and anticipated results. In this manner, you will be well informed regarding the best method to use for a particular material. Since techniques such as solution-phase nuclear magnetic resonance (NMR) and infrared spectroscopy (IR) are used throughout undergraduate courses, the background of these methods will not be provided in this textbook. Likewise, it is beyond the scope of this chapter to provide detailed background in optics, electronics, and physical chemistry concepts that underly most of the techniques described herein. For this information, the reader is referred to the "Further Reading" section at the end of this chapter.

7.1. OPTICAL MICROSCOPY

Of the many techniques available for the analysis of solid materials, perhaps the simplest is optical microscopy. Two modes of optical microscopy are typically

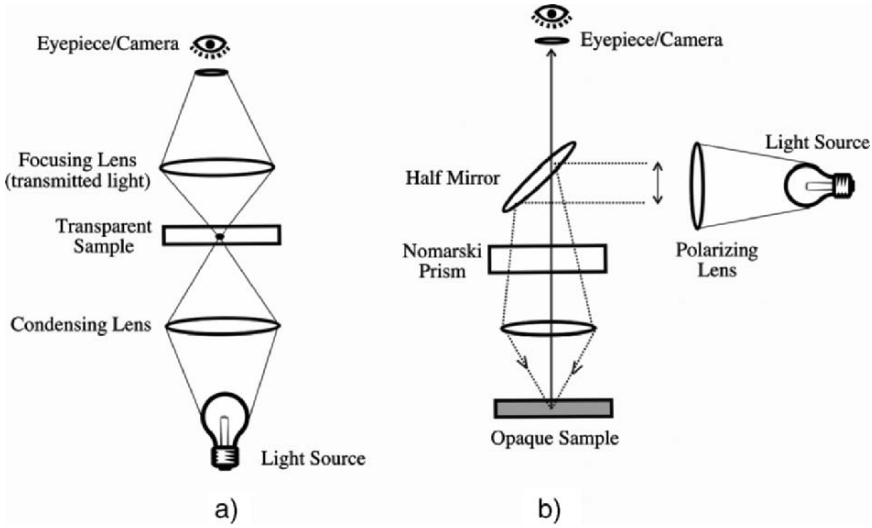

Figure 7.1. Schematic of the components of (a) transmitted light optical microscope and (b) reflected light optical microscope.

employed, based on the measurement of transmitted or reflected light, from a transparent or opaque sample, respectively (Figure 7.1). Often, a microscope is fitted with both modes, allowing one to analyze both types of samples. Most of the solid-state materials discussed thus far are nontransparent in their as-grown/as-deposited states. Further, it is usually difficult to prepare thin cross sections for transmission microscopy. Hence, materials scientists typically employ the reflection mode, also known as episcopic light differential interference contrast (DIC) microscopy.[1] This technique is useful for imaging of a variety of reflective samples including minerals, metals, semiconductors, glasses, polymers, and composites. The semiconductor industry relies heavily on reflective DIC imaging for quality assessment of computer chip components.

Surface artifacts such as depressions and particulates create optical path differences in the reflected beam. Formation of the final image is the result of interference between two distinct wave fronts that reach the image plane slightly out of phase with each other. Unlike the situation with transmitted light and semitransparent phase specimens, the image created in reflected light DIC can often be interpreted as a true three-dimensional representation of the surface geometry, provided a clear distinction can be realized between raised and lowered regions in the specimen. Oftentimes, the reflected wave fronts emanating from the sample are separated by only fractions of a micrometer, which is much less than the resolution of the objective.

The ability to discern fine details within a magnified image is referred to as the *resolution* of a microscope. Since light is used as the illumination source in optical microscopy, the resolution is expressed in the same units as the wavelength of

light (nm). The theoretical resolution, R, of any optical system may be calculated using Abbe's equation (Eq. 1):

$$(1) \qquad R = \frac{0.61\lambda}{\eta(\sin\theta)},$$

where

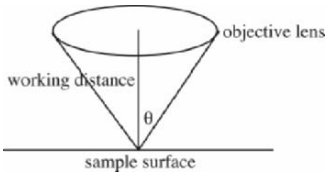

The denominator of Eq. 1 represents the numerical aperature (NA) of the objective lens, related to its light gathering ability. Other primary factors that influence the resolution of a lens is the wavelength of light used, the index of refraction (η) of the environment surrounding the lens (*e.g.*, 1.00 for air), and the angle of illumination (θ).

Examining the above equation, one can see that a resolution limit will be reached using visible light (350–700 nm) as the illumination source. That is, using high numerical aperatures (*e.g.*, 1.3–1.4 for oil-immersion lenses where $\eta = 1.5$), the theoretical resolution using polychromatic visible light (*ca.* 500 nm) is on the order of 220 nm. Hence, any sample features that are less than 220 nm apart from one another will appear blurry. It should be noted that the calculated resolution represents the best possible cutoff for clear discernment of small features. In practice, the observed resolution is often worse than the theoretical value, depending on the degree of optical aberrations that are inherent in the lens.

It may be seen by Eq. 1 that higher spatial resolutions (*i.e.*, smaller R values) are possible through use of shorter wavelengths. To illustrate this concept, subsequent sections of this chapter will examine the high resolutions inherent in microscopes that use an electron beam rather than visible light. However, we first must ask ourselves whether it is possible to improve the resolution limits of optical microscopy. If this is possible, the cost of such a modification would be far less than the price of electron microscopes (currently \$600 K–\$1.5 M).

In the late 1920s, Edward H. Synge published a series of articles that conceptualized the idea of an "ultrahigh resolution" optical microscope.[2] His original idea proposed using a screen with an aperature of dimensions much smaller than wavelength of the illuminating source. Upon irradiating the screen with a high-intensity light source, the light is confined to the dimensions of the hole. If this hole is placed in close proximity (nanometer regime) to the sample surface, the light emerging from the aperture could be used to image a specimen before it had time to spread out. By comparison, the distance between the light source and sample in conventional optical microscopy is on the order of millimeters. Not unlike other visionary ideas ahead of

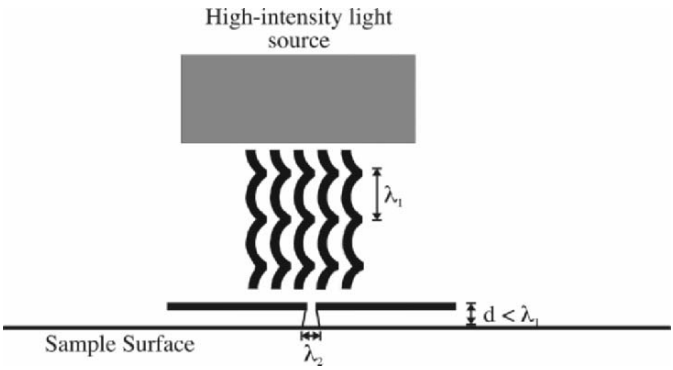

Figure 7.2. Schematic of operating principle of near-field scanning optical microscopy (NSOM). The resulting wavelength of light impinging on the sample (λ_2) has a wavelength much smaller than the illuminating source, resulting in much higher resolution.

their time, the technical difficulties associated with Synge's idea were only recently overcome at IBM in the mid-1980s, which marked the rediscovery of the technique now referred to as near-field scanning optical microscopy (NSOM, Figure 7.2).[3]

A variety of apertures have been used to deliver nanometer-sized spots of light. While early NSOM tips were fabricated out of etched quartz crystals and micropipettes, tapered optical fibers with tip diameters of *ca.* 100 nm are now typically used. A metallic thin film such as aluminum is usually applied around the sides of the tapered region of the NSOM tip to focus the light toward the sample. For optical fibers, the numerical aperature is related to the difference in the indices of refraction of the cladding and core (Eq. 2):

$$\text{NA} \propto \sqrt{(\eta_{\text{core}})^2 - (\eta_{\text{cladding}})^2}. \quad (2)$$

In order to obtain high-resolution optical images with NSOM, the tip must be stabilized within a few nanometers of the sample surface during scanning. Techniques to precisely position the tip above the sample were developed by researchers in 1992, resulting in more applications for both imaging and topographic profiling of surfaces. This latter capability will be discussed in more detail later in this chapter when discussing scanning probe microscopy (SPM).

7.2. ELECTRON MICROSCOPY

Although optical microscopy may be extended into the nanoregime, other techniques must be used to clearly discern components below 100 nm. Indeed, the current "nanotechnology revolution" that we are experiencing would not have been possible if there were not suitable techniques in order to characterize nanomaterials. As we saw in the previous section, in order to improve resolution, we must use source radiation with as small a wavelength as possible.

Louis DeBroglie was the first to assert that matter, like light, could be described as having both particle and wave characteristics (Eq. 3). However, the application of this equation for a macroscopic item such as a golf ball in flight,[4] predicts a wavelength that is too small to be meaningful (Eq. 4). By comparison, subatomic particles have wavelengths comparable to the size of an atom. In particular, electrons that are accelerated in a potential, V, have quantifiable wavelengths[5]; for example, electrons accelerated at 100 kV have a wavelength of 0.037 Å (Eq. 5). This is significantly shorter than the wavelengths of high-energy radiation sources such as X-rays (*e.g.*, 1.54 Å for Cu Kα X-rays), or neutrons (*ca.* 1 nm). Though neutron microscopes have recently been demonstrated,[6] X-ray microscopes are not possible due to the lack of suitable refracting lenses for X-rays. However, we will see later on that X-rays are instrumental for the chemical analysis of a surface:

$$\lambda = \frac{h}{mv}, \tag{3}$$

$$\frac{6.626 \times 10^{-34}\,\mathrm{J\,s}}{(0.045\,\mathrm{kg})(41\,\mathrm{m\,s^{-1}})} = 3.59 \times 10^{-34}\,\mathrm{m}, \tag{4}$$

$$\lambda = \frac{12.3\,\text{Å}}{\sqrt{V + \frac{V^2}{1\times10^6}}}. \tag{5}$$

The ability to focus the extremely small incident wavelengths of energetic electrons results in an unprecedented spatial resolution compared to optical based microscopy techniques (Figure 7.3). Since the resolution of our eyes is on the order of 0.1 mm, in order for us to observe these features, an appropriate level of magnification must be used. That is, for the increasingly greater resolution capabilities of modern scanning electron microscope (SEM) and transmission electron microscope (TEM) instruments, the sample must be magnified by *ca.* 100–300 K and 1.5–2 M times, respectively (Figure 7.4). However, it should be noted that although the wavelength of electrons are *ca.* 100,000 times smaller than visible light, the resolving power of electron microscopes are only on the order of 1,000 times greater than light microscopes, due to lens aberrations (especially spherical aberration).[7]

Images obtained from electron microscopy are due to the nature/degree of electron scattering from the constituent atoms of the sample. Table 7.1 provides a comparison between electron, X-ray, and neutron sources, pertaining to their utility

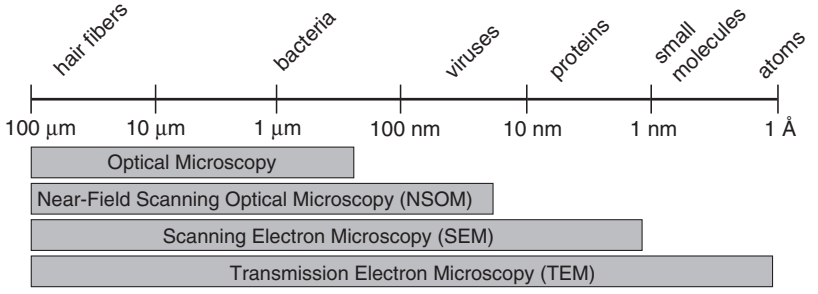

Figure 7.3. Comparison of the characterization size regimes for optical and electron microscopy.

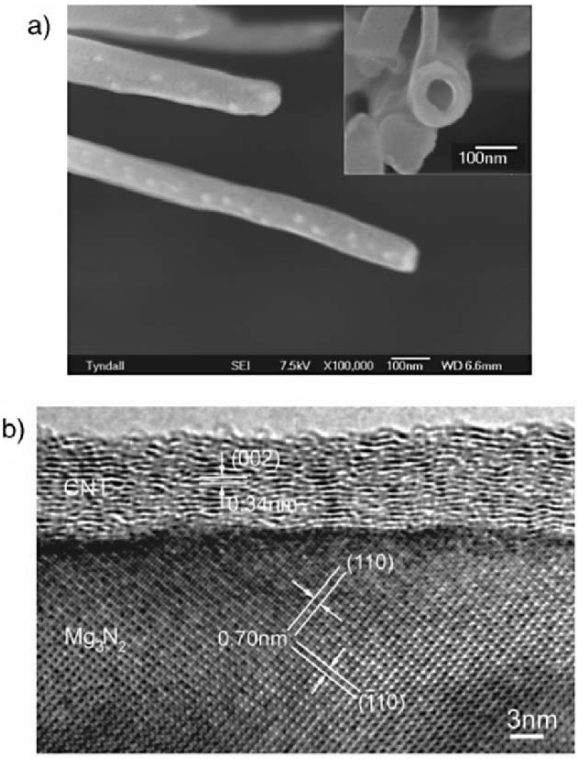

Figure 7.4. High-resolution (HR) electron micrographs. Shown is (a) an SEM image of vanadium oxide nanotubes at a magnification of 100,000×[8] and (b) a TEM image of the interface between a Mg_3N_2 nanowire and a graphitic carbon coating at a magnification of *ca.* 2,000,000×.[9]

Table 7.1. Comparative Characteristics of Energetic Radiation Sources

Source	Brightness[a] (particles cm^{-2} eV^{-1} $steradian^{-1}$)	Elastic Mean Free Path[b] (Å)	Absorption Length[c] (Å)	Minimum Probe Size[d] (Å)
Neutrons	1×10^{24}	1×10^{8}	1×10^{9}	1×10^{7}
X-rays	1×10^{26}	1×10^{4}	1×10^{6}	1×10^{3}
Electrons	1×10^{29}	1×10^{2}	1×10^{3}	1

Data from http://ncem.lbl.gov/team/team_background.htm
[a]Related to the number of particles and the range of incident angles that irradiate a sample.
[b]Related to the distance a particle travels in a solid before elastically colliding with constituent atoms.
[c]Related to the distance a particle travels in a solid before its energy is absorbed through interactions with constituent atoms and electrons.
[d]Related to the minimum diameter of the source that is used to generate the radiation.

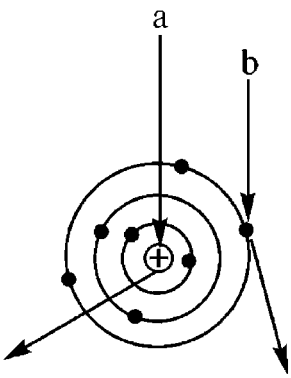

Figure 7.5. Schematic of specific interactions between the electron beam and sample atom. Shown are (a) an elastically scattered electron and (b) an inelastically scattered electron.

for scattering applications. Electrons are much less penetrating than X-rays, and are readily absorbed by air, dictating the use of ultrahigh vacuum (UHV) environments. Since the mass of an electron is 1,000 times smaller than the lightest nucleus, electrons are scattered much more intensely than X-rays or highly penetrating neutrons. This results in high sensitivity from the interaction of electrons with extremely small samples.

There are two types of scattering interactions that are possible when an electron beam impinges on atoms of the sample (Figure 7.5). Interaction between the electron source and atomic nuclei gives rise to *elastic scattering*, which results in a large-angle deflection of the electron beam with little or no energy loss. By comparison, electron–electron interactions between the source and electron clouds of individual atoms cause small-angle deflections with a significant loss of energy, known as *inelastic scattering*. It should be noted that there is a finite probability that the electrons may continue their original trajectory through the atomic structure without scattering. In particular, this is commonly observed with molecules containing light atoms such as H, Li, B, *etc*. As you would expect, a solid consisting of a high density of large atoms such as metallic solids would result in shorter elastic mean free paths, and stronger elastic scattering interactions with incident electrons. By comparison, organic solids such as polyethylene would primarily exhibit inelastic scattering with an electron source.

There are two instruments that are used for electron imaging: TEM and SEM. As the name implies, the transmission mode measures the intensity from an electron source after it has passed through a transparent sample (Figure 7.6a). In contrast, SEM features the scanning of an electron beam over selected regions of an opaque sample (Figure 7.6b).

The basic principles that govern electron microscopy are analogous to optical microscopy. Whereas optical microscopes use light and optical lenses to illuminate and magnify the sample, electron microscopes utilize high-energy electrons and electromagnetic lenses. There are two types of lenses in electron microscopes (see

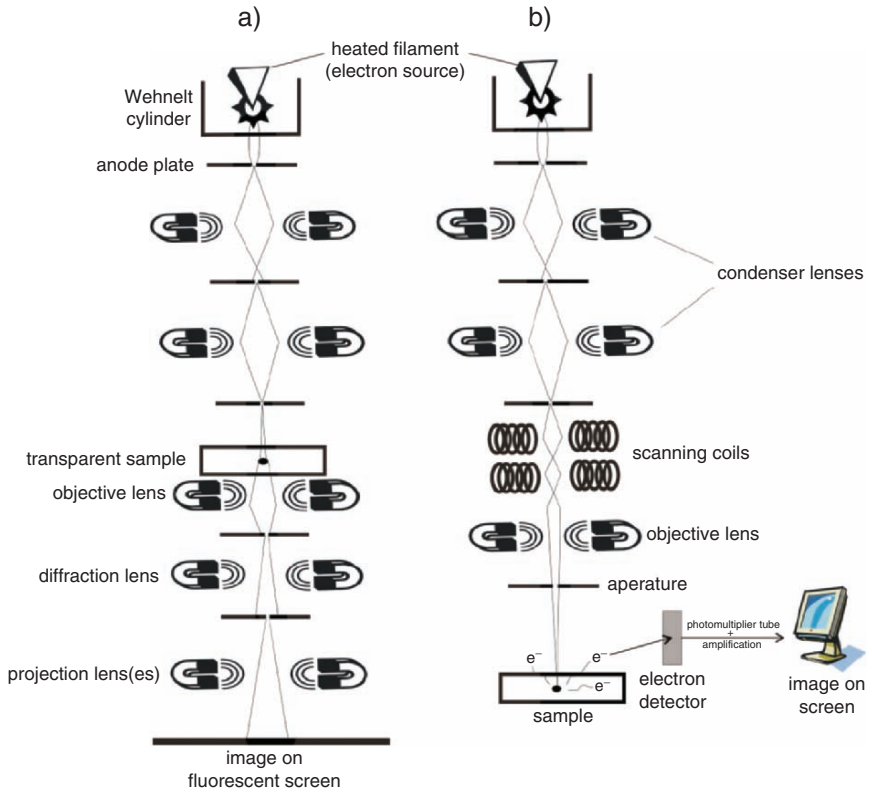

Figure 7.6. Schematic of the major components of (a) transmission electron microscope (TEM) and (b) scanning electron microscope (SEM). Note: stigmator coils are also associated with the lens(es) that reduce beam astigmatism, thereby improving image distortion and resolution. For TEM, the image is shown to be projected onto a viewing screen. This screen is coated with phosphorescent particles such as ZnS and CdS that emit visible light when struck by electrons (hard copies of the image may also be transferred to photographic plates *via* silver halide emulsions). However, modern TEM instruments do not require photographic development, as digital images are observed directly on computer monitors, in real time.

below); TEM has an additional lens, the projector lens, which is used to project an amplified copy of the image onto a screen:

(i) *Condenser* – used to control the illumination of the sample through concentration of the electron beam generated from the source.
(ii) *Objective* – used to magnify the sample (in TEM, the sample is inserted into the objective lens).
(iii) *Projector* – used to project an amplified copy of the image onto a screen (photographic plate, computer screen, fluorescent screen, CCD camera/monitor).

The heart of any electron microscope is the electron source, or gun. In fact, the electron gun within microscopes is identical to that operating within modern televisions. Behind the TV monitor lays a cathode ray tube (CRT), containing a set

of three tungsten filaments. The electrons generated from these filaments are accelerated toward an anode that is coated with phosphor particles, which emit either red, green, or blue light when struck with electrons. This light is focused onto individual pixels that comprise the monitor; if you look close at a television screen, you may notice the millions of tiny dots that comprise individual images. The picture we see on our monitors is a result of the electron guns being scanned sequentially from left to right in a fraction of a second, a process known as *rastering*. This is the exact mode that is operable in SEMs and scanning transmission electron microscopes (STEM), where the focused electron beam is allowed to scan across selected regions of a sample.

Electrons are generated by passing high currents through tungsten or crystalline LaB_6 (or CeB_6) filaments, resulting in temperatures on the order of 2,700–2,900 K or 1,500 K, respectively. The thermal release of electrons at the Fermi level of the material is known as *thermionic emission*, and may only occur once the energy exceeds the work function of the material (4.7 and 2.7 eV for W and LaB_6, respectively). Saturation of the filament occurs when further heating does not increase the number electrons being emitted. Electrons ejected from the filament cathode are focused by a negatively charged Wehnelt cylinder, and drawn toward a positively charged anode plate containing a small aperature (Figure 7.6). The electrons that escape through the pinhole are directed down the column toward the sample. The voltage difference between the filament and the anode plate is referred to as the *accelerating voltage*. This value is directly proportional to the energy of the electron beam that is directed down the column. Whereas the voltage range for SEM is *ca.* 200 V–40 kV, TEMs feature much higher accelerating voltages, ranging from 60 to 400 kV. All electron microscopes must be operated under extremely high vacuum conditions (*ca.* 10^{-6}–10^{-9} Torr), which provides an insulating medium between the cathode and anode, prolongs the lifetime and efficiency of the gun, and allows for sharper beam focusing. In general, the characteristics of an electron gun may be optimized by varying four components: the distance from the filament to the opening of the Wehnelt cylinder, the temperature of the filament, the negative bias of the Wehnelt cylinder with respect to the cathode, and the brightness of the beam.

Lanthanum hexaboride crystal filaments yield a brightness *ca.* 10 times greater than W, with a smaller spot size. This allows for imaging at very low accelerating voltages without a loss of resolution – of importance for beam-sensitive samples. Due to the small spot size, the beam from a LaB_6 source is highly monochromatic, which increases the overall resolution (*i.e.*, less chromatic aberrations). Interestingly, LaB_6 filaments employ the (100) face due to its relatively low work function.[10] The preferential release of electrons from this crystal face is likely due to the dipole existing between the positively charged metal atoms at the crystal surface, and the underlying layer of boride octahedra (Figure 7.7). A high vacuum must be used to prevent oxidation of the crystal surface; adsorption of oxygen raises the work function of LaB_6 to 4.0 eV.[11]

It should be noted that the work function of structural alloys is always less than the work function of the isolated component metals. For instance, the work functions of B and La are 4.5 and 3.3 eV, respectively – much higher than LaB_6. The mechanisms

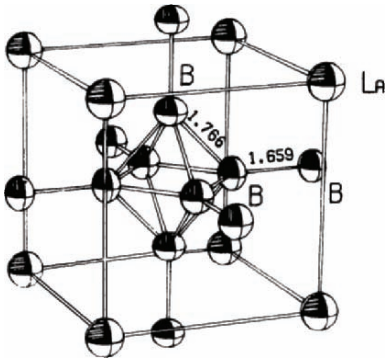

Figure 7.7. Unit cell of LaB_6. Thermal vibration ellipsoids are also shown, illustrating a significant aniostropy in the thermal vibrations of the B atoms. Reproduced with permission from Lundstrom, T. *Pure Appl. Chem.* **1985**, *57*, 1383. Copyright 1985 IUPAC.

Table 7.2. Comparison of Various Electron Sources

	Spot Size (nm)	E Spread (eV)	Brightness ($A\,cm^{-2}\,SR^{-1}$)	Stability (% RMS)	Lifetime (h)
Field Emission					
Schottky					
ZrO_2/W(100)	>0.2	0.35–0.7	5×10^8	<1	>1 year
Cold					
W(310)	>0.2	0.3–0.7	1×10^9	4–6	>1 year
Conventional					
LaB_6	>2	1.5	1×10^7	<1	500
W	>50	3	1×10^6	<1	100

responsible for the reduction of the work function are not completely understood, although it must depend on the three-dimensional arrangement and orbital overlap of electron rich/deficient atoms or ions near the surface of the solid. Once this mechanism is deciphered, many more materials will be isolated as effective candidates for electron emission sources.

In order to increase the intensity and focus of electrons, a *field emission* source may be used. This consists of a single crystal tungsten or $LaB_6(100)$ wire that is sharpened to a tip diameter of *ca.* 100 nm − 1 μm. For crystalline tungsten, the axis is suitably aligned with respect to the optical axis of the microscope. For example, a beam with a diameter < 5 nm is possible from alignment of the filament planes perpendicular to ⟨310⟩ and ⟨111⟩. In addition to W and LaB_6, a number of other materials are proposed for field emission applications, such as silicon, single-walled nanotubes,[12] and ultrananocrystalline diamond (UNCD) or Cu/Li alloy films deposited onto sharpened tips.[13]

Two classifications of field emitters are used in electron microscopes, cold and Schottky sources (Table 7.2). Whereas the former operates through electron

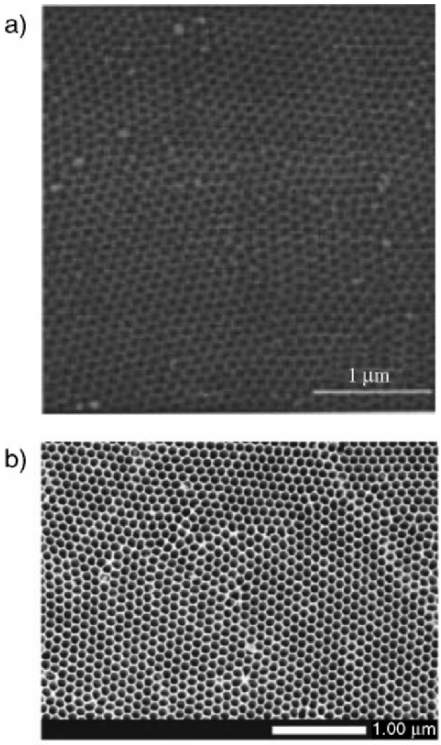

Figure 7.8. Comparison of the resolution for (a) low-resolution SEM,[15] with (b) high-resolution FESEM.[16] Both images are of a nanoporous anodized aluminum oxide template at identical magnification.

tunneling from a cathode wire held at room temperature, the latter features thermionic emission from a ZrO_2-coated sharpened W filament at 1,800 K. In both cases, an electrical field draws electrons from the narrow filament tip into an ultrahigh vacuum (10^{-9} Pa) chamber. When the electrons are accelerated through the magnetic field and focused onto the sample, a dramatically greater resolution is obtained – *ca*. 15 times that of traditional filaments (Figure 7.8). Though cold FE sources feature a higher brightness and smaller spot size than a Schottky FE source, they are not as preferred due to their relatively noisy emission profile. This beam instability arises from the Brownian motion of adsorbed residual gases on the surface of the narrow tip. Though electron microscopes are operated under UHV, these gases are always present in the column – likely originating from the sample itself (residual solvent on grid, e-beam decomposition of the sample, *etc*.). In addition, as electrons strike residual gas molecules in the column, positive ions are generated that may be accelerated back to the electron source. Such ion bombardment will cause a significant deformation of the filament surface, which will lead to beam instabilities. Since Schottky emitters are operated at 1,800 K, these deformations are readily repaired *via* annealing.

However, this is not possible using cold FE sources, which must be periodically "flashed" with a high-temperature pulse in order to repair surface deformations. Though this effectively improves the surface structure of the emitter, the lifetime of the emitter is shorted due to an increase in the tip radius – a consequence of thermal flashing in the absence of an electric field.

7.2.1. Transmission Electron Microscopy

A transmission electron microscope is analogous to a slide projector, with illumination from an electron beam rather than light. When an electron beam is impinged upon a sample, a black and white TEM image is formed from the passage of some electrons through the sample untouched, alongside the combination of interactions between other electrons and sample atoms (*e.g.*, inelastic/elastic scattering, diffraction). If the undiffracted beam is selected to form the image, it is referred to as *bright-field imaging*; in contrast, selection of strongly diffracting regions of the sample, which would appear brighter than the transmitted beam, is known as *dark-field imaging*.[14] It should be noted that electrons may also be absorbed by molecules containing large atoms, or by surface contamination (*e.g.*, dust, grease). The absorption of a high density of electrons in a specific region will cause a buildup of heat, leading to sample destruction and poor image quality.

Analogous to throwing a baseball of varying speeds through a wall, the relative degree of penetration through a particular sample is governed by the energy of the electron source. That is, higher energy electrons (*e.g.*, 200 keV *vs*. 100 keV) will be more penetrating, allowing for the characterization of thicker and/or less transparent samples. In general, increasing the thickness of a sample, or decreasing the energy (*i.e.*, accelerating voltage) of the electron beam, will induce more scattering events through more effective interactions between the electron beam and atoms of the sample. This effect will enhance image contrast, since there is a larger deviation between the path lengths of transmitted and scattered electrons that reach the viewing screen. However, this improvement of image quality is offset by plentiful inelastic collisions that yield a broadened wavelength distribution of the electron beam. Since individual electrons will have differing energies, they will be brought into focus at different points resulting in a blurry image (*i.e.*, decreased resolution).

Sample preparation techniques

Not unlike other materials (or molecular) characterization techniques, the most important and time-consuming aspect of TEM analysis is sample preparation. Specimens for TEM analysis are placed on special micromesh grids of a conductive metal such as Cu, Au, or Ni. The typical dimensions of TEM grids are *ca*. 3 mm in diameter and 10–25 μm thick. The mesh number of a grid indicates the number of grid openings per linear inch. The smaller the grid number, the larger the hole size and the greater the ratio of open area to covered area (Figure 7.9a). For example, a 200 mesh grid has 20 holes along its diameter; a 400 mesh grid has 40 holes. This translates to

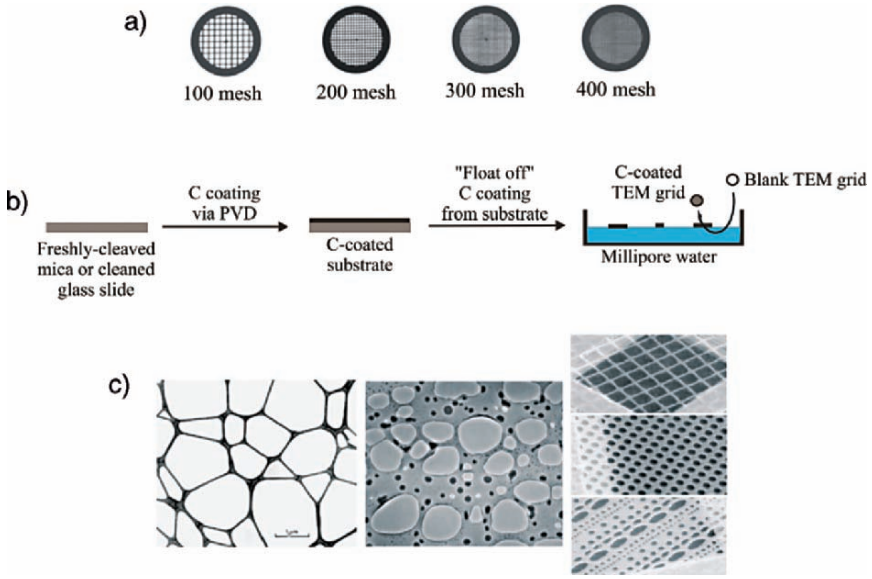

Figure 7.9. (a) A comparison of TEM grid mesh sizes; (b) Illustration of the "float off" method to prepare carbon-coated TEM grids; (c) Comparison of a lacey carbon coating with holey carbon films deposited onto TEM grids.

hole sizes of *ca*. 200 µm for 100 mesh, *ca*. 97 µm for 200 mesh, *ca*. 63 µm for 300 mesh, and *ca*. 42 µm for 400 mesh grids.

Most often, a grid is coated with a support film that holds the sample in place. The film must be as transparent as possible, while providing support for the sample. To prevent interference with electron-sample interactions, films containing light elements (*e.g.*, C, Be) are used. Support films are typically deposited onto the surface of grids through a "floating" technique (Figure 7.9b). Amorphous carbon or plastic (*e.g.*, Formvar – polyvinyl formar, Collodion – nitrocellulose) films are first deposited onto a glass microscope slide or mica surface, and floated off onto the surface of filtered water. For polymer films, the precleaned glass/mica surface is simply immersed in a 0.3% ethylene dichloride solution of the polymer. By contrast, carbon films are deposited onto the glass/mica surface through sputter coating. The coated glass/mica substrate is allowed to dry completely, scored with a razor blade, and slowly immersed into a container of distilled water. When water reaches the score marks, surface tension effects cause the film to be pulled from the glass/mica, resulting in a floating film on the surface of the water. Grids are then dunked into the water and brought up underneath the floating film, lifted out of the water, and allowed to air-dry completely. The coated grids are stored in a dry, dust-free environment.

The typical thickness of amorphous carbon films is 2–5 nm, whereas polymer films have thicknesses on the order of 30 nm. As you might expect, all plastic films are subject to decomposition by the electron beam. Sometimes, this exposure also causes further crosslinking which will cause the film to shrink and become more brittle. The

surface adsorption characteristics of support films vary quite significantly between polymer and carbon varieties. In general, polymer films possess hydrophilic characteristics whereas carbonaceous support films are hydrophobic.

For the imaging of nanomaterials, it is most desirable to have a support film that resembles a piece of lace, featuring many holes on the surface. In this manner, nanostructures such as nanotubes or nanowires are held on the surface of the support film, with unobstructed imaging made possible through holes in the film surface (Figure 7.9c). Such "holey" or "lacey" grids are made from plastic film suspensions to which water or glycerin has been added. Due to the microemulsions created in the solution, when the film is dried, thousands of tiny holes are left in the support film. In this way, the coating itself acts like a mesh grid with the thousands of very tiny open viewing areas.

Due to the high vacuum environment and bombardment of the sample with high-energy electrons, not all samples are appropriate for TEM characterization. In particular, any sample comprising a volatile organic compound, or those containing residual solvents, must be dried using freeze–pump–thaw procedures, or supercritical fluid media. Failure to do so will result in collisions between the electron beam and stray gaseous molecules in the column, resulting in defocusing of the beam and a reduction in image quality. Further, the decomposition of organic matter can severely contaminate the microscope column – especially in finely machined regions such as apertures and pole pieces resulting in blurry images. Some samples may not be directly analyzed even following drying procedures, due to their instability toward the focused electron beam. For these samples (*e.g.*, biological), the specimen is mounted within a plastic support resin, and very thin pieces of the composite are shaved off using an ultramicrotome fitted with a diamond, sapphire, or glass knife (Figure 7.10).

TEM grids of solid samples are typically prepared by pipetting a few drops of a solution containing the suspended solid onto a grid, and allowing it to air-dry. Alternatively, the suspension may be blown onto a grid using an aerosol delivery device (Figure 7.11). If the solid is too thick, or comprises relatively large

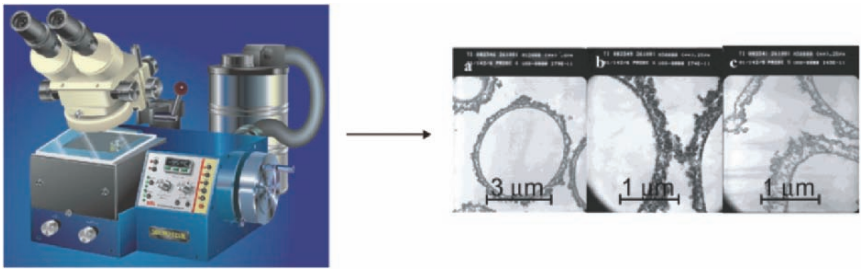

Figure 7.10. Sectioning of a TEM sample using an ultramicrotome instrument. Shown is an ultramicrotome instrument with a built-in nitrogen cryogenic system, used to section samples with a thickness of 25 nm–5 mm.[17] Also shown is a TEM image of polymer capsules that have been sectioned using an ultramicrotome instrument. Image reproduced with permission from Dai, Z.; Mohwald, H. *Langmuir* **2002**, *18*, 9533. Copyright 2002 American Chemical Society.

Figure 7.11. Photo of a glass aerosol delivery system used to spray solvent-suspended particulates onto a TEM grid.

granules, the material may be embedded within a polymeric matrix and cut into thin cross sections. The best embedding medium permits thin sectioning with the least damage during preparation, and gives the least interference during microscopy. While early embedding media included gelatin and paraffin, the <100 nm sections that are required for electron microscopy were not possible to cut using any of these media. Nowadays, polymers such as methacrylates, epoxy and polyester resins are typically employed for sectioning applications, since they are nontoxic, inexpensive, and strong enough to withstand very thin mechanical sectioning. For methacrylates, the degree of final block hardness can be predictably controlled by mixing methyl (hard) and *n*-butyl (soft) functionalities. However, with respect to electron beam stability, epoxy resins are by far superior to both methacrylates and polyester resins.

The "best" section thickness not only depends on the electron opacity of the sample, but also on the operating conditions of the TEM. In general, the higher the accelerating voltage, the thicker the sample cross section may be. For instance, epoxy-based sections of up to 250 nm thick may be used for standard TEM analyses, operating at 100 kV. However, section thicknesses in the range of 50–60 nm are typically used for TEM analysis, in order to improve the resolution through reduced electron scattering.

A recent alternative to (ultra)microtoming is the use of a *focused-ion beam* (FIB) to etch/mill away undesired portions of the sample (Figure 7.12). The most common beam is gallium ions from a liquid gallium source, with an energy of *ca.* 30 keV. Extreme control over the resultant cross section is afforded by varying the beam current/energy, and scanning speed of the ion beam. This technique is especially useful for the study of polymer films that have been deposited onto hard inorganic substrates – using a FIB/lift-out method.[18] Typically, a dual-beam FIB/SEM is used for sample preparation, which affords real-time monitoring of FIB sectioning (Figure 7.12b). A more recent use of a FIB instrument is nanofabrication. In particular, *in situ* CVD of a thin film may be deposited through the introduction of a co-reactant precursor gas during ion bombardment (Figure 7.12c). It should be noted that in contrast to ultramicrotomy, FIB preparation does not induce mechanical stress on the sample surface, which often leads to deformation and interfacial debonding. However,

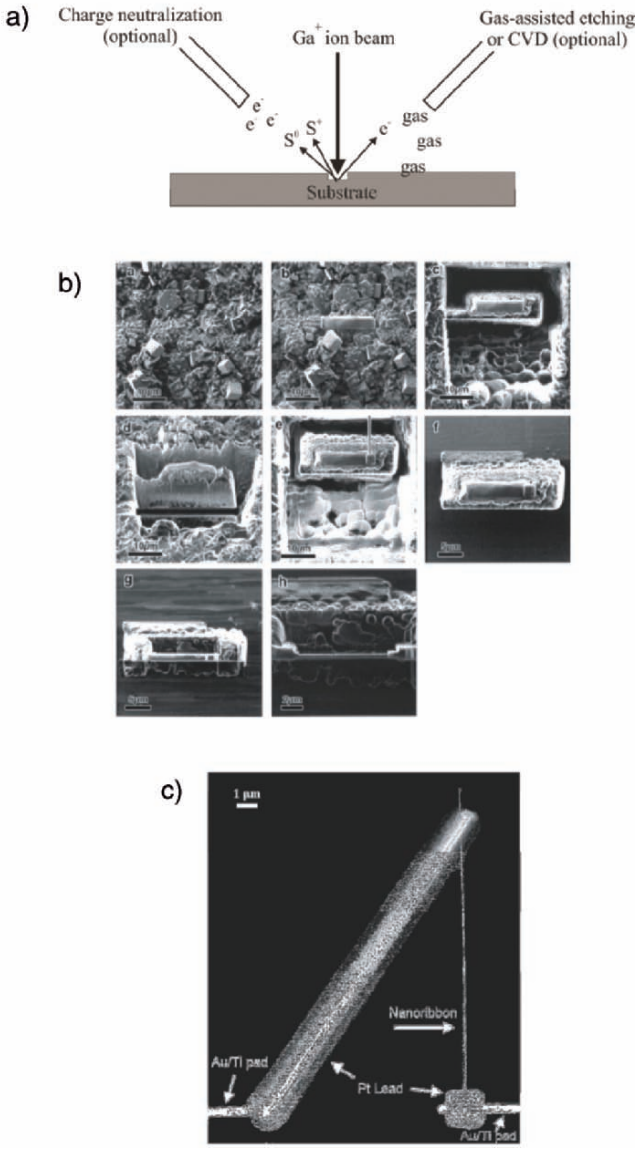

Figure 7.12. Applications for focused-ion beam (FIB). Shown is (a) general illustration of the technique, with a gallium ion source and emission of secondary electrons, as well as charged ions and atoms from the substrate surface (S^+ and S^0, respectively). The optional "charge neutralization" electron beam is used for *in situ* imaging of a surface during FIB (dual-beam FIB/SEM). The images shown in (b) represent the sectioning of a zeolitic membrane (images c and d illustrate FIB milling to a depth of 20 µm, and cutting off the bottom surface; latter images show the manipulation of the milled target and further sectioning by FIB).[19] The SEM image in c illustrates the use of FIB for nanofabrication – the selective deposition of Pt contact leads onto the ends of a Ga_2O_3 nanowire.[20]

the high-energy radiation may result in other surface modifications such as amorphization, shrinkage, and bond cleavage – especially for "soft," polymeric-based samples.[21]

Oftentimes, a lack of image contrast in TEM results from the analysis of very thin sections (*e.g.*, <30 nm), or samples comprising light elements (*e.g.*, hydrocarbons, B, Li, *etc.*). In order to increase the contrast, elements of high atomic weight are introduced to selective regions of the sample – a process referred to as *staining* (Figure 7.13). Due to their high electron density, staining agents are better able to stop or deflect the beam of electrons, whereas elements of low weight allow the beam to pass through relatively unimpeded. Electron staining falls into one of two categories:

(i) *Positive staining* – contrast is imparted to the sample.
(ii) *Negative staining* – contrast is imparted to the area surrounding the sample.

The most common staining agents are aqueous solutions (*ca.* 2 wt% concentration) of OsO_4 (osmium tetroxide), RuO_4 (ruthenium tetroxide), $UO_2(CH_3COO)_2 \cdot 2H_2O$ (uranyl acetate), $Pb(C_6H_2O_7)_2 \cdot 3H_2O$ (lead citrate), or $Na_3[PW_{12}O_{40}] \cdot 30H_2O$ (sodium phosphotungstate). Due to the presence of heavy metals, these agents are considerably toxic and must be handled/disposed with great care. Whereas most of

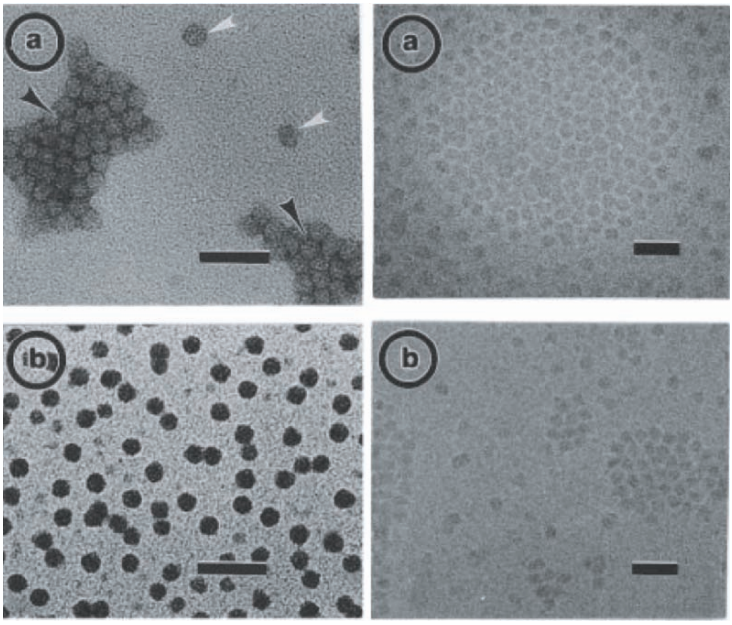

Figure 7.13. (Left, a) TEM image of G10 PAMAM dendrimers stained with 2% methylamine tungstate, showing both positively (white arrows) and negatively (black arrows) stained regions. (Left, b) TEM image of G9 PAMAM dendrimers positively stained with sodium phosphotungstate, showing little agglomeration. (Right, a, b): TEM images showing the lack of contrast from unstained G10 PAMAM dendrimers, imaged in vitrified water using cryo-TEM. The scale bar for all images is 50 nm. Reproduced with permission from Jackson, C. L.; Chanzy, H. D.; Booy, F. P.; Drake, B. J.; Tomalia, D. A.; Bauer, B. J.; Amis, E. J. *Macromolecules* **1998**, *31*, 6259. Copyright 1998 American Chemical Society.

these agents interact most strongly with amino and phosphate groups, lead ions preferentially interact with hydroxyl groups. For biological staining, it has been widely shown that OsO_4 interacts more readily with lipids than proteins, resulting in a structure-specific staining agent. The use of lead citrate requires special considerations due to its high sensitivity to CO_2; hence, NaOH is often used as a CO_2-scavenger for the aqueous staining solution.

Nonimaging applications for TEM

Due to the high spatial resolution and predictive scattering modes, TEMs are often employed to determine the three-dimensional crystal structure of solid-state

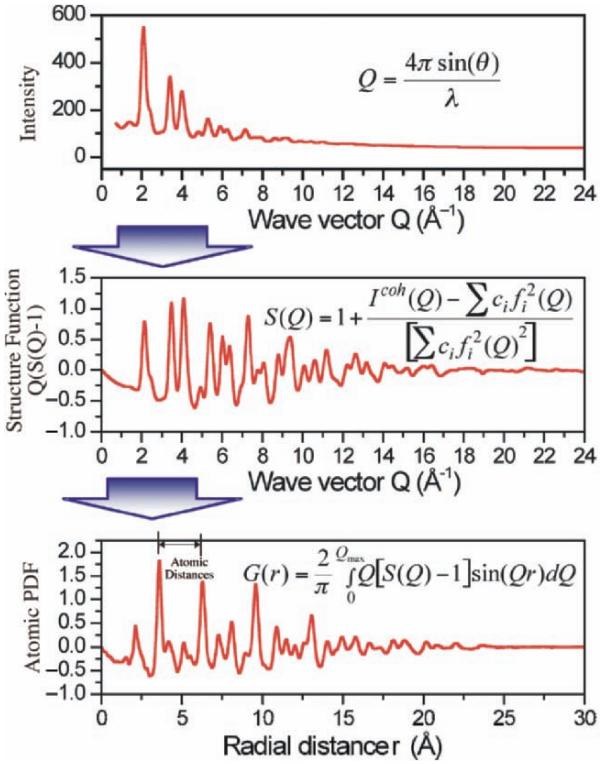

Figure 7.14. The atomic pair distribution function (PDF) used to characterize powders by high-energy X-ray diffraction. Shown (top-bottom) is the conversion of the reflection intensity data into the atomic PDF, which yields information regarding the average inter-atomic spacings of the powder in real space. The three-dimensional structure of the solid is determined by using software, which compares the experimental PDF with structural models that best fit the data. This method is preferred over competing techniques such as Rietveld analysis since the peaks are in real space (not reciprocal space), and both Bragg peaks and diffuse scattering are included in the data. It should be noted that for maximum resolution, Q_{max} in the sine Fourier transform must be as high as possible. Since Q is inversely proportional to the radiation wavelength, a synchrotron source is often utilized ($\lambda = 0.1$ Å, relative to 1.54 Å for a traditional powder X-ray diffractometer). Images provided courtesy of Prof. Valeri Petkov, Department of Physics at Central Michigan University. For more information, see http://www.phy.cmich.edu/people/petkov/

materials. Thus, TEM may be considered as complementary to conventional crystallographic methods such as X-ray diffraction (Figure 7.14). When electrons (or X-rays) interact with a crystalline solid, comprising a regularly spaced three-dimensional array of atoms, the incoming beam is diffracted at specific angles, as predicted by the Bragg equation (Eq. 6). Simply stated, Bragg's Law suggests that for a particular pair of d and λ, diffraction will occur at a specific angle (known as a Bragg reflection):

$$n\lambda = 2d(\sin\theta), \tag{6}$$

where d is the lattice spacings of the crystal planes (*e.g.*, d_{10} would indicate the spacing of the (10) planes in two-dimensions); λ, the wavelength of the incoming beam; and θ is the angle of the incident (and diffracted: $\theta_{in} = \theta_{out}$) beam.

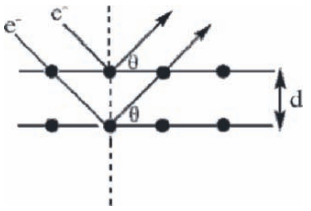

In order to understand the information contained within the diffraction pattern of a crystal lattice, it is necessary to construct a secondary lattice known as a *reciprocal lattice*. This lattice is related to the "real" crystalline array by the following (Figure 7.15):

(i) For a two-dimensional lattice defined by vectors a and b, the reciprocal lattice is defined by vectors a^* and b^*, such that $a^* \perp a$ and $b^* \perp b$.

(ii) The magnitude of the reciprocal lattice vectors are equal to the inverse of the lattice spacings of the associated planes in the real lattice (Eq. 7):

$$\frac{1}{d} = \frac{2}{n\lambda}(\sin\theta). \tag{7}$$

It should be noted that for a three-dimensional reciprocal lattice, a third vector (c^*) is used that is perpendicular to *both* a and b axes of the real lattice.

In order to determine which lattice planes give rise to diffraction, a geometrical construct known as an *Ewald sphere* is used (Figure 7.16). An incident wave that impinges on the crystal is denoted as a reciprocal lattice vector, **k**, which passes through the origin. The Ewald sphere (or circle in two-dimensional) shows which reciprocal lattice points, (each denoting a set of planes) that satisfy Bragg's Law for diffraction of the incident beam. A specific diffraction pattern is recorded for any **k** vector and lattice orientation – usually projected onto a two-dimensional film or CCD camera. In general, very few reciprocal lattice points will be intersected by the Ewald sphere,[22] which results in few sets of planes that give rise to diffracted beams. As a result, a single crystal will usually yield only a few diffraction spots. If a sample is single-crystalline, sharp spots will be observed; a polycrystalline sample

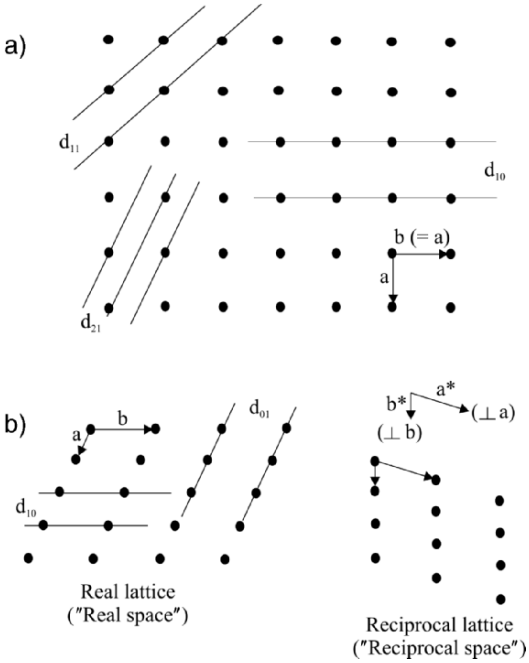

Figure 7.15. (a) Illustration of a two-dimensional square lattice, showing various lattice spacings; (b) a comparison of real space and reciprocal space for a crystalline solid. In the reciprocal lattice, the magnitudes of a^* and b^* are $1/d_{10}$ and $1/d_{01}$, respectively.

will yield many closely spaced diffraction spots. By contrast, an amorphous sample will give rise to diffuse rings.

Since the wavelength of an accelerated electron in a TEM is much smaller than an X-ray beam, the Ewald sphere (radius: $1/\lambda$) is significantly larger for electron diffraction relative to X-ray diffraction studies. As a result, electron diffraction yields much more detailed structural information of the crystal lattice. Information such as lattice parameters and atomic positions in a crystal may be obtained through analyzing the *in situ* electron diffraction pattern from a specimen size of *ca.* >400 nm (>100 nm for a field emission source). This technique is denoted as *selected area electron diffraction* (SAED, Figure 7.17). In addition, the lenses within a TEM allow one to alter the orientation of the incoming electron beam, from a parallel beam to a cone-shaped beam. The latter orientation is known as convergent beam electron diffraction (CBED), and allows one to conduct a diffraction experiment over many incident angles simultaneously to reveal the full three-dimensional reciprocal lattice of the crystal.

In the same manner as X-ray diffraction, by examining the systematic absences of the diffraction spots (Table 7.3), one may easily determine the appropriate Bravais

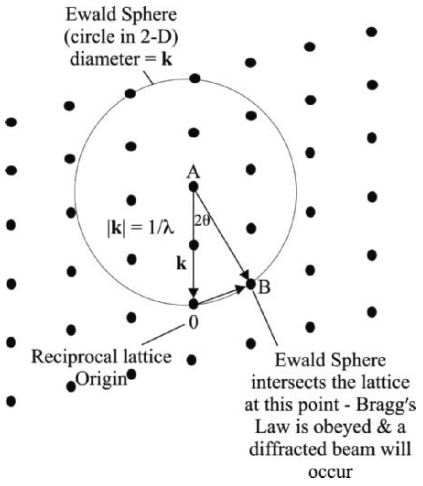

Figure 7.16. Illustration of Ewald sphere construction, and diffraction from reciprocal lattice points. This holds for both electron and X-ray diffraction methods. The vectors AO, AB, and OB are designated as an incident beam, a diffracted beam, and a diffraction vector, respectively.

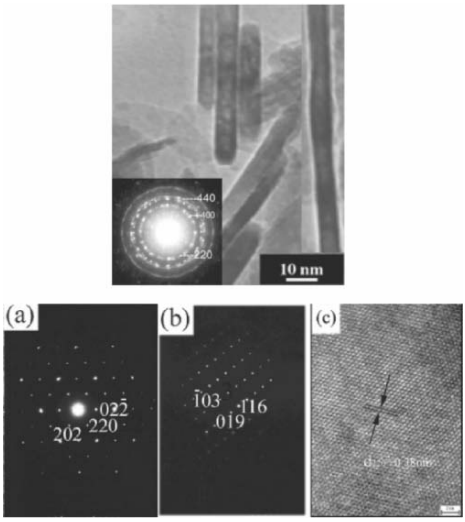

Figure 7.17. (top) SAED pattern from a polycrystalline $MgAl_2O_4$ nanorods.[24] (bottom) SAED patterns (a, b) and high-resolution TEM image (c) of a single-crystalline In_2S_3 nanoparticle. Images (a) and (b) illustrate the diffraction patterns for cubic and tetragonal unit cells, respectively. The TEM image shown in (c) illustrates the lattice fringes and interplanar spacing of 3.81 Å, corresponding to the (220) interplanar spacing of cubic In_2S_3.[25] In high-resolution images, lattice fringes result from the interference of the transmitted and diffracted beams; these are only evident in the TEM image when the lattice spacings are larger than the resolution of the electron microscope.

Table 7.3. Systematic Absences for Electron and X-Ray Diffraction

Cause of absence	Symbol	Absences[a]
Body-centering	I	$h + k + l = 2n + 1$ (odd)
A centering	A	$k + l = 2n + 1$
B centering	B	$h + l = 2n + 1$
C centering	C	$h + k = 2n + 1$
Face-centering	F	*hkl* mixed (not all even or all odd)
Glide plane//(100)	b	$k = 2n + 1$
	c	$l = 2n + 1$
	n	$k + l = 2n + 1$
	d	$k + l = 4n + 1$
Glide plane//(010)	a	$h = 2n + 1$
	c	$l = 2n + 1$
	n	$h + l = 2n + 1$
	d	$h + l = 4n + 1$
Glide plane//(001)	a	$h = 2n + 1$
	c	$k = 2n + 1$
	n	$h + k = 2n + 1$
	d	$h + k = 4n + 1$
Screw axis//*a*	2_1 or 4_2	$h = 2n + 1$
	4_1 or 4_3	$h = 4n + 1$
Screw axis//*b*	2_1 or 4_2	$k = 2n + 1$
	4_1 or 4_3	$k = 4n + 1$
Screw axis//*c*	2_1 or 4_2	$l = 2n + 1$
	3_1, 3_2, 6_2, or 6_4	$l = 3n + 1, 3n + 2$
	4_1 or 4_3	$l = 4n + 1, 4n + 2, 4n + 3$
	6_1 or 6_5	$l = 6n + 1, \ldots, 6n + 5$
Screw axis//(110)	2_1	$h = 2n + 1$

[a]Refers to the Miller indices ((*hkl*) values) that are absent from the diffraction pattern. For instance, a body-centered cubic lattice with no other screw axes and glide planes will have a nonzero intensity for all reflections where the sum of $(h + k + l)$ yields an odd number, such as (100), (111), *etc*.; other reflections from planes in which the sum of their Miller indices are even, such as (110), (200), (211), *etc*. will be present in the diffraction pattern. As these values indicate, there are three types of systematic absences: three-dimensional absences (true for all *hkl*) resulting from pure translations (cell centering), two-dimensional absences from glide planes, and one-dimensional absences from screw axes.[26]

lattice as well as any screw axes and glide planes that are present in the crystal lattice. Since TEM is more user-intensive, involves significant sample preparation, and often results in sample damage from the high-energy electron beam, highly automated X-ray and neutron (useful for light elements such as H) diffraction methods are the preferred methods to yield structural information from a bulk crystalline solid. However, if structural information is desired from an individual nanocrystal, TEM/SAED is the best alternative.[23]

Before leaving the subtopic of electron diffraction, it should be noted that two other techniques known as low-energy electron diffraction (LEED) and reflection high-energy electron diffraction (RHEED) may also be used to gleam structural

information from a crystalline sample. Both techniques are performed independent of a TEM instrument, and utilize an electron gun and fluorescent screen to show the structure and morphology of a crystal surface. The RHEED technique uses a high accelerating voltage and low impact angle in order to focus the electrons to the first few atomic layers of the crystal surface. This technique may be used to monitor crystal growth in real time, or to probe the surface adsorption properties for sensor development. For beam-sensitive crystalline samples (*e.g.*, organic thin films), either LEED or microchannel plate (MCP)–RHEED may be used; the latter features the amplification of the incident electron beam *via* a MCP – resulting in much lower intensities of the incident electron beam.

In addition to structural information from crystalline samples, quantitative analysis may also be carried out in tandem with TEM (and SEM) analyses. The interaction among high-energy electrons and sample atoms results in a variety of emissions (Figure 7.18) that yield important information regarding the surface morphology

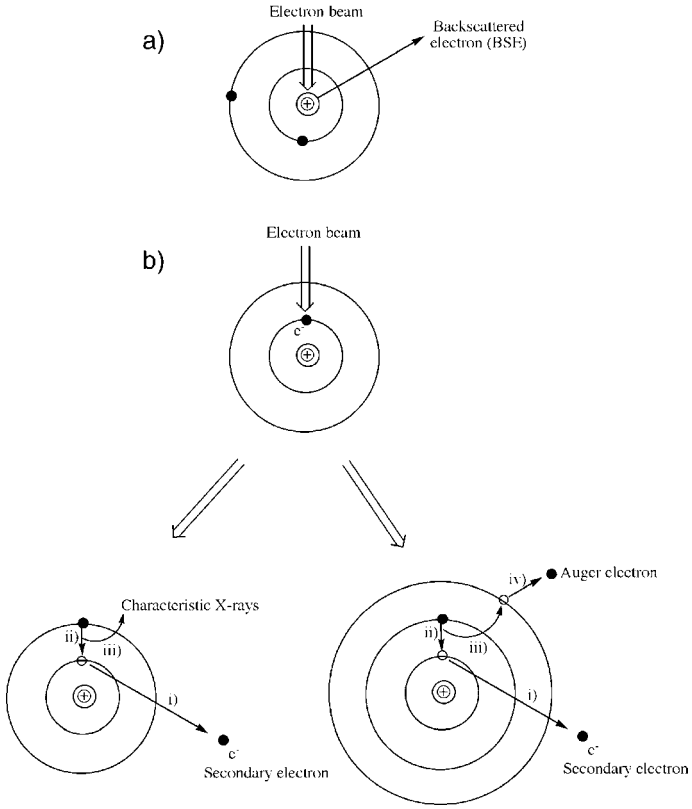

Figure 7.18. Types of possible interactions between the primary electron beam and (a) the nucleus of surface atoms and (b) electrons of surface atoms comprising the sample. For simplicity, only K, L, and M shells (with no L and M subshells) are shown.

and elemental composition of the sample. As previously stated, if the electron beam interacts with the nucleus of surface atoms, the electrons are elastically scattered. In this case, the trajectory of the electron changes with no change in the kinetic energy or velocity, a process known as *backscattering*.

The number of *backscattered electrons* (BSE) that are produced from a given atom is proportional to the atomic number. That is, materials composed of heavy atoms will backscatter more electrons, resulting in brighter gray tones in the image relative to less dense materials. Hence, BSE produce an image that is related to material composition, providing both spatial and chemical information.

The primary electron beam may also be inelastically scattered through interaction with electrons from surface atoms. In this case, the collision displaces core electrons from filled shells (*e.g.*, ns^2 (K) or np^6 (L)); the resulting atom is left as an energetic excited state, with a missing inner shell electron. Since the energies of these *secondary electrons* are sufficiently low, they must be released from atoms near the surface in order to be detected. Electrons ejected from further within the sample are reabsorbed by the material before they reach the surface. As we will see in the next section (re SEM), as the intensity of the electron beam increases, or the density of the sample decreases, information from underlying portions of the sample may be obtained.

In order for the excited-state atom to return to its ground state (within a picosecond or so following secondary electron generation), the vacancy in the K shell is filled with an electron from shells farther from the nucleus (*e.g.*, L shell, Figure 7.19). When such post-ionization atomic relaxation occurs, the excess energy may be released as either characteristic X-rays, or through nonradiative emission of an *Auger electron* (Figure 7.18b; Auger electron spectroscopy (AES) will be discussed later). Especially for elements with $Z > 11$ (*i.e.*, >Na), the electronic shell structure becomes exceedingly complex, which results in electronic transitions that are possible from a number of outer shells (Figure 7.19, bottom).

Typically, a variety of X-rays are produced during atomic relaxation due to a cascading effect. For instance, a vacancy in the K shell may be filled with an electron in an L shell (K_α emission); the resulting vacancy in the L shell may then be filled with an electron from the M shell ($L_{\alpha 1}$ emission), and so forth. By counting the number and energies of X-rays produced from electrons interacting the sample, it is possible to both qualitatively and quantitatively (using suitable standards) determine the chemical composition of the surface being analyzed.

There are two methods used to identify and quantify the X-ray emission: *energy-dispersive X-ray spectroscopy* (EDS), and *wavelength-dispersive X-ray spectroscopy* (WDS).[28] In EDS, all of the characteristic X-ray energies reaching the detector are measured simultaneously. Hence, data acquisition is very rapid across the entire spectrum. By contrast, WDS measures a single wavelength at a time through use of a detecting crystal. As the characteristic X-rays are emitted from the sample, they are diffracted in a regular manner as discussed previously. Not only does this improve the resolution of WDS to an order of magnitude greater than EDS (Figure 7.20),[29] but also improves the count rate and deconvolution of overlapping spectral peaks. Nevertheless, due to its simplicity and speed of analysis, EDS is the standard method

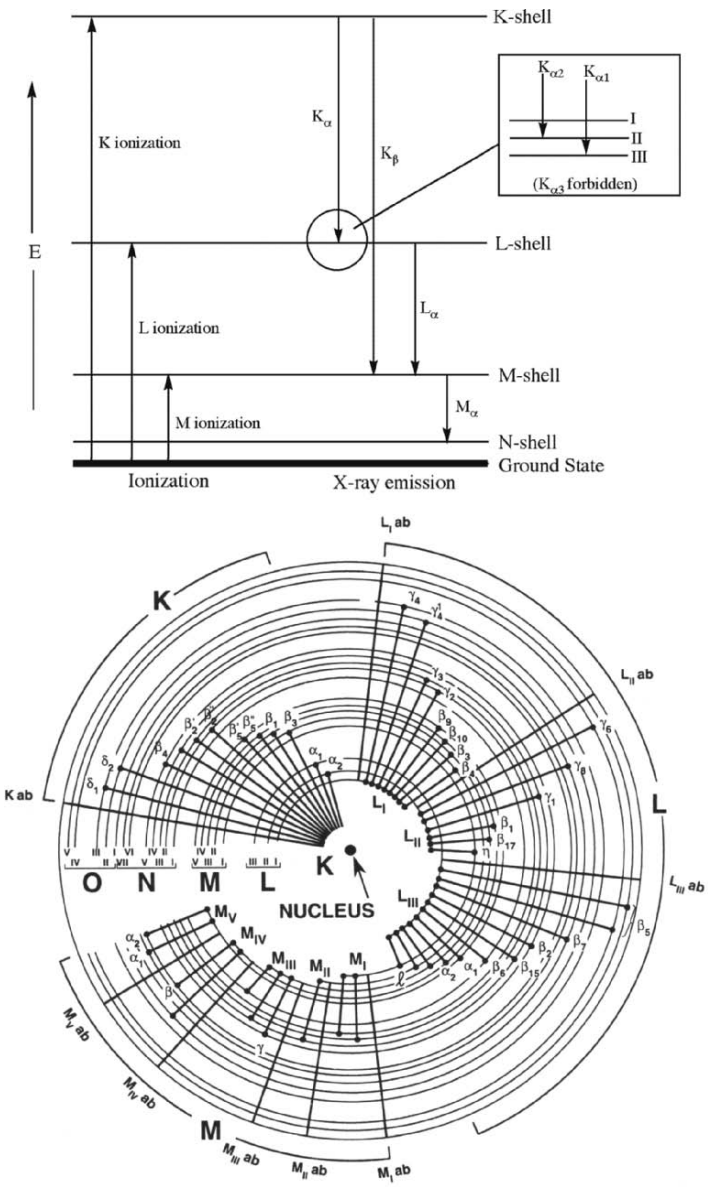

Figure 7.19. Simplified (top) and detailed (bottom) illustration of atomic energy levels, showing the characteristic X-rays emitted as the atom's energy returns to the ground state following ionization. The α and β designations indicate the filling of K, L, or M electron vacancies from adjacent ($n + 1 \rightarrow n$) and ($n + 2 \rightarrow n$) energy levels, respectively.[27] The inset shows transitions between the K shell and L subshells. The illustration of detailed electronic transitions for Cu was reproduced with permission from Goldstein, J.; Newbury, D.; Joy, D.; Lyman, C.; Echlin, P.; Lifshin, E.; Sawyer, L.; Michael, J. *Scanning Electron Microscopy and X-Ray Microanalysis*, 3rd ed., Kluwer: New York. Copyright 2003 Springer Science and Business Media.

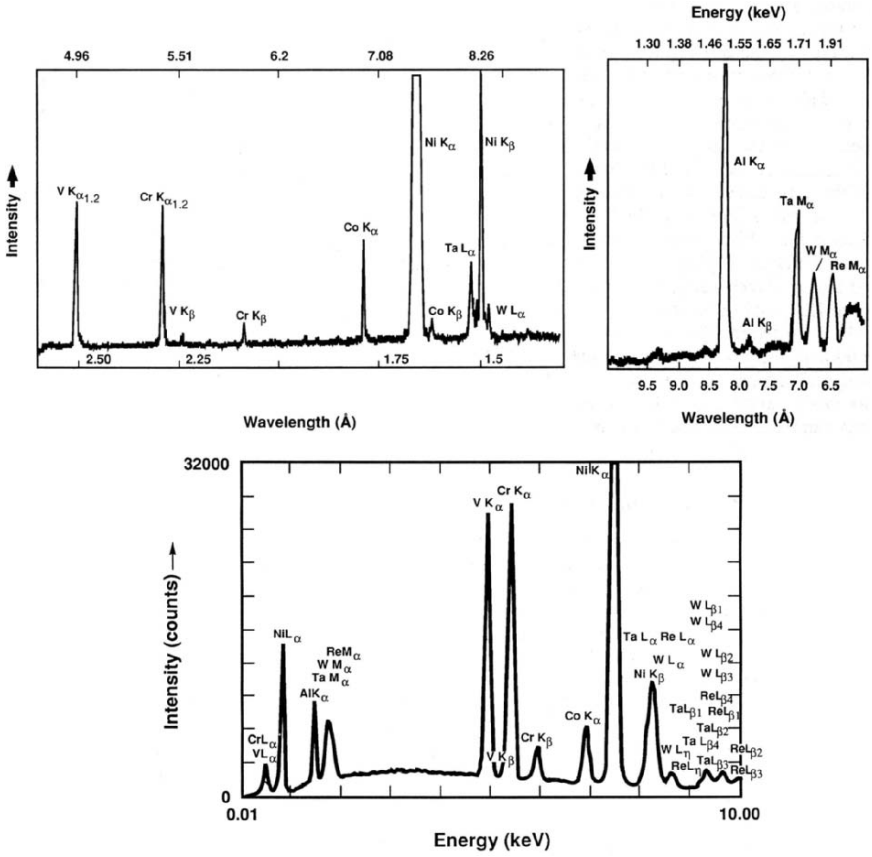

Figure 7.20. Comparison of WDS (top, using LiF and thallium acid phthalate (TAP (1010), respectively) and EDS for the analysis of a superalloy. A number of X-ray spectral lines such as Ta Lα, Ni Kβ, and W Lα are hardly discernible using EDS, but readily visible using WDS analysis. Reproduced with permission from Goldstein, J.; Newbury, D.; Joy, D.; Lyman, C.; Echlin, P.; Lifshin, E.; Sawyer, L.; Michael, J. *Scanning Electron Microscopy and X-Ray Microanalysis*, 3rd ed., Kluwer: New York. Copyright 2003 Springer Science and Business Media.

for chemical analysis within TEM (and SEM) instruments. Typically, if WDS is desired, an instrument known as electron probe microanalyzer (EPMA) is utilized, often in tandem with SEM imaging.

The spatial resolution of X-ray microanalysis may be described by Eq. 8. In general, prerequisites for the best spatial resolution include a high-energy electron beam and extremely thin samples. Though the resolution limits of EDS/WDS will never match the imaging resolution, it is now possible to easily determine the elemental composition of individual nanoclusters in the 1–5 nm size regime – as long as they are suitably dispersed with respect to one another (Figure 7.21):

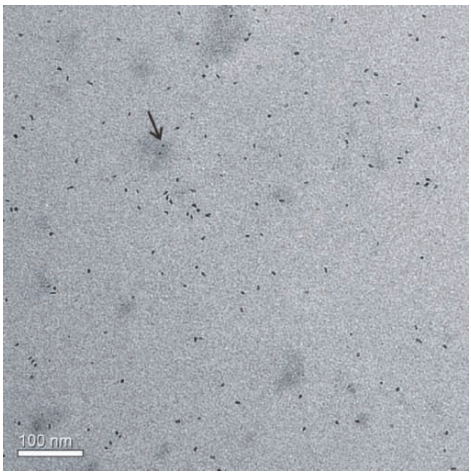

Figure 7.21. Ambiguity in assigning a chemical composition (iron oxide) to individual nanostructures based on TEM/EDS. The small and large nanoparticles are in the same vicinity on the grid; Depending on the area selected for analysis, it may be difficult to definitely state if one (or both) comprise iron oxide (*e.g.*, arrow region). However, by also looking at the relative contrast of the nanoparticles, it is likely that the smaller structures contain iron (higher density) and the larger nanoparticles comprise lighter elements (*e.g.*, a carbonaceous, organic-based nanostructure).[32]

$$R = \frac{d + \sqrt{\left(7.21 \times 10^5 \frac{Z}{E_o}\sqrt{\left(\frac{\rho}{A}\right)}t^{3/2}\right)^2 + d^2}}{2}, \tag{8}$$

where R is the X-ray spatial resolution; d, the beam diameter; E_o, the beam energy (eV); ρ, the specimen density; and t is the specimen thickness (cm).

Scanning transmission electron microscopy

An imaging mode that merges both SEM and TEM is also possible on most modern TEM instruments. This method, referred to as *scanning transmission electron microscopy* (STEM), uses a LaB_6 source that produces a focused electron beam with a high current density and extremely small diameter. Instead of monitoring the transmitted electrons from a static beam as performed in standard TEM imaging, the beam within a STEM is scanned across the sample – analogous to SEM. Due to a higher beam intensity, thicker samples may be analyzed in a STEM; furthermore, staining is generally not necessary for low-Z elements due to a higher sensitivity to sample density/composition. In particular, it is possible to overlay the image with the EDS data – a technique known as *elemental dot-mapping*, widely used for SEM/EDS analysis (Figure 7.22).

The majority of STEM instruments are simply conventional TEMs with the addition of scanning coils. As a result, these "nondedicated STEMs" are capable of TEM/STEM, as well as SEM imaging for thicker samples. The development

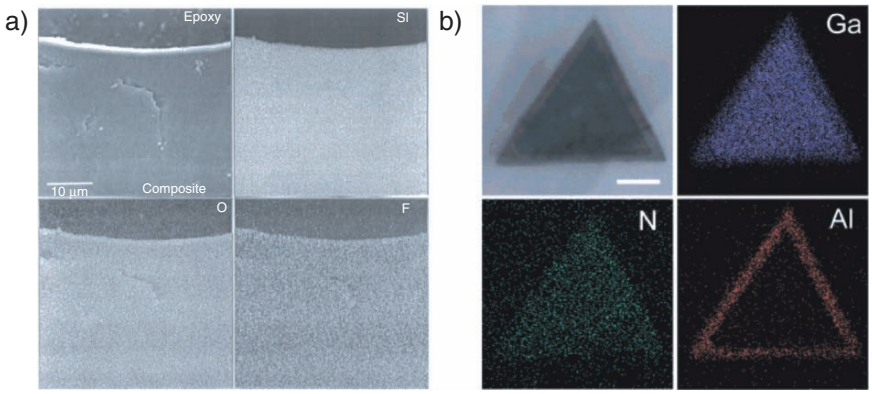

Figure 7.22. Elemental dot-maps. Shown is (a) elemental concentrations of Si, O, and F (as white pixels) overlaid onto the SEM image of a Nafion resin/silica composite[33]; (b) bright-field STEM image of a GaN/AlN/AlGaN nanowire cross section, with elemental mapping of Ga, N, and Al (scale bar is 50 nm).[34]

of HRTEMs and "dedicated" STEMs with lens aberration correction[30] have now pushed the resolution limits to as low as 0.1 nm, *i.e.*, 1 Å, the approximate diameter of the smallest atoms in the Periodic Table![31] In contrast to conventional TEMs, the beam system of dedicated STEMs is reversed, with the placement of the gun on the bottom of the microscope and detectors at the top (Figure 7.23). Since there are no post-sample refocusing lenses, it is not possible to generate a bright-field image as is standard using a conventional (HR)TEM. Instead, the image is based on specific interactions between the electron beam and sample atoms (*i.e.*, elastic/inelastic scattering, unscattered electrons).

In a dedicated STEM, high-angle (elastically) scattered electrons are separated from inelastic/unscattered electrons through use of a high-angle annular dark-field (HAADF) detector (Figure 7.23). Since the incoherently scattered electrons are related to elastic scattering, they are directly related to the structure and chemical composition of the feature being imaged (Figure 7.24).[35] In particular, the incoherent scattering of an electron is described by the Rutherford equation (Eq. 9). This equation predicts that the intensity of the scattered electrons, and resultant image contrast, is strongly dependent on atomic number of the sample atoms. Hence, HAADF–STEM is also referred to as Z-contrast imaging. It should be noted that HAADF–STEM is strongly dependent on variations in sample thickness.[36] That is, thicker regions of a sample will result in higher image intensities, which may be falsely interpreted as the presence of species with relatively high atomic numbers:

$$\frac{\mathrm{d}\sigma(\theta)}{\mathrm{d}\Omega} = \frac{e^4 Z^2}{16(E_\mathrm{o})^2 \sin^4 \dfrac{\theta}{2}}, \tag{9}$$

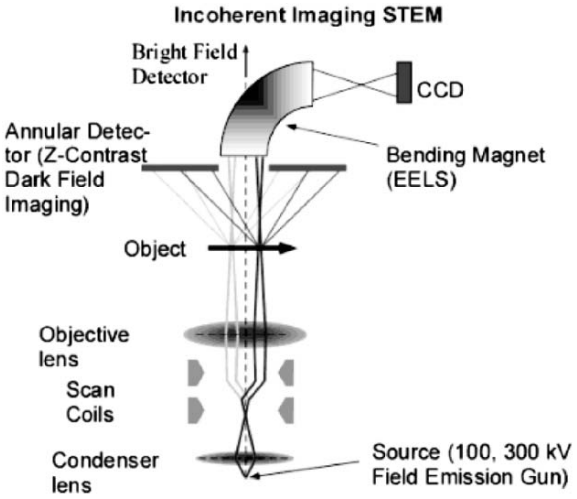

Figure 7.23. Schematic of a dedicated HAADF–STEM. Reproduced with permission from McBride, J. R.; Kippeny, T. C.; Pennycook, S. J.; Rosenthal, S. J. *Nano Lett.* **2004**, 4, 1279. Copyright 2004 American Chemical Society.

where $d\sigma(\theta)/d\Omega$ is the different scattering cross sections as a function of the scattering angle (θ); E_o, the incident beam energy; e, the electron charge (1.602×10^{-19} C); and Z is the atomic number of the scattering nucleus.

A primary limitation of EDS and WDS is the inability to detect light (*i.e.*, low-Z) elements. Since atomic energy levels are closely spaced for low-Z elements, the energies of the emitted X-rays will be relatively low.[37] As a result, they are masked by the broad, continuous background spectrum (known as *bremsstrahlung*[38]) that is most intense at energies below 1 keV. Furthermore, the characteristic X-ray lines are less intense for low-Z elements since they exhibit a low *X-ray fluorescence yield* – favoring nonemissive Auger[39] electron processes rather than X-ray generation (Figure 7.25). Consequently, it becomes increasingly more difficult to observe X-ray lines from elements with $Z < 11$ (Na). Recently, there have been improvements in the design of EDS windows, which separate the detection system from the electron microscope.[40] Since low-energy X-rays are readily absorbed, new detector designs feature ultrathin windows and lightweight compositions that facilitate the detection of elements down as far as beryllium ($Z = 4$). However, the analysis of these elements by EDS/WDS is semiquantitative, at best.

Electron energy-loss spectroscopy

In order to increase the sensitivity toward the detection of light elements, a technique known as *electron energy-loss spectroscopy* (EELS) may be utilized.[41] This method may be carried out within a (S)TEM, and consists of monitoring the loss in energy (due to inelastic scattering) of the beam electrons as they pass through the sample. Since it is more difficult to focus X-rays relative to electrons with appropriate lenses,

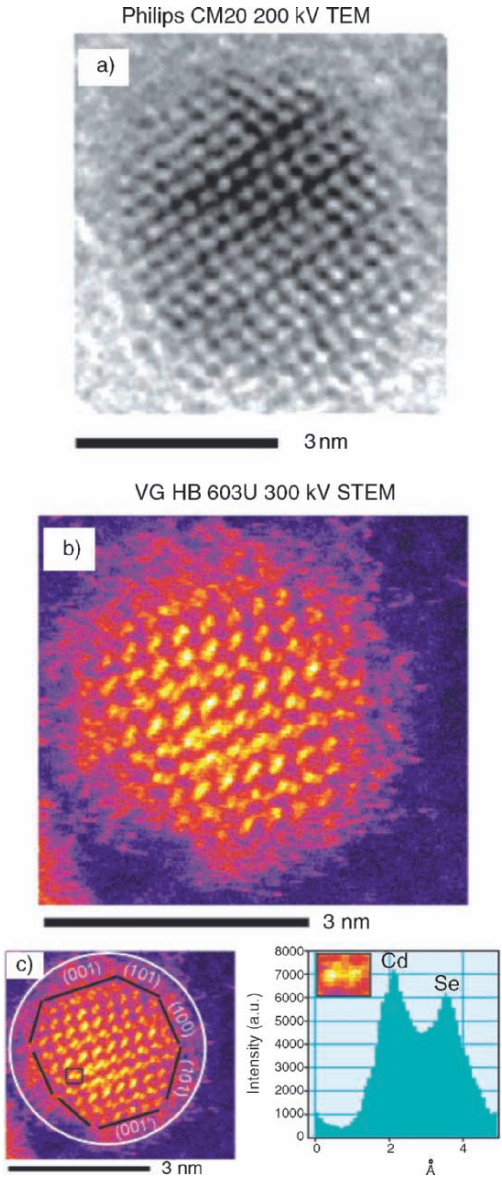

Figure 7.24. Comparison of conventional HRTEM (a), with HAADF–STEM (b). Also shown (c) is the chemical analysis of an individual CdSe "dumbbell." The white circle shows the amorphous oxide region, and the surface of the nanocrystal is outlined in black. Unlike conventional HRTEM, it is also possible to label the individual nanocrystal facets, such as Cd-rich (001) and Se-rich (001′). Reproduced with permission from McBride, J. R.; Kippeny, T. C.; Pennycook, S. J.; Rosenthal, S. J. *Nano Lett.* **2004**, *4*, 1279. Copyright 2004 American Chemical Society.

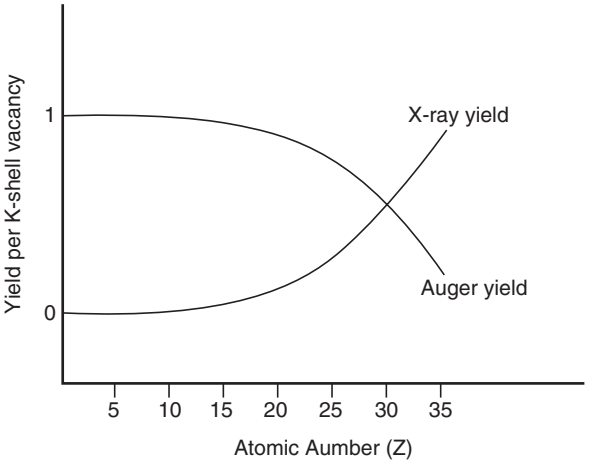

Figure 7.25. Relative probabilities for X-ray and Auger electron emission during the decay of K-electron vacancies.

the collection efficiency for EELS is *ca.* 80–90%, relative to 5–6% for EDS. This leads to a greater sensitivity and spatial resolution for EELS, with elemental mapping of *ca.* $\geq$ 2 Å. The intensity is greater than EDS for light elements since the signal generated by EELS represents the total sum of the number of X-ray photons and Auger electrons emitted from the sample. This technique is useful for elements with $Z > 1$, and like EDS, is amenable for elemental mapping of a sample surface.

As illustrated in Figure 7.23, a dedicated STEM is usually fitted with an EELS detector, which collects the low-angle scattered electrons that pass by the HAADF. Although the beam electrons have energies of several hundred keVs, the electrons being transmitted through the sample only have energies on the order of a few eVs. In order to perform EELS, it is therefore necessary to detect very small differences in the kinetic energies of the electrons. This is accomplished using a magnetic prism that exerts a centripetal force on each electron, causing a circular motion. While in the magnetic field, electrons move along the arc of a circle, whose radius is based on the speed and kinetic energy of the electron. In reality, there is nothing new with this concept; a magnetic prism is actually analogous to the dispersion of white light into a colored spectrum using a glass prism. However, unlike a glass prism, the magnetic field focuses the electrons as they exit the field, generating a spectrum from the grouping of electrons that exhibited identical energy losses.

In addition to detecting/quantifying particular elements in a sample, EELS also provides detailed elemental information such as the electronic structure, bonding, and nearest neighbor distribution of the atoms in the sample.[42] A representative EELS spectrum for a NiO surface is shown in Figure 7.26. The most intense features are peaks corresponding to zero-loss – those electrons that were either unscattered, or elastically scattered, while traversing through the sample. At relatively small energy losses (*ca*. 5–25 eV), a plasmon peak is observed which corresponds to the collective

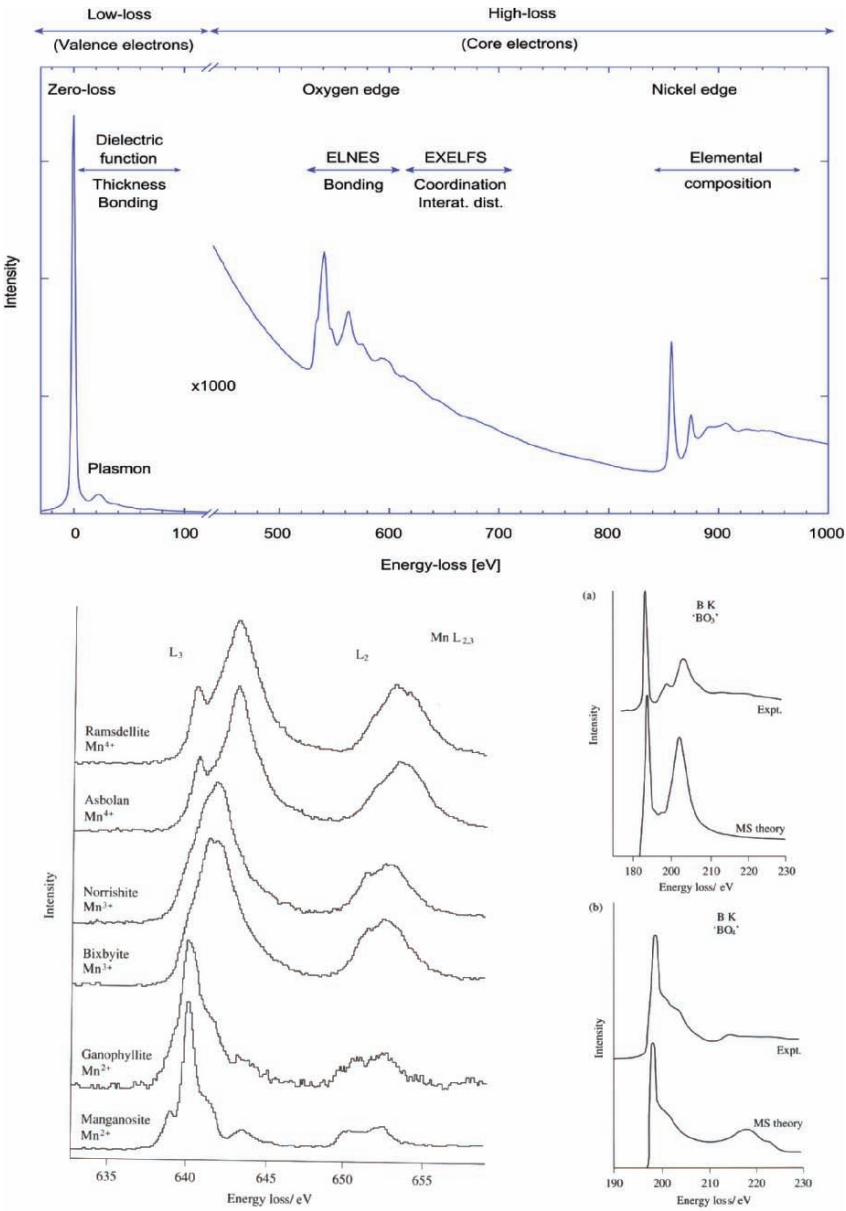

Figure 7.26. Electron energy-loss spectroscopy (EELS) spectra. Shown (top) is a representative EELS spectrum of a nickel oxide sample. A typical EELS spectrum shows a zero-loss peak that represents the unscattered or elastically scattered electrons, the near-edge fine structure (ELNES), and extended energy-loss fine structure (EXELFS). Also shown (bottom) are the "fingerprint" regions of an EELS spectrum, just beyond the core-electron edges, which provide information regarding the detailed bonding and chemical environment of the desired element.[46]

oscillation of many outer-shell (valence or conduction) electrons. The most useful application for this peak is the accurate determination of the sample thickness, of up to several thousand nanometers with a precision of a few percent (Eq. 10).[43] More recently, the plasmon region of the spectrum has been used to delineate variations in the size and geometry of metal nanoparticles.[44] As we saw in Chapter 6, the plasmon resonance frequency is directly related to the effective nuclear charge and size/shape of the charge distribution. Hence, the low-loss region of an EELS spectrum also provides information about bonding interactions and the dielectric function of the sample:

$$T \propto \log\left(\frac{I_p}{I_z}\right), \quad (10)$$

where T is the sample thickness; I_p, the intensity of the plasmon peak; and I_z is the intensity of the zero-loss peak.

At higher energy losses, an EELS spectrum will exhibit a variety of sharp features known as "edges," which are diagnostic for the presence of specific elements. The positions of the edges correspond to the binding energies of the core electrons in the sample. As shown in Figure 7.26 (top), the K-edges for O and Ni are 530 and 860 eV, respectively. Once the background is subtracted, the area under each edge peak(s) is integrated in order to determine the elemental concentrations. The shape of the peak immediately surrounding the edge is aptly referred to as the electron-loss near-edge structure (ELNES). As you might expect, these features are directly dependent on the exact band diagram and density of states (DOS) of the solid being analyzed. As such, this profile may be considered as the electron-scattering counterpart of X-ray absorption near-edge structure (XANES).[45] This region of the spectrum relates to the electronic structure, oxidation state, and bonding hybridization/symmetry of the desired element (Figure 7.26 (bottom)).[47]

Whereas the ELNES region typically extends to *ca.* 20 eV beyond the edge, the extended energy-loss fine structure (EXELFS) provides chemical information from the scattering of electrons by neighboring electrons. Accordingly, this region of the EELS spectrum is the electron-scattering counterpart of extended X-ray absorption fine structure (EXAFS)[42]; both being used to determine nearest-neighbor distances, oxidation states, and coordination numbers of the element being probed (see Figure 7.26 (bottom)).

The spectral fine details from EELS result from dipole-scattering of the incoming electrons. Much like IR spectroscopy, the incoming charged electron is influenced by a vibrating dipole at the sample surface. Hence, the energy loss of the electron is based on the amount of energy that was deposited into the vibrational mode.[48] The compilation of the various regions in an EELS spectrum provides a fingerprint of the surface species being analyzed; hence, this technique is commonly used to probe the localized vibrational modes of chemisorbed molecules on a surface – relevant for the study of any heterogeneous process, including the development of novel catalysts for chemical syntheses, and gas sensors for fuel cell and homeland security applications.[49]

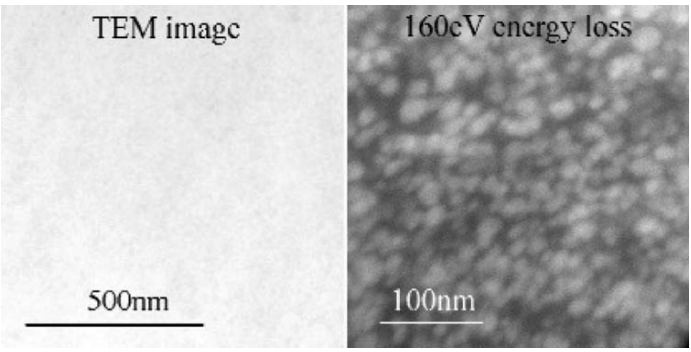

Figure 7.27. Energy-filtered TEM showing silica nanoparticles embedded within an organic coating. The conventional bright-field TEM image (left) shows little/no contrast relative to the EF-TEM image (right).[50]

It should be noted that energy-filtered TEM (EF-TEM) images may be formed with electrons that have lost a specific energy, with respect to a predetermined cut-off energy of the atomic inner shell. Chemical mapping of the surface is possible in this mode, which allows one to determine the exact location of elements in the sample – most useful for surfaces that contain low-Z elements (Figure 7.27). In addition, EF-TEM may be used to illustrate the valence-state distribution of a particular element across a surface, based on slight differences observed in the ELNES region of the EELS spectrum.

7.2.2. Scanning Electron Microscopy (SEM)

In contrast to TEM, with typical sample thicknesses in the range of 10 nm–1 μm, sample depths for SEM often extend into the 10–50 mm range. As such, this technique is most often used to provide a topographic image of the sample surface. However, the electron beam is not confined to the top of the surface, but also interacts with lower depths of the sample. Consequently, SEM provides information regarding the species present at varying depths of the sample (Figure 7.28):

(i) Elastic scattering of electrons by atomic nuclei of the sample results in BSE – useful for generating images based on Z-contrast.
(ii) Inelastic scattering of electrons by sample atoms results in low-energy secondary electrons – useful for providing topographic information regarding the sample surface.
(iii) Inelastic scattering of electrons by sample atoms results in X-ray generation (characteristic and Bremsstrahlung background X-rays) from lower sample depths – useful for chemical analysis of the bulk sample.
(iv) Inelastic scattering results in Auger electrons emitted from sample atoms near the sample surface – useful for surface chemical analysis.

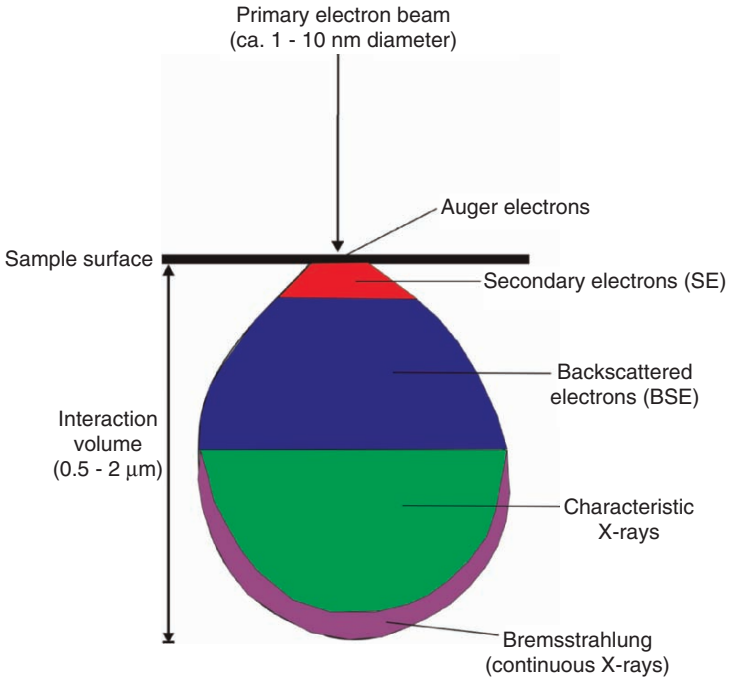

Figure 7.28. Illustration of the sample interaction volume, and the corresponding particles emitted from various sample depths. The exact volume will depend on the accelerating voltage of the electron beam and sample composition.

As you will recall from Figure 7.6b, for imaging and chemical analysis using SEM, the particles generated from the sample must reach the detector situated above the sample surface. Since the relative energies of the generated particles are in the order:

$$\text{Auger electrons} < \text{SE} < \text{BSE} < \text{X-rays}$$

The least energetic emissions will not reach the surface from lower depths of the sample. For instance, Auger electrons that are emitted from deeper regions of the sample lose their energy through collisions with sample atoms before they reach the surface. As a result, AES is a very sensitive technique to probe the chemical composition of only the top 50–100 Å (*i.e.*, 15–30 monolayers). In comparison, the maximum escape depth of secondary electrons has been estimated as 5 nm in metals, and 50 nm in insulators.

Not surprisingly, both the beam current (or accelerating voltage) and sample density will greatly affect the *interaction volume* of the bulk sample with primary electrons (Figures 7.29 and 7.30, respectively). As we saw earlier, the probability for elastic scattering increases with Z^2 (Eq. 9); hence, as the density of the sample increases, the number of BSEs will increase, reducing the number of electrons that may penetrate to deeper regions of the sample. Similarly, as the energy of the incident

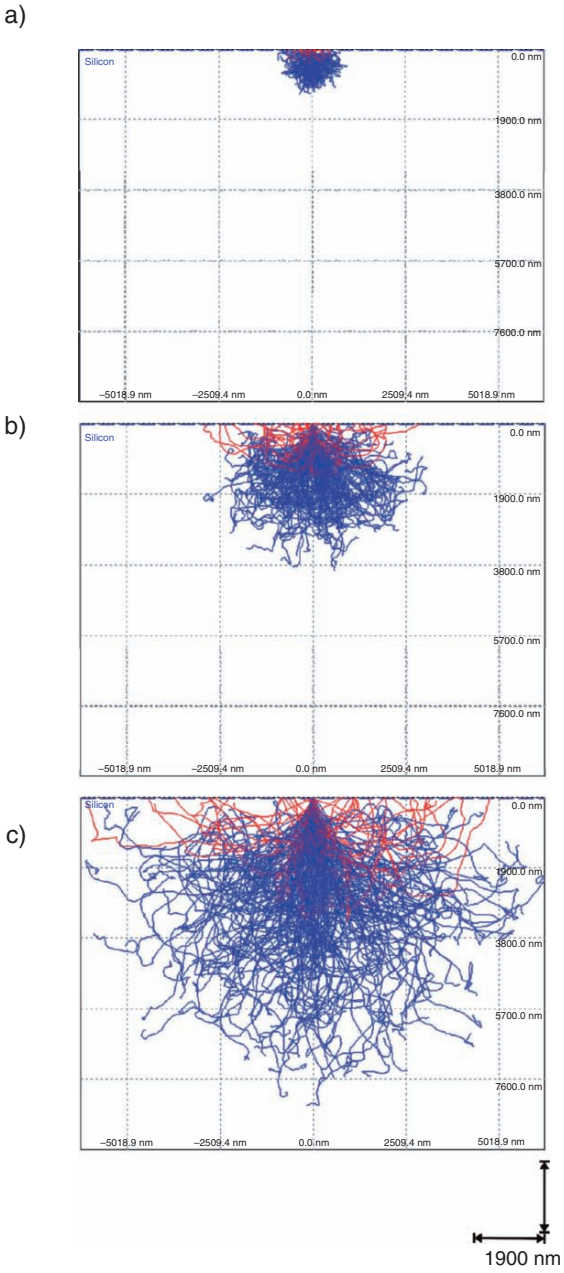

Figure 7.29. Electron-beam penetration volume resulting from varying the beam current. Shown are X-rays (blue) and backscattered electrons (red) generated from a silicon substrate. The beam currents are (a) 10 keV, (b) 20 keV, and (c) 30 keV.[54]

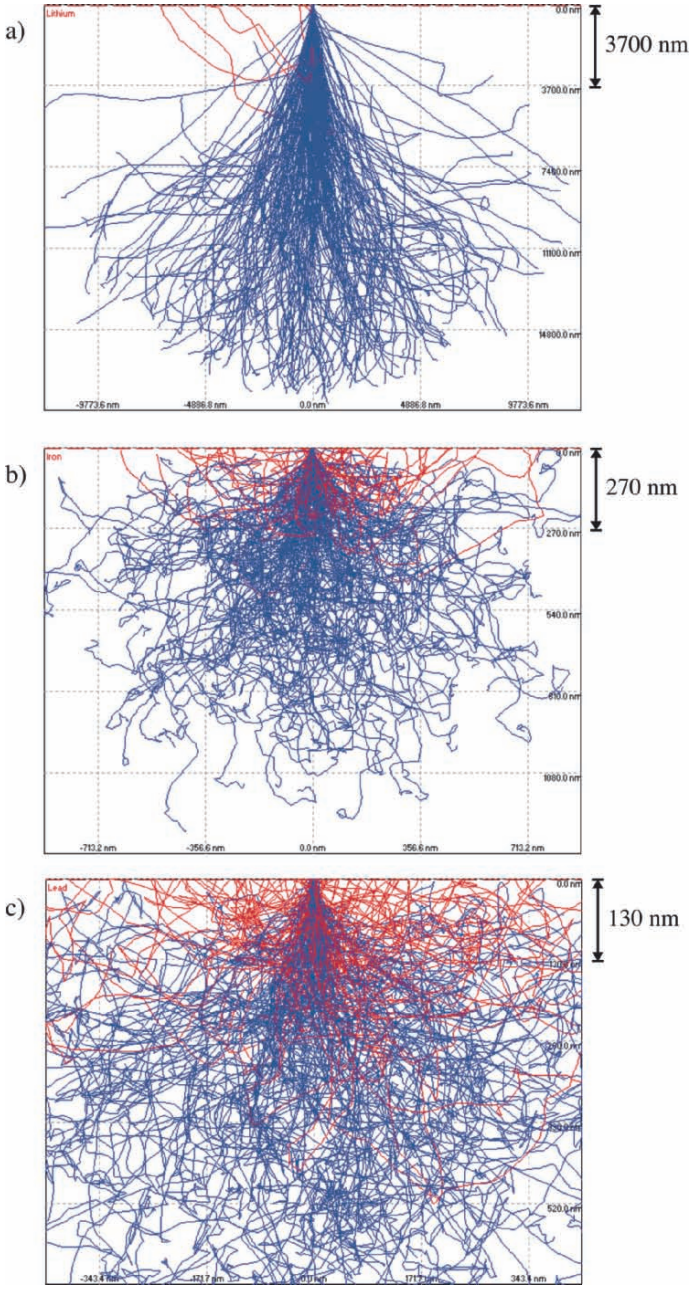

Figure 7.30. Electron-beam penetration volume resulting from varying the sample density. Shown are X-rays (blue) and backscattered electrons (red) resulting from electron beam impingement on (a) Li, (b) Fe, and (c) Pb. The beam current is 20 keV, and beam diameter 10 nm for all metals.[54]

beam decreases, fewer inelastic collisions with sample atoms are needed to bring the electrons to rest, thus decreasing the penetration depth into the sample.

The image formed from SEM is primarily the result of secondary electron emission from sample surface. The Law of Conservation of Energy ensures that any energy lost by the primary beam electrons must be transferred to the secondary electrons that are ejected from the sample atoms.[51] Those with sufficient energy to traverse the sample surface reach an Everhart–Thornley detector, which consists of a scintillator and photomultiplier tube (PMT).[52] The topographical contrast that arises from an uneven surface is due to a differing number of SEs being released from the sample (Figure 7.31).

Structure determination using SEM

In addition to displaying the familiar bright-field images from secondary electron emission, BSE in a SEM may be used to determine the crystallography of (poly)crystalline samples. This technique is referred to as *electron backscattering diffraction* (EBSD) or *backscattering Kikuchi diffraction* (BKD), used to measure individual crystallite orientations, as well as crystallographic parameters of the sample (*e.g.*, interplane spacings/angles, crystal symmetry elements, *etc.*). The EBSD patterns are generated from the interaction of the incident electron beam with a highly tilted (*ca.* 70° from horizontal) planar sample.

When the electrons impinge on the crystalline sample, they interact with individual lattice planes. When these interactions satisfy the Bragg condition, they exhibit backscattering diffraction and (due to the tilted sample) are directed toward a phosphor screen where the fluorescent pattern is detected by a CCD camera. The resulting pattern consists of a large number of intersecting bands, known as Kikuchi lines, which represent the unique crystallographic properties of the crystal

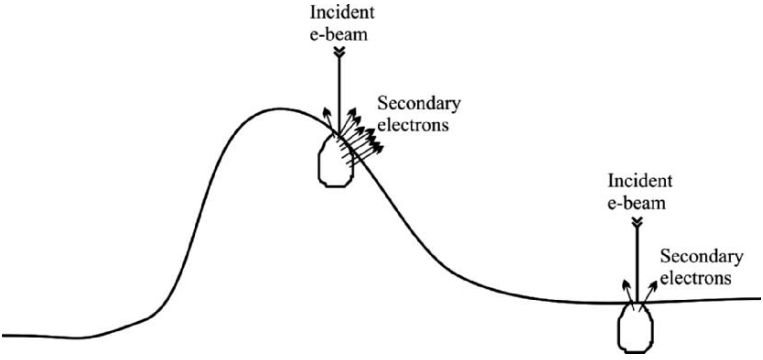

Figure 7.31. Illustration of topographic imaging of a surface using SEM. When the incident beam strikes the side of a feature, many secondary electrons are released from the side and top of the interaction volume ("edge effect"). In comparison, the interaction of the primary beam with a flat substrate releases significantly fewer secondary electrons that originate near the sample surface. The image contrast results from varying numbers of secondary electrons reaching the detector as the beam is rastered across the sample surface.

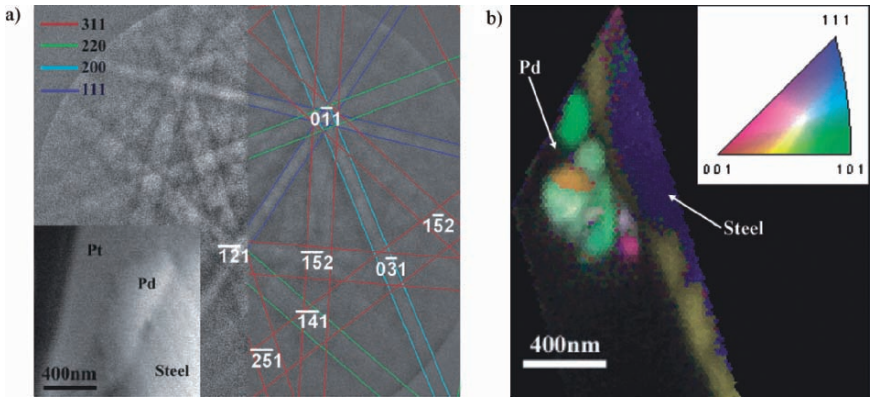

Figure 7.32. (a) SEM micrograph (left bottom inset) of a Pd particulate selected for crystallographic analysis. Also shown are the crisscrossing Kikuchi lines originating from various crystallographic planes. The indices of each plane are indicated in the color legend at the top-left corner. (b) The orientation imaging microscopic (OIM) profile of the Pd particulate, showing a microcrystalline array (color-coated based on the crystallite orientations). Reproduced with permission from Bera, D.; Kuiry, S. C.; Seal, S. *J. Phys. Chem. B* **2004**, *108*, 556. Copyright 2004 American Chemical Society.

(Figure 7.32a). Computer software is used to collect/analyze the resulting patterns to determine the crystallography of the material.[53] In association with compositional data from EDS, the exact phase of the material may be identified from a library of known materials. For a more thorough crystallographic description, *orientation imaging microscopy* (OIM) is often carried out in tandem with EBSD. This technique consists of stepping the beam across the sample, with automatic indexing of the resulting EBSD patterns. The resulting OIM map readily reveals the crystallographic orientations and grain boundaries in three-dimensions (Figure 7.32b) – of use for applications such as sensor/heterogeneous catalyst design and micro/nano defect analyses.

Sample considerations and AES

Sample preparation for SEM analysis is trivial relative to TEM, with the sample simply deposited onto the top of an adhesive fastened to an aluminum stub/holder. Most often, conductive carbon tape is used to sequester the sample; for FESEM, problems with outgasing usually dictates the use of carbon/silver paint, epoxy, or copper/aluminum tape with adequate drying prior to analysis. After allowing the solvent to fully evaporate (if present), a thin conductive film (*ca.* <10 nm) of Au or C is often deposited onto the sample surface.[55] This is especially required if a nonconductive adhesive is used to mount the sample, or if the sample itself is nonconductive. The preparative steps involving conductive mounting materials is important to prevent *charging* – the buildup of electrons on the sample surface, which dramatically affects the imaging ability of the SEM (Figure 7.33). Sometimes, it is even necessary to use an additional amount of carbon paste or tape to create a conductive path between a tall sample and the aluminum holder. It should be noted that metallic

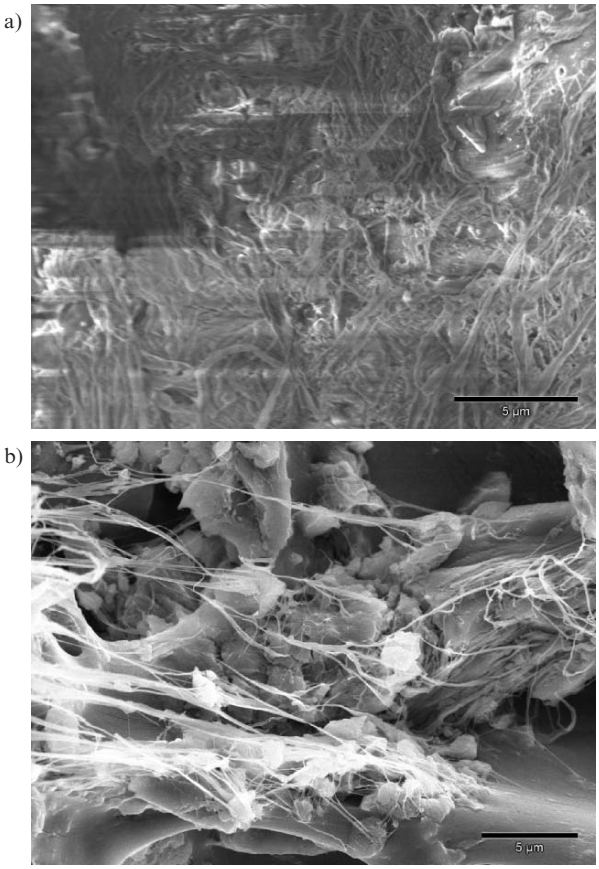

Figure 7.33. SEM images of amorphous carbon nanofibers (nonconductive) grown at room temperature from a dendritic catalyst. Shown is (a) as-formed nanofibers, without a gold coating and (b) after sputtering a thin conductive gold coating on the surface. The uncoated sample exhibited extreme charging (a), which thermally degraded the sample and caused movement of the sample during imaging.[60]

coatings also serve another important use – to increase the SE emission of a sample with a low yield of secondary electrons (*e.g.*, comprising low-Z elements).

In addition to imaging applications, SEM is also widely used for elemental analysis and chemical mapping of surfaces, using EDS/WDS. However, unlike TEM, facile cross-section imaging/chemical mapping may also be performed using specialized sample holders (Figure 7.34). Besides monitoring characteristic X-rays from sample elements, Auger electron emission may be analyzed – a technique known as AES (Figure 7.35a). Analogous to the STEM extension of TEM, scanning auger microscopy (SAM) is also possible, wherein the incident electron beam is scanned across the sample. Perhaps the most intriguing aspect of AES/SAM instruments is the capability of depth profiling. An argon ion beam is used to etch away monolayers of the surface, allowing for compositional studies as a function of sample depth (Figure 7.35b).

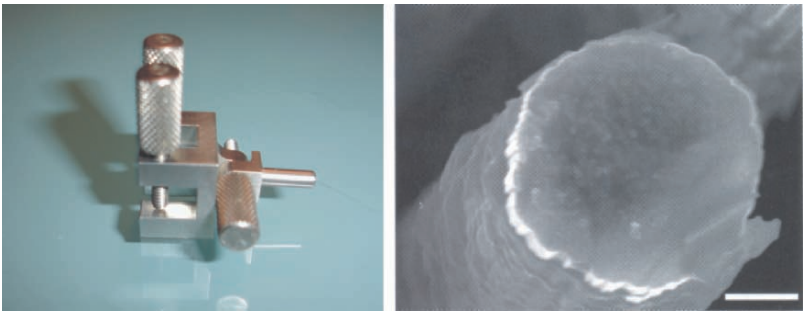

Figure 7.34. Photograph of a variable-angle SEM sample holder, with an example of a cross-section SEM image (scale bar is 2 μm).[61]

A simple way to distinguish between SEM and SAM is the former collects secondary electrons to form an image; the latter collects Auger electrons for chemical analysis. Recent developments have now afforded dual-detector electron microscopes that are equipped with standard FESEM/EDS capabilities in addition to SAM. This powerful combination offers the direct superimposing of both EDS and SAM chemical maps onto the corresponding high-resolution image.[56] In addition to being more sensitive for light elements (±0.5 at% for Li–U), it should be noted that AES is more suited for surface analysis than EDS. Due to the low kinetic energies of Auger electrons (*ca*. 50 eV–3 keV), chemical information is only obtained from sample depths of *ca.* <50 Å (compared to 1–2 μm for EDS). As such, it is not always possible to coat the sample to prevent charging, which explains why SAM is most often applied for compositional studies of conductive samples.[57]

Environmental SEM

Though the analysis of samples in the presence of solvent is normally a *faux pas* for the UHV environment of any electron microscope, there are now instruments known as *environmental SEMs* (ESEMs) that are capable of such studies. These instruments have been in development since the early 1970s,[58] for *in situ* studies of virtually any material (wet/dry, insulating/conducting). Before this major technological development, samples such as paints, inks, and biological specimens had to be dried completely to maintain the integrity of the vacuum system. Typically, an ESEM is not simply a modified SEM, but rather a specially designed instrument that is capable of regular (FE)SEM imaging, as well as "wet mode" operation.[59]

The operation of an ESEM is made possible through use of a differential pumping system (Figure 7.36) that maintains a UHV environment (10^{-7} Torr) required for the electron gun, while allowing the presence of gases in the sample chamber (10–20 Torr). The pressure and temperature of the sample chamber may be strictly controlled, inducing evaporation or condensation events.

The nonvacuum conditions within the sample chamber require a different type of detection system relative to conventional SEMs, referred to as a *gaseous secondary*

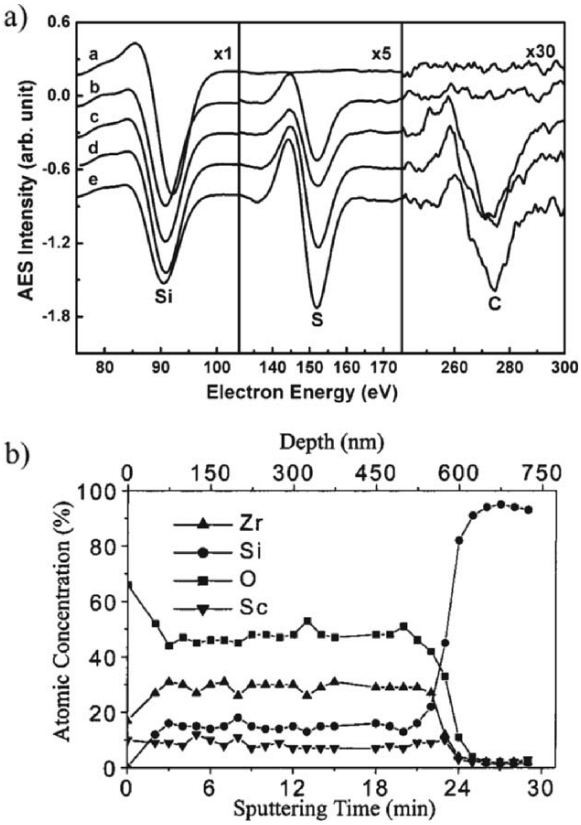

Figure 7.35. (a) AES analysis of organosulfur compounds adsorbed onto Si(100). Shown are the Si(LVV), S(LVV), and C(KLL) transitions for (a) clean Si(100), and after saturation exposure by (b) H_2S, (c) CH_3SCH_3, (d) CH_3SH, and (e) CH_3SSCH_3.[62] (b) AES depth profile for a $(Sc_2O_3)_{0.08}(ZrO_2)_{0.92}$ thin film deposited onto a Si(100) wafer. This profile shows a homogeneous Sc:Zr:O:Si atomic ratio between 75 and 500 nm, with an interdiffusion layer thickness of <100 nm. By examining the rise of the Si peak, the film thickness can be readily determined.[63]

electron detector (GSED). Due to the energetic nature of the primary beam, there is little scatter from its interaction with the gaseous medium about the sample. *En route* toward the positive electrode, the secondary electrons generated from the sample repeatedly collide with gas molecules, generating a cascade of additional electrons and positive ions (Figure 7.36). In addition to amplifying the SE signal, the positive ions migrate back to the sample surface where they dissipate the charge buildup – hence, precluding the need for conductive samples or carbon/gold coating. The aperature diameter through which the primary electron beam is passed determines the overall maximum pressure of the sample chamber. For instance, a 0.5 mm aperature dictates a maximum pressure of 10 Torr about the sample; a 1 mm aperature would lower the maximum pressure to 5 Torr.

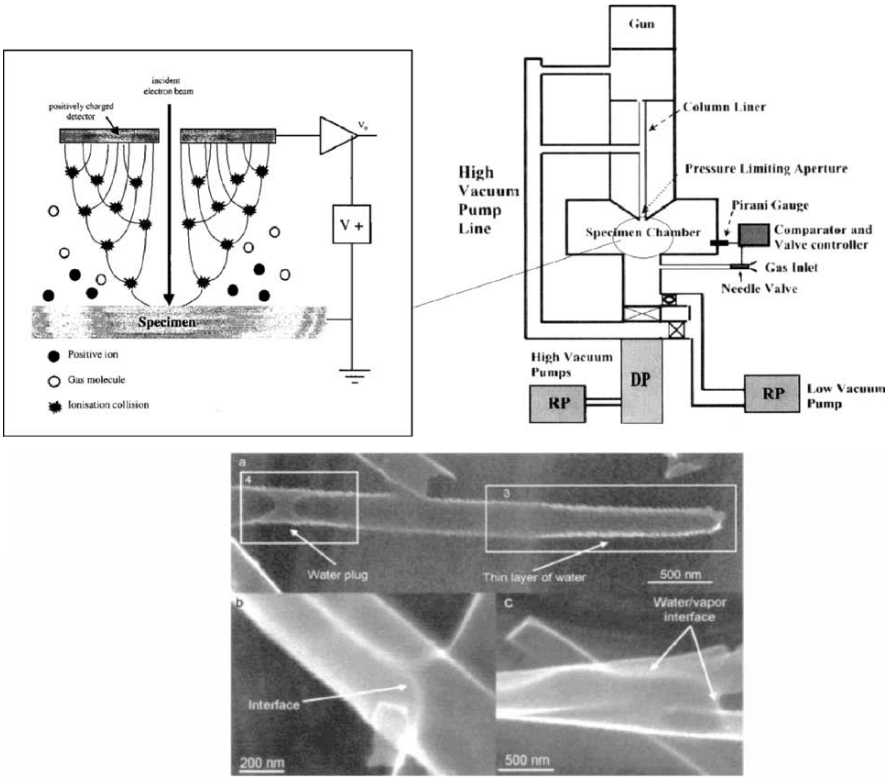

Figure 7.36. Schematic of the differential pumping arrangement of an ESEM (top right)[52] and the cascade amplification process occurring in the gaseous secondary electron detector (GSED) (top left).[64] The abbreviations RP and DP refer to the rough pump and diffusion pump, respectively. Also shown (bottom) is an intriguing application for ESEM – the *in situ* imaging of water condensation inside a carbon nanotube (a), and underneath/around the CNT (b, c).[65]

7.2.3. Photoelectron Spectroscopy

The photoelectric effect, first outlined by Einstein in the early 1900s, refers to the ejection of electrons from a surface due to photon impingement. However, it was not until the 1960s that this phenomenon was exploited for surface analysis – a technique referred to as *X-ray photoelectron spectroscopy* (XPS), or *electron spectroscopy for chemical analysis* (ESCA). This technique consists of the irradiation of a sample with monochromatic X-rays (*e.g.*, Al K_α (1.487 keV), Mg K_α (1.254 keV), Ti K_α (2.040 keV)), which releases photoelectrons from the sample surface (Figure 7.37).[66] Due to the short *free mean path* (FMP) of the photoelectrons in the solid, this technique provides compositional information from only the top 1–5 nm of a sample.

Each atom in the sample has characteristic binding energies of their inner-shell electrons, referred to as *absorption edges*. In order to excite the electrons, the energy

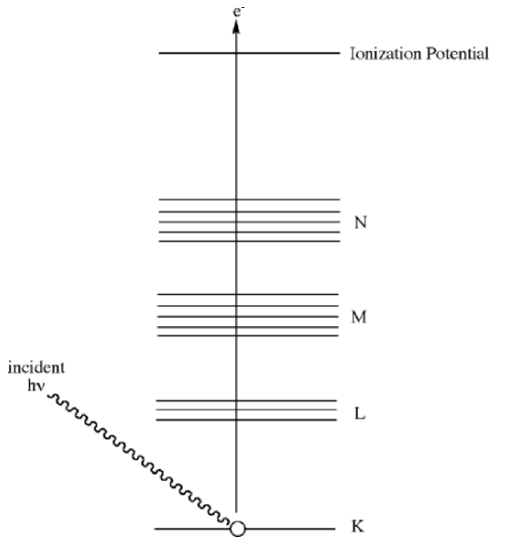

Figure 7.37. The energy-level diagram for X-ray photoelectron spectroscopy (XPS).

of the incident photons must be at least as large as the binding energy of the electrons. When this energy threshold is exceeded, a large absorption of energy takes place, followed by the release of photoelectrons with excess kinetic energy (Eq. 11) in order to relax the atom back to its stable ground state. Since the binding energy of an atom is altered by minute changes in its chemical environment (*e.g.*, oxidation state, hybridization/geometry, *etc.*), XPS provides both elemental quantification and details regarding the chemical environment of the surface atoms (Figure 7.38) [67]:

$$E_k = h\nu - E_b, \tag{11}$$

where E_k is the kinetic energy of the emitted photoelectrons; $h\nu$, the energy of the incident photons; and E_b is the binding energy of the inner-shell electrons.

In addition to using X-rays to irradiate a surface, ultraviolet light may be used as the source for *photoelectron spectroscopy* (PES). This technique, known as *ultraviolet photoelectron spectroscopy* (UPS, Figure 7.38), is usually carried out using two He lines (HeI at 21.2 eV and HeII at 40.8 eV), or a synchrotron source. This technique is often referred to as "soft PES," since the low photon energy is not sufficient to excite the inner-shell electrons, but rather results in photoelectron emission from valence band electrons – useful to characterize surface species based on their bonding motifs. It should be noted that both UPS and XPS are often performed in tandem with an Ar^+ source, allowing for chemical analysis of the sample at depths of $\leq 1\,\mu m$ below the surface.

Though a typical XPS detector collects all emitted photons, regardless of their ejection angles, it should be noted that *angle-resolved* XPS (ARPES) and UPS (ARUPS) may also be carried out. By detecting photoelectrons emitted from a surface at different emission angles, one obtains the energy of the electrons as a function

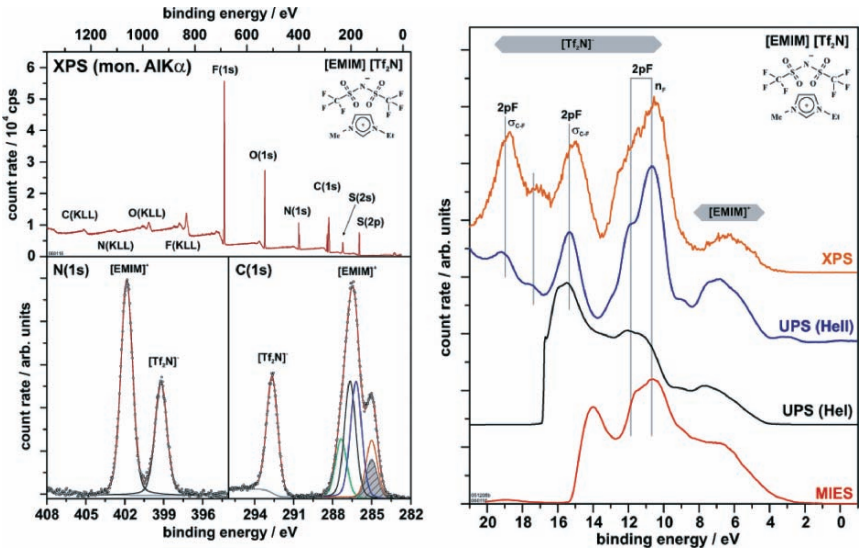

Figure 7.38. XPS spectrum of an ionic liquid, [EMIM][Tf_2N], detailing the C(1s) and N(1s) regions. Since there are no peaks from the Au substrate, the film thickness is likely >10 nm. Also shown (right) is the comparison between XPS, ultraviolet photoelectron spectroscopy (UPS, HeI = 21.2 eV, HeII = 40.8 eV radiation), and metastable impact electron spectroscopy (MIES). Whereas XPS and UPS provide information from the first few monolayers of a sample, MIES is used for zero-depth (surface only) analysis, since the probe atoms are excited He atoms that interact with only the topmost layer of sample. Full interpretations for these spectra may be found in the original work: Hofft, O.; Bahr, S.; Himmerlich, M.; Krischok, S.; Schaefer, J. A.; Kempter, V. *Langmuir* **2006**, *22*, 7120. Copyright 2006 American Chemical Society.

of the momentum vector, **k**. This is referred to as "band mapping," since this analysis probes the electronic structure of crystalline materials.[68]

Structure determination using XAFS

If a tunable X-ray source such as synchrotron radiation[69] is used to generate the incident photons rather than a monochromatic beam, one can select specific absorption edges to gain more detailed information regarding the chemical environment of specific atoms. This technique, known as XAFS, is divided into two spectral regions – XANES and EXAFS – which are analogous to ELNES and ELEFS in EELS studies. Whereas XANES is sensitive to the oxidation state and bonding geometry of the probed element, EXAFS is useful to determine the distances and coordination numbers of neighboring species.[70] The small oscillations that are present in an EXAFS spectrum are indicative of the interference effects that occur as the photoelectrons leave the sample surface. As you might expect, this backscattering effect becomes most pronounced with increasing photon energies, and with smaller interatomic distances between the probed atom and its nearest neighbors. As a further extension of this technique, the X-rays may be reflected from a surface at an angle in order to yield even more structural information. This technique is referred to as

total external reflection EXAFS, or REFLEXAFS,[71] particularly useful to determine chemical information from greater sample depths without the need for destructive Ar^+ etching.

In order to illustrate the complementary information yielded from XPS and XAFS, we will consider the recent work of Gervasini and coworkers, regarding the characterization of CuO catalysts dispersed on silica and silica/alumina supports.[72] The XANES, EXAFS, and XPS spectra for these catalyst species are illustrated in Figure 7.39. The EXAFS spectrum (Cu K-edge) for a $Cu/SiO_2/Al_2O_3$ catalyst, calcined in air, has one primary peak at 1.939 Å corresponding to an (octahedral) environment of six O atoms (Figure 7.39a, thick line).[73] The lack of other O shells suggests that the surface contains isolated Cu ions, likely as a Cu-aluminate phase. In contrast, the same catalyst on a SiO_2 support (Figure 7.39a, thin line) shows the same octahedral environment of O atoms (1.947 Å), and another large peak corresponding to *ca*. 5 Cu atoms at an average Cu-Cu distance of 2.987 Å. Since this is shorter than the Cu-Cu distances in crystalline CuO, the EXAFS spectrum suggests the formation of amorphous CuO aggregates on the SiO_2 support.

After reduction of the catalyst in a H_2 stream at the same temperature as calcination (Figure 7.39b), the Cu/SiO_2 spectrum shows a large peak at 2.547 Å, corresponding to *ca*. 8 Cu atoms. The spectrum closely matches that of the fcc metallic Cu reference, suggesting the presence of small metallic Cu atoms on the surface. On the Si/Al support, the same spectral features are observed; however, line-fitting indicates that the Cu atoms are somewhat electropositive until further reduction takes place at higher temperatures. It was postulated that this resistance toward reduction is likely due to the strong association of surface Cu ions with Lewis acidic aluminum centers of the support.

Not surprisingly, the XANES spectra of Cu/Si and Cu/SiAl (Figure 7.39c) correspond to the absorption edge of Cu^{2+}. However, the spectra are significantly different from the CuO reference. This suggests the presence of a distorted octahedral geometry about the Cu ions, where the Cu may be bound to three different types of O atoms: (i) from the support, (ii) from surface –OH groups, and (iii) from water molecules.

The XPS spectra (Figure 7.39d,e) show a broad peak at 934 eV, corresponding to the Cu L-edge of Cu(2p $\rightarrow$ 3d transition). Since the binding energy for Cu^{2+} and Cu^+ are similar (*i.e.*, 933.6 and 932.5 eV, respectively), the shape of the Cu 2p peaks was examined in detail to determine the valence states of the surface Cu species. Whereas Cu on Si/Al exhibits one contribution, Cu on a SiO_2 support shows the presence of two different Cu species. In particular, this suggests that the Cu^{2+} ions interact with both =O and –OH groups from the silica support. Furthermore, satellite peaks from the spin–orbit components[74] (*i.e.*, $Cu(p_{1/2})$ and $Cu(p_{3/2})$) of the Cu(2p) peak are observed only for Cu on a SiO_2 support; this suggests that the Si/Al support contains Cu atoms in a lower valence state, such as Cu^+ speciation.[75]

Lastly, XPS was also used to gleam information regarding the dispersion of Cu on the two surfaces. The $Cu(2p_{3/2})$, Si(2s), and Al(2p) peaks were integrated to yield the respective elemental concentrations of each supported catalyst. The molar ratios between the surface species (*i.e.*, Cu(2p)/Si(2s) or Cu(2p)/Si(2s) + Al(2p)) and the total metal species (*i.e.*, Cu/Si or Cu/(Si + Al), as obtained from inductively

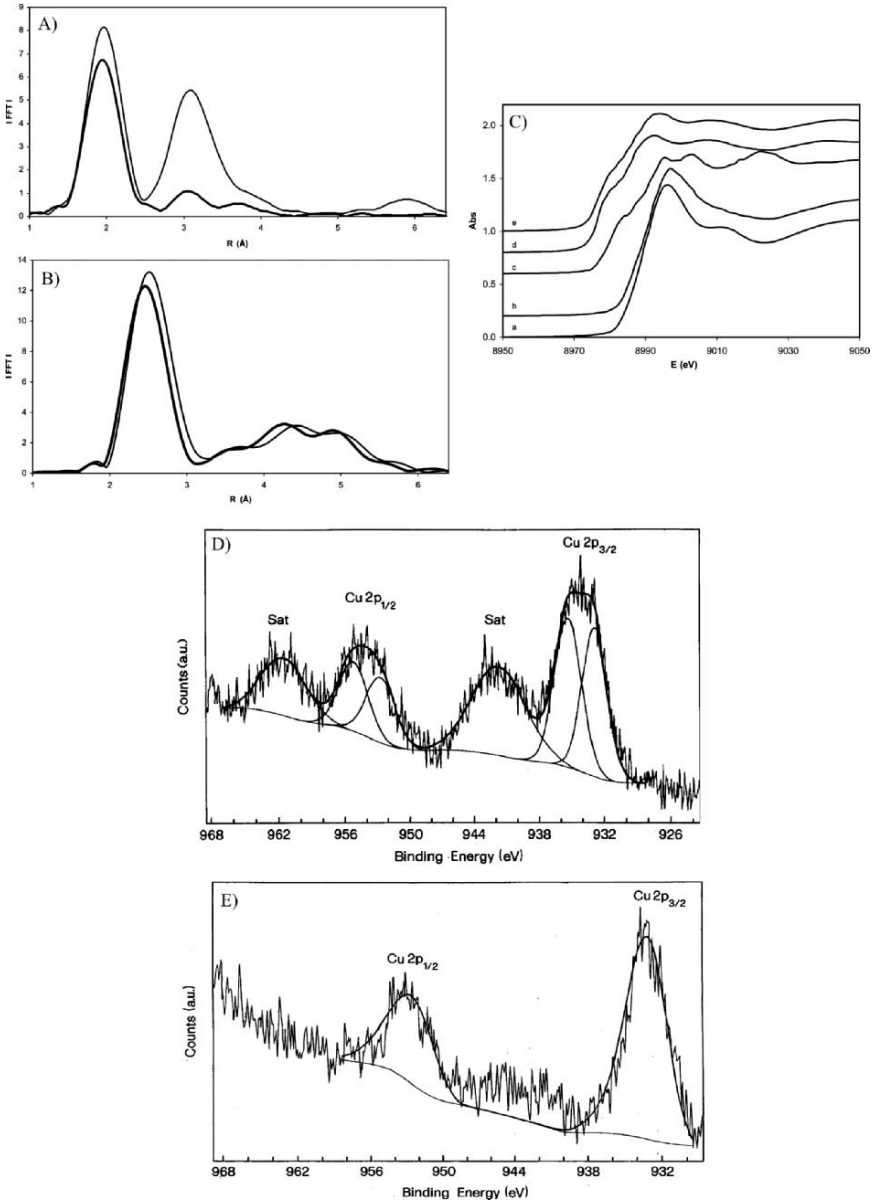

Figure 7.39. XAFS CASE STUDY: surface characterization of dispersed CuO catalysts on silica and alumina/silica supports. Shown are: (A) EXAFS of the Cu K-edge of the catalyst calcined in air at 543 K. The thick and thin lines indicate Si/Al and Si supports, respectively; (B) EXAFS of the Cu K-edge of the catalyst reduced under a H_2 flow at 543 K; (C) Cu K-edge XANES spectra of the calcined catalyst on (a) SiO_2, (b) SiO_2/Al_2O_3 supports, along with references of (c) Cu foil, (d) Cu_2O, and (e) CuO; (D) XPS spectrum of the Cu 2p core level of the calcined catalyst on a Si support; (E) XPS spectrum of the catalyst on a Si/Al support. Reproduced with permission from Gervasini, A.; Manzoli, M.; Martra, G.; Ponti, A.; Ravasio, N.; Sordelli, L.; Zaccheria, F. *J. Phys. Chem. B* **2006**, *110*, 7851.

coupled plasma (ICP) analysis) resulted in values near 1.0 and 0.35 for the SiO_2 and SiO_2/Al_2O_3 supports, respectively. The surface deficiency of Cu on the Si/Al support is proposed to be an artifact of Cu encasement within the pores of aluminum-rich regions, as also suggested from XAFS.

7.3. SURFACE CHARACTERIZATION TECHNIQUES BASED ON ION BOMBARDMENT

Thus far, the majority of surface techniques have employed the "collide and collect" principle, where either electrons or X-rays impinge on the sample, and various emissions are collected/analyzed. However, a number of other ions may also be used for such bombardment-based analyses. For instance, we already saw an example (Figure 7.38) of *metastable impact electron spectroscopy* (MIES), in which metastable He atoms (in an excited $2s^1$ state, with an energy of 19.8 eV and a lifetime of *ca*. 4,000 s) are directed toward a sample. As the atom collides with the sample, the 2s electron tunnels into an empty valence orbital in a sample atom, releasing an Auger electron. A similar surface-relaxation mode may be carried out by incident He ions, which is termed *ion neutralization spectroscopy* (INS). Since the incident atoms/ions are not sufficiently energetic, the beam does not penetrate through the sample surface. Hence, the spectra resulting from these techniques provide information regarding the DOS for the topmost surface monolayer of the sample.[76]

If a high-energy beam (2–4 MeV) of He (α-particles) or H ions[77] collides with a surface, information may be gained regarding the composition and thickness of a surface coating (Figure 7.40). This technique is known as *Rutherford backscattering* (RBS), very similar to the original scattering experiments conducted by Rutherford in the early 1900s – essential in the early development of a structural description of the atom. As the energetic ion penetrates the material, it loses energy through collisions with electrons, and (less frequently) with nuclei. When the positively charged He^+ ion approaches the nucleus of a sample atom, it will be electrostatically repelled. As you would expect, the energy of the backscattered ions will depend on their incident energy, as well as the mass of the surface atom that causes the scattering. For instance, contact with high-Z atoms such as gold, will result in the energy of the backscattered ions being almost equivalent as the incident beam. By measuring the energy spectrum of the backscattered ions, information on the composition of the elements, and their origination depth from the sample may be obtained. Hence, RBS provides facile compositional information regarding a sample, without the need for a reference sample.[78] This technique is most often applied to determine the chemical composition versus depth for heavy elements in a low-Z matrix, amenable for thicknesses of up to 0.5 μm (for He ions) and 10 μm (for H ions).

Based on our previous discussions, it is logical to assume that high-energy ions may dislodge inner-shell electrons, releasing characteristic X-rays (*cf.* EDS). This is the theoretical principle underlying *particle-induced X-ray emission* (PIXE), which uses high-energy H^+ or He^+ ions (at >2 MeV; produced from a van de Graaff accelerator[79]) as the incident beam. This technique offers a nondestructive quantitative analysis of a sample (for elements with $Z \geq 13$), often used by archaeologist

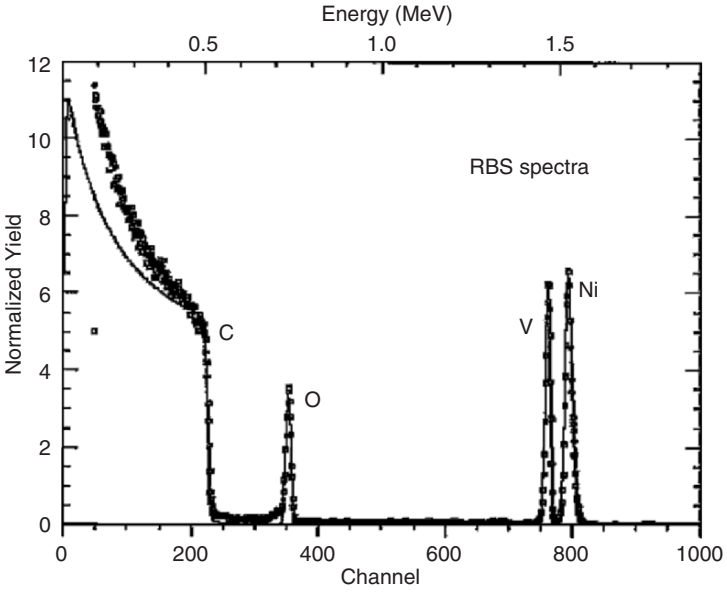

Figure 7.40. Rutherford backscattering (RBS) spectrum of a $LiNiVO_4$ film (thickness of 240(±5) Å) on a carbon substrate. The open squares represent the experimental RBS data, and the continuous line is the simulated data. Reproduced with permission from Reddy, M. V.; Pecquenard, B.; Vinatier, P.; Levasseur, A. *J. Phys. Chem. B* **2006**, *110*, 4301. Copyright 2006 American Chemical Society.

and art curators to assist with dating and authenticity assessments. With low detection limits (*ca.* 1–10 ppm), and ability to analyze a number of elements simultaneously, PIXE has also been widely used for the rapid analysis of multilayer thin films for microelectronics and optoelectronics applications. A recent extension, known as micro-PIXE, allows one to focus the ion beam to a diameter of *ca.* 1 μm, to allow for a more localized analysis (Figure 7.41). The primary benefit of this technique is the wide variety of samples that may be analyzed, from liquids to powders. Though no sample preparation is necessary for PIXE, it should be noted that the analysis is limited to the top 10–50 μm of the sample, depending on its density.

Among the techniques discussed thus far, the best Z-cutoff for elemental composition techniques has been Li (for XPS and AES). One ion-bombardment method, *elastic recoil detection analysis* (ERDA),[80] is able to nondestructively quantify light elements such as hydrogen or deuterium.[81] This technique uses a high-energy ion beam (*e.g.*, He, Au, Cl, C, or O ions), which causes light elements to be elastically ejected from the surface (*i.e.*, "recoiled") due to interactions between the incident beam and their atomic nuclei (Figure 7.42). By choice of the correct angle between the sample surface and detector, the incident beam is blocked by "stopper foil" to increase the signal/noise ratio for the measurement.

The most common mode of chemical analysis presented herein has been the monitoring of elastically/inelastically scattered or recoiled incident beam species, or

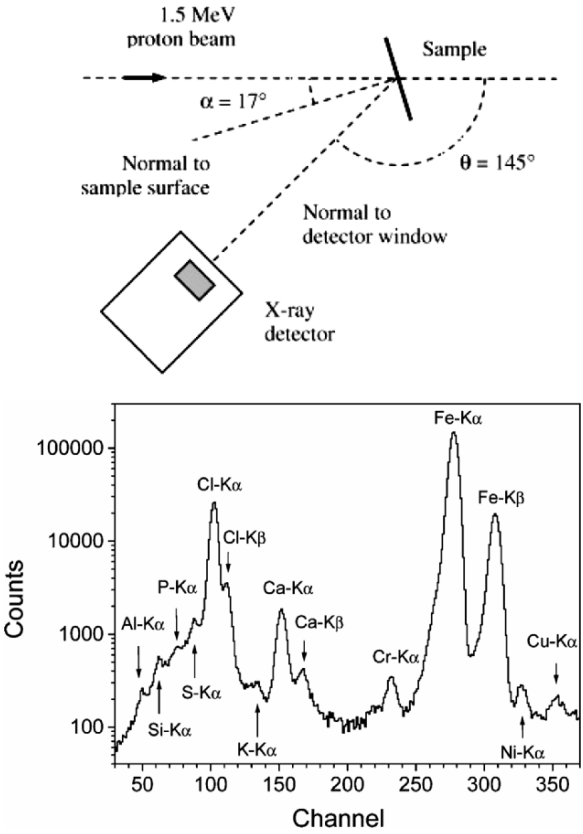

Figure 7.41. Experimental setup and X-ray spectrum resulting from PIXE analysis of single-walled carbon nanotubes. Reproduced with permission from Naab, F. U.; Holland, O. W.; Duggan, J. L.; McDaniel, F. D. *J. Phys. Chem. B* **2005**, *109*, 1415. Copyright 2005 American Chemical Society.

the analysis of a secondary emission pattern. In addition to the release of characteristic X-rays, Auger electrons, and photoelectrons, an incident beam may cause ionization of the sample. This technique is known as *secondary-ion mass spectrometry* (SIMS),[82] which represents the most sensitive surface characterization technique developed to date, with detection limits of 10^{10}–10^{15} atoms cm^{-3} (*i.e.*, 0.1 ppb − 0.1 ppm) and ability to detect/quantify any element in the Periodic Table. In contrast to common bulk MS methods such as matrix-assisted laser desorption/ionization (MALDI)[83] and electrospray ionization (ESI),[84] SIMS analyzes samples in their native state without the need for a suitable matrix solution. As a result, SIMS is the best choice to characterize organic-based thin films and polymer surfaces.

The operating principle of SIMS is not unlike other techniques in this section; that is, a high-energy (1–30 keV) ion source is directed onto a sample surface. However, the absorption of this energy by the top *ca.* 50 Å of the sample results in the sputtering

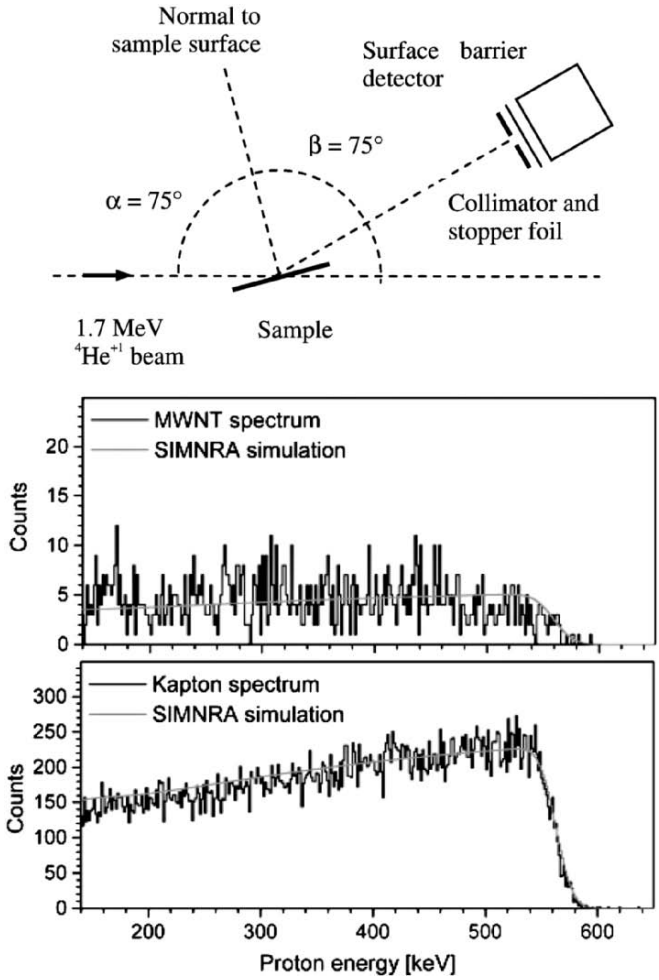

Figure 7.42. Experimental setup and eastic recoil detection (ERD) spectra for multiwalled nanotubes, and a Kapton polyimide film. A computer program, SIMRA, is useful to simulate ERD as well as other non-RBS data. Reproduced with permission from Naab, F. U.; Holland, O. W.; Duggan, J. L.; McDaniel, F. D. *J. Phys. Chem. B* **2005**, *109*, 1415. Copyright 2005 American Chemical Society.

of neutral and charged $(+/-)$ species from the surface.[85] These ejected species primarily include neutral atoms and atomic clusters; however, charged molecular fragments are also released from the surface. Analogous to a traditional mass spectrometer, SIMS analyzes these secondary ions based on their relative mass/charge (m/z) ratios (Figure 7.43).

Depending on the desired species to be analyzed, a variety of primary ion beams may be used such as Cs^+, O_2^+, O, Ar^+, and Ga^+. Whereas a cationic primary beam such as Cs^+ is used to ionize electronegative elements (*e.g.*, O, C, N, chalcogens,

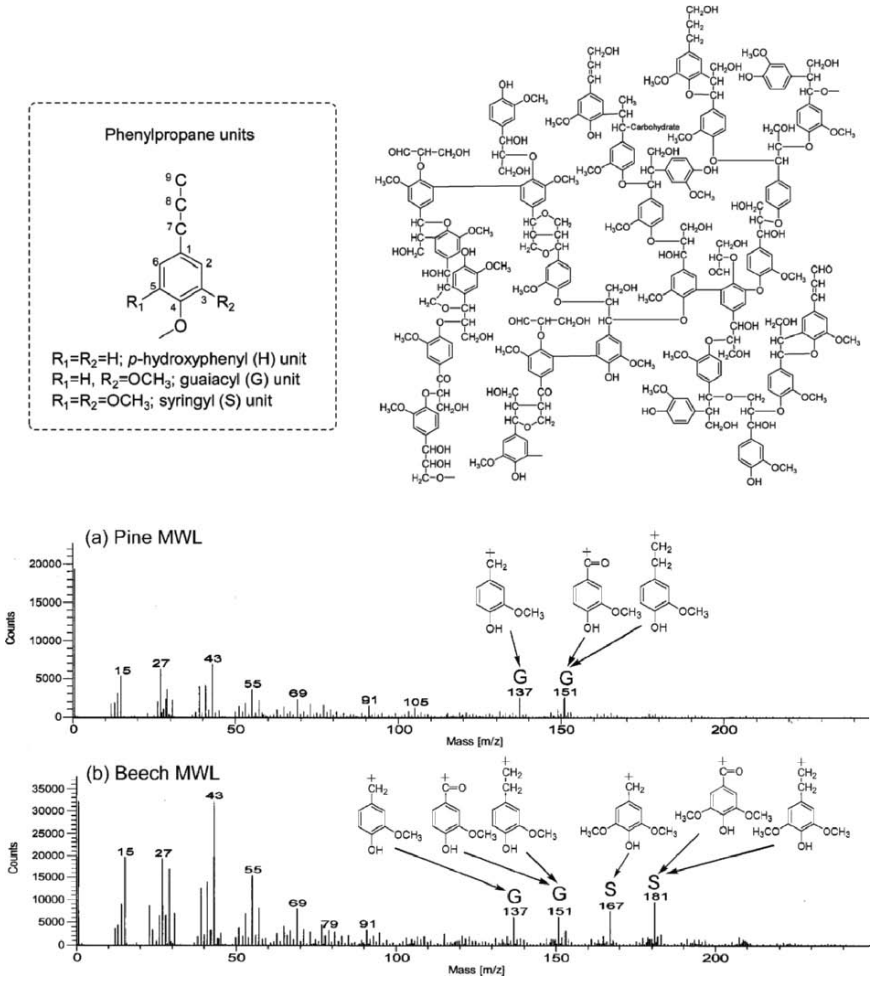

Figure 7.43. SIMS analysis of lignin, the second most abundant biopolymer in nature, following cellulose. Shown is the phenylpropane subunits and a structural model of softwood lignin (top). The secondary-ion mass spectra of pine (softwood) and beech (hardwood) milled wood lignin (MWL, a solvent-extracted form of lignin from beech wood) are also shown (bottom). Reproduced with permission from Saito, K.; Kato, T.; Tsuji, Y.; Fukushima, K. *Biomacromolecules* **2005**, *6*, 678. Copyright 2005 American Chemical Society.

halogens, *etc*.), oxygen atoms are used to ionize electropositive elements (*e.g.*, Li, Mg, Na, B, Al, *etc*.). Liquid metal ion beams (*e.g.*, Ga, Au/Ge) are used for high-resolution studies, since the beam may be focused to a smaller diameter (<50 nm) for micron and nanoscale analyses.

There are two varieties of SIMS – static and dynamic. *Static SIMS* (often referred to as time-of-flight SIMS, TOF-SIMS) is often the method-of-choice, used for

elemental analysis and imaging of the top 2–3 monolayers of a sample; in comparison, *dynamic SIMS* is used to determine elemental concentrations of the sample, as a function of depth. As such, dynamic SIMS is a destructive technique primarily used for depth profiling, whereas TOF-SIMS does not appreciably deteriorate the surface being analyzed. For instance, due to a slow, controllable sputtering rate, the entire analysis may be performed without removing less than 1/10 of an atomic monolayer.

It should be noted that any SIMS analysis will at least result in surface roughness/cratering and elemental mixing within the outermost monolayers. When the primary beam interacts with surface atoms, the incident energy is transferred to target atoms through a series of binary collisions. Some atoms/fragments receive sufficient energy to be recoiled through the sample surface and are removed from the material. However, other less noticeable effects will result such as the implanting of primary ions, and mixing with sample atoms at depths of $\leq$10 nm below the surface. The magnitude of these effects is governed by the incident beam,[86] as well as the crystallinity and surface defects of the sample.

Dynamic SIMS typically uses a quadrupole mass analyzer; however, a TOF mass analyzer offers much higher sensitivities (with limitations, *vide infra*) and mass ranges. In a TOF-SIMS, an ion of known electrical charge, but unknown mass, is accelerated by an electrical field. As a result, all ions of the same charge will have identical kinetic energies. However, the velocity of the ion will depend on the mass/charge ratio, which affects the time it takes for the charged species to reach the detector. That is, light ions will reach the detector before heavier species, allowing for effective mass separation and analysis. It should be noted that each pulse of the primary ion beam produces a full spectrum of secondary ions. Hence, the highest mass resolution is afforded by using the shortest pulse of the primary ion beam, since the time-of-flight for ions may be determined more precisely.

The sputtering event will yield secondary ions with a range of kinetic energies. Whereas atoms will contain their kinetic energy only in translational modes, charged molecular fragments will have the kinetic energy spread over translational, vibrational and rotational modes. By varying the accelerating voltage of the electrostatic ion energy analyzer, one is able to select secondary ions (*e.g.*, monoatomic *vs.* multiatomic (molecular fragments)) based solely on their translational energies. For instance, ions with a lower energy are deflected at larger angles, which prevents them from passing through to the mass analyzer.

Due to more energetic collisions, an incident beams consisting of either heavier ions (*e.g.*, Au^+ *vs.* Ga^+), or polyatomic species (*e.g.*, $C_{60}{}^+$,[87] $Au_3{}^+$, $SF_5{}^+$, $Bi_3{}^+$), will result in much greater secondary ion yields for high molecular components – especially in the range of 500–5,000 Da. For instance, the use of an atomic cluster such as $C_{60}{}^+$ results in a significant number of surface atoms being sputtered from the surface, relative to a smaller beam such as Ga^+ (Figure 7.44). For a 15 keV incident beam, each carbon atom would contain 15,000/60 eV (*i.e.*, 24, 000 kJ mol^{-1}–50 times greater than the C-C bond strength in C_{60}!). Hence, the atomic cluster likely behaves as 60 individual 250 eV atoms with a much broader impact on the surface. However, since the kinetic energy of each C_{60} cluster is much

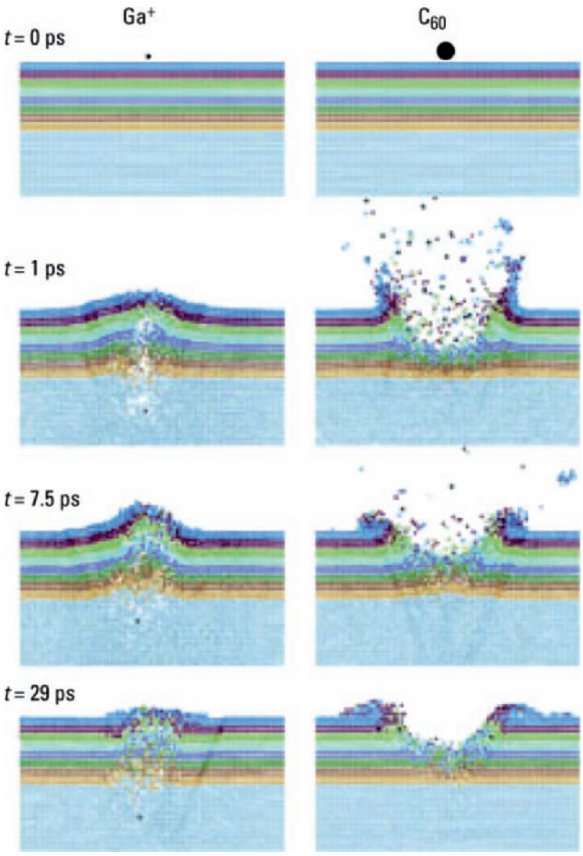

Figure 7.44. Molecular dynamics simulation of the ion bombardment of a Ag crystal surface with a 15 keV Ga^+ beam, and a 15 keV C_{60} atomic cluster beam. The C_{60} beam results in a larger crater and more material removed from the surface. In contrast, the Ga^+ beam results in a destructive effect at greater sample depths, without successful sputtering of the sample. Reproduced with permission from Winograd, N. *Anal. Chem.* **2005**, *77*, 142A. Copyright 2005 American Chemical Society.

less than a Ga^+ ion (15 keV), the sputtering event for ${C_{60}}^+$ is limited to the first few monolayers of the sample.[88]

Another strategy that is used to increase the TOF-SIMS signal for polymeric samples is the application of a metallic coating[89] or nanoparticles[90] onto the sample surface (Figure 7.45). The signal enhancement is likely a result of facilitated electron loss (Eq. 12), as well as the formation of conjugate ions that contain the neutral polymer fragment and metal atoms (Eqs. 13 and 14). The reaction between the polymer fragment and a proton, either in the gas-phase or at the metallic surface, may also result in signal enhancement (Eq. 15).[90]

(12) $\quad M \rightarrow [M]^+ + e^-$

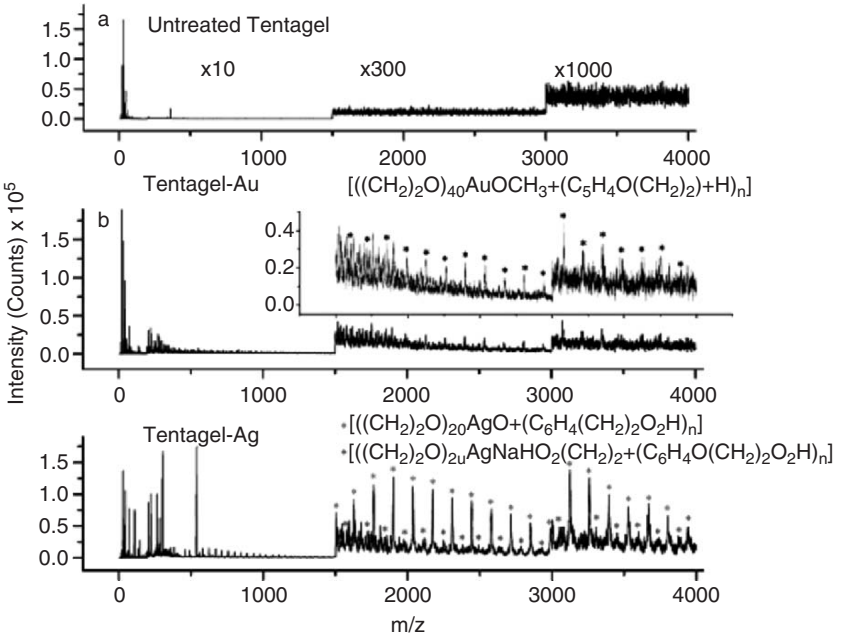

Figure 7.45. SIMS signal enhancement from metal nanoparticle deposition. Shown are comparative spectra in the high molecular weight range for an untreated polymer (a), along with nanoparticle-treated samples (b, c). Reproduced with permission from Marcus, A.; Winograd, N. *Anal. Chem.* **2006**, *78*, 141. Copyright 2006 American Chemical Society.

$$(13) \quad [M + Me]^+ \rightarrow [M]^+ + Me^0$$

$$(14) \quad M + [Me]^+ \rightarrow [M + Me]^+$$

$$(15) \quad M + H^+ \rightarrow [M + H]^+$$

where M is the neutral polymer fragment; Me, neutral metal atom (present as a film or nanoparticles).

In addition to secondary ion generation, SIMS also results in the release of secondary electrons near the sample surface. As previously discussed for SEM analysis, this may result in the buildup of a net electric current for nonconductive surfaces. Analogous to microscopy applications, such surface charging will diffuse the primary beam, making it difficult to perform microanalysis using SIMS. Furthermore, charging will deleteriously affect the detection of secondary ions, by altering the energy distribution of the recoiled ions. These effects are magnified when a sample contains a dielectric surface and a conductive substrate. Due to the strong induced electric field, mobile metal ions in the substrate may migrate toward the surface. Consequently, the data obtained from depth profiling will no longer reflect the original composition of the sample layers. Since information is gleamed from the uppermost portion of the sample, the application of a simple conductive coating is not

feasible for SIMS. Rather, the effects of charging may be minimized by the following techniques:

(i) *Electron bombardment* – typically used in quadrupole (dynamic) SIMS instruments. A low electron beam is used to compensate for a positive charge buildup.
(ii) *Surface conducting grid* – a metallic grid is placed over the sample. When the primary beam impinges this surface, the grid releases secondary electrons that dissipate the buildup of positive charge. Alternatively, a gold or carbon coating may be sputtered onto the sample surface, and then removed from the area to be analyzed – leaving a conductive film that encapsulates the area of interest.
(iii) *Use of negative primary ion beams* – for example, oxygen.

Another widely used application for SIMS is *ion imaging*, which shows secondary ion intensities as a function of spatial location on the sample surface (Figure 7.46). Further, if imaging is performed in tandem with depth profiling, a three-dimensional compositional map of a sample may also be generated (Figure 7.46). Two modes of imaging *via* SIMS are possible:

(i) *Ion microscopy* – the sample is uniformly irradiated and the image is formed directly on a viewing screen *via* optics similar to SEM (max. lateral resolution of *ca.* 0.5 μm).
(ii) *Ion microprobe* – the ion beam is rastered across the surface (max. lateral resolution of *ca.* 20 nm, using liquid metal ion guns).

7.4. SCANNING PROBE MICROSCOPY

The characterization techniques discussed thus far have involved the interaction of an incident beam of radiation (electrons, X-rays, ions, or light) with a sample. Subsequent scattering, transmission, and/or secondary emission is then used to provide an image of the sample, or delineate its chemical composition. This section will discuss a technique that does not involve irradiation, but rather features the scanning of a probe across a surface (hence, termed SPM). A tangible analogy of this technique is actually the precursor to modern CD players – the phonograph/record player (check your local antique shop if you have not seen one before!). The heart of an antiquated phonograph is a cantilever-supported stylus that followed the grooves on the record. The mechanical movement of the stylus within the grooves resulted in an electrical response from a piezoelectric crystal, which was then converted into sound *via* the speaker system. Though this technology was abandoned for stereo applications in the 1980s, SPM represents a next-generation application for a stylus with a much sharper tip (radius of curvature of <50 nm), to follow the surface topography of microscale and nanoscale materials. The resolution of SPM is among the best of all methods to date, with the possibility of atomic scale manipulation/imaging (revisit Figure 6.3 in Chapter 6 – the manipulation and imaging of individual Xe atoms – performed almost 20 years ago!).

Analogous to record players, a SPM tip is supported by a flexible cantilever. During analysis, the tip is slowly rastered across the surface of a material – either

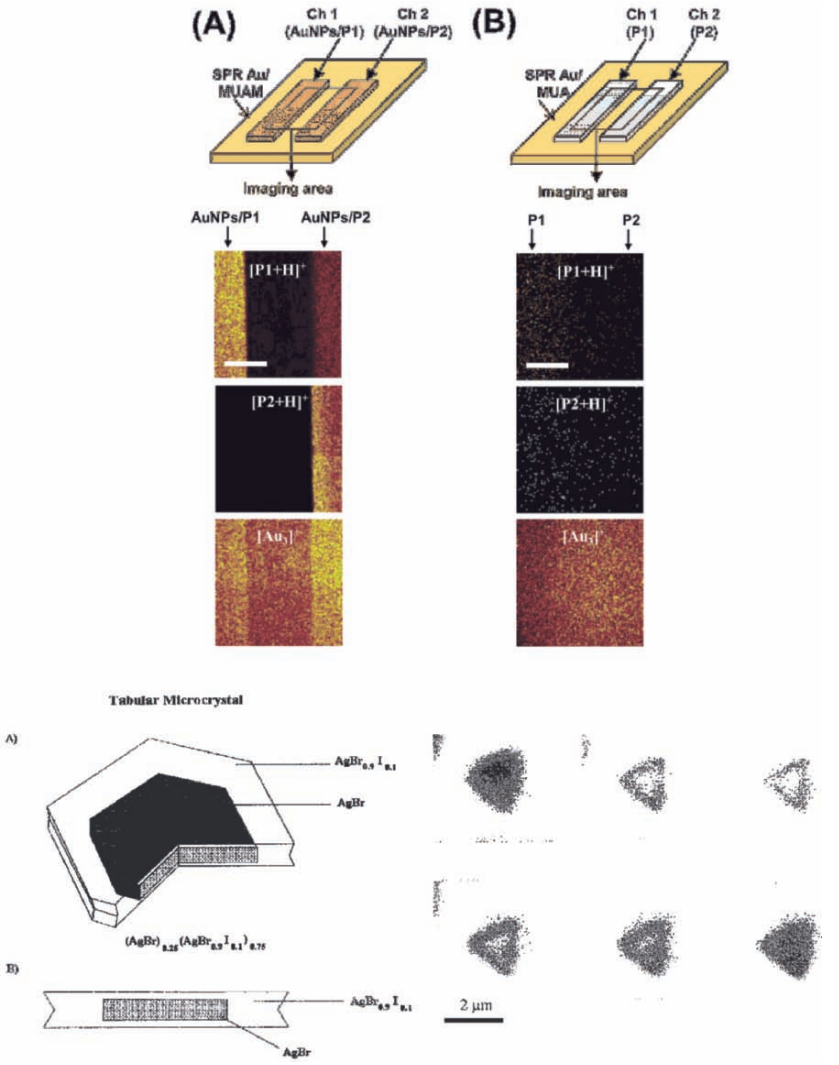

Figure 7.46. Ion imaging using SIMS. (Top) Positive TOF-SIMS images of fragments from peptides (P1, Ac-PRNYVTP-NH_2; P2, Ac-PRNYpVTP-NH_2) patterned on SAMs, pretreated (A) with gold nanoparticles and (B) without gold nanoparticles. The lateral region at both sides (both arrows) represents a microfluidic pattern of different peptides (P1 and P2). TOF-SIMS utilized a Au^+ primary ion gun, with an ion dose $<10^{13}$ ions cm^{-2} at a sample area of $300 \times 300\,\mu m^2$. The scale bar is 100 µm.[91] (Bottom) Schematic of a silver halide microcrystal with a core-shell structure. The diameter is *ca.* 0.5–2 µm; the thickness is *ca.* 150–400 nm. To the right of the illustration are successive I^- ion images (using a Cs^+ primary beam) for the crystal, shown from the top left corner to the bottom right corner, as a function of depth profiling. Whereas the first and last images show a homogeneous iodine-rich array, the middle images show the I^- distribution localized in the shell of the microcrystal.[92]

a few Angstroms away from the surface (noncontact mode), or in contact with the sample (contact mode). There are two primary forms of SPM[93]:

(i) *Scanning tunneling microscopy* (STM) – set the precedent for SPM in the early 1980s. The tip is held a few Angstroms from the sample surface during scans.
(ii) *Atomic force microscopy* (AFM) – the tip may interact with the sample surface through either contact or noncontact modes.

Both types of SPM are most often used to provide an image of the surface topography. Though both techniques are frequently carried out under ambient temperatures/pressures, or even in liquids,[94] they may also be performed in an UHV chamber (*ca.* 10^{-11} Torr)[95] in order to prevent sample contamination, prevent oxidation of the surface, or monitor the deposition of sputtered thin films in real time. As a STM tip is scanned across the sample, a quantum mechanical tunneling current is established between the sample surface and a sharpened W or Pt/Ir tip (Figure 7.47, top). The magnitude of the current is dependent on the distance between the tip and the surface (Δz), as well as the local DOS of the surface. Accordingly, STM is typically performed on conductive and semiconductive surfaces. During topographic imaging, a feedback loop is established to maintain a constant current through varying the distance between the tip and surface ("constant current mode"). In this respect, STM is able to provide real-time, three-dimensional images of the surface with atomic resolution. The use of STM for nanofabrication also represents an important application that is of increasing interest.[96]

In addition to imaging applications, *scanning tunneling spectroscopy* (STS) may be performed, which delineates the local electronic structure of a surface. In this mode, the feedback loop is interrupted, which fixes the distance between tip and sample. A current *vs.* voltage (I–V) curve may then be acquired at a specific (x,y) position on the surface by ramping the bias voltage, and recording the tunneling current. If the I–V curves are collected at every point, a three-dimensional map of the electronic structure may be generated.[97]

Rather than monitoring electronic tunneling phenomena, AFM measures the forces between the tip and surface, which depends on the nature of the sample, the probe tip, and the distance between them (Figure 7.47, bottom).[98] The deflection of the tip in response to surface–tip interfacial forces is recorded by using a laser focused on top of the Si or SiN cantilever, and reflected onto photodetectors. The signal emanating from the photodetector is used to generate a surface topographic map, or the direct measurement of surface intermolecular forces. As with STM, a feedback loop is present in the system, which controls the distance between the tip and sample *via* an electrical current sent to piezoelectric transducers. Such "constant force" scanning is used most frequently, since "constant-height" scanning could result in collisional damage between the tip and surface.

The most common operating modes of AFM are contact, noncontact, and tapping, which are self-explanatory in their manner of interrogation of the surface. In contact-mode AFM, there is a repulsive force between the sample and tip (*ca.* 10^{-9} N); the piezoelectric response of the cantilever either raises or lowers the tip to maintain a constant force. Similarly as STM, the best resolution will be obtained under UHV conditions. That is, in an ambient environment, adsorbed

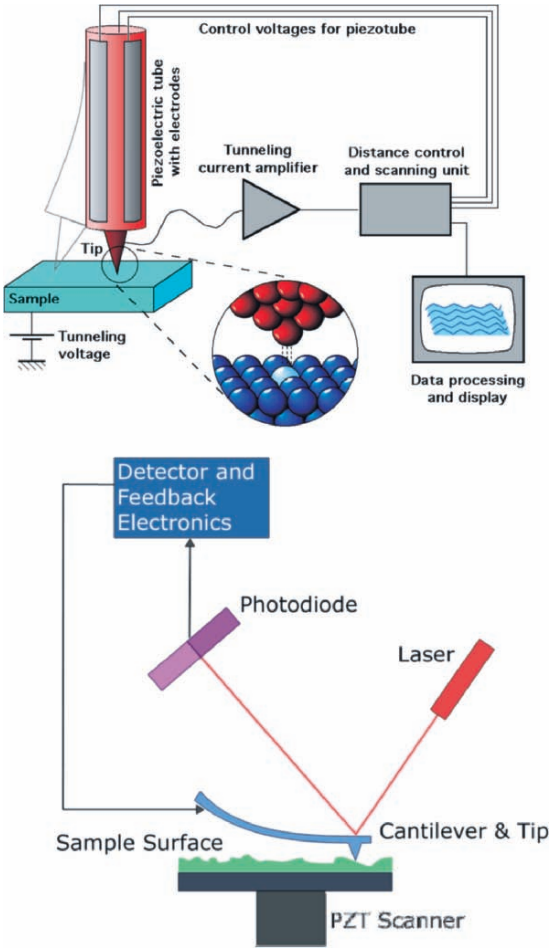

Figure 7.47. Illustrations of STM (top), and AFM (bottom). Reproduced with permission through the Wikipedia Commons agreement. The illustration of STM is courtesy of Michael Schmid, TU Wien, and is available online at: http://www.iap.tuwien.ac.at/www/surface/STM_Gallery/stm_schematic.html. The illustration of AFM is available online at: http://en.wikipedia.org/wiki/Image:Atomic_force_microscope_block_diagram.png

vapors (*e.g.*, N_2, H_2O) form a layer on the surface with a thickness of *ca.* 10–30 monolayers. Consequently, a meniscus will form between the tip and surface, which results in the attraction of the tip toward the surface due to surface tension forces. This force may be neutralized by operating the AFM in a liquid cell, in which the tip is completely immersed in a solvent (Figure 7.48). It should be noted that frictional forces are not always detrimental; lateral force AFM, or the purposeful dragging of the tip along the surface, is useful to determine spatial variations in the composition or phase of a surface.

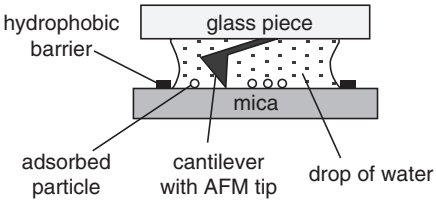

Figure 7.48. Illustration of an AFM system used for *in situ* studies within a liquid. Reproduced with permission from Gliemann, H.; Mei, Y.; Ballauff, M.; Schimmel, T. *Langmuir* **2006**, *22*, 7254. Copyright 2006 American Chemical Society.[100]

Noncontact AFM overcomes the frictional and adhesive forces between the tip and sample by hovering the tip a few Angstroms above the surface. In this mode, the attractive Van der Waal forces between the tip and surface are monitored. As you might expect, these attractive forces are much weaker than those generated in contact mode, often resulting in lower resolution. In order to improve the sensitivity of the tip, the cantilever is oscillated to better detect surface features through small variations in the oscillation wave characteristics (*i.e.*, phase, amplitude, *etc*.). It should be noted that noncontact AFM is often preferred over STM (also noncontact) to study "true" molecular assemblies on surfaces. That is, it has been shown that STM imaging may induce irreversible changes in molecular arrangements on surfaces, especially for high-resolution, constant-height imaging.[99]

During tapping AFM, the cantilever oscillation amplitude remains constant when not in contact with the surface. The tip is then carefully moved downward until it gently taps the surface. As the tip passes over an elevated surface feature, the cantilever has less room to oscillate, and the amplitude of oscillation decreases (*vice versa* for a surface depression). The oscillation frequency is typically 50–500 kHz, with an amplitude of *ca.* 30 nm, which is sufficient to overcome the adhesive forces that are evident in contact (and noncontact) modes (Figure 7.49). Consequently, the tapping mode is most appropriate for soft samples such as organics, biomaterials, *etc*.

Without question, AFM exhibits a much greater versatility for surface analysis than STM. In particular, the following variations are possible, through altering the nature of the tip:

(i) *Chemical force microscopy* (CFM) – uses a chemically modified tip to examine interfacial behavior between the sample and functional groups on the tip surface.[101]

(ii) *Magnetic force microscopy* (MFM) – uses a noncontact magnetic-susceptible tip to map the magnetic properties of a surface, with spatial resolutions of $<$20 nm.[102]

(iii) *Scanning thermal microscopy* (SThM) – uses a resistive Wollaston wire instead of a conventional AFM probe, which acts as a localized heating source and microthermocouple, used to map the thermal conductivity of a surface.[103]

(iv) *Scanning electrochemical microscopy* (SECM) – based on the electrochemical interaction between a redox-active species produced at the tip, and the substrate

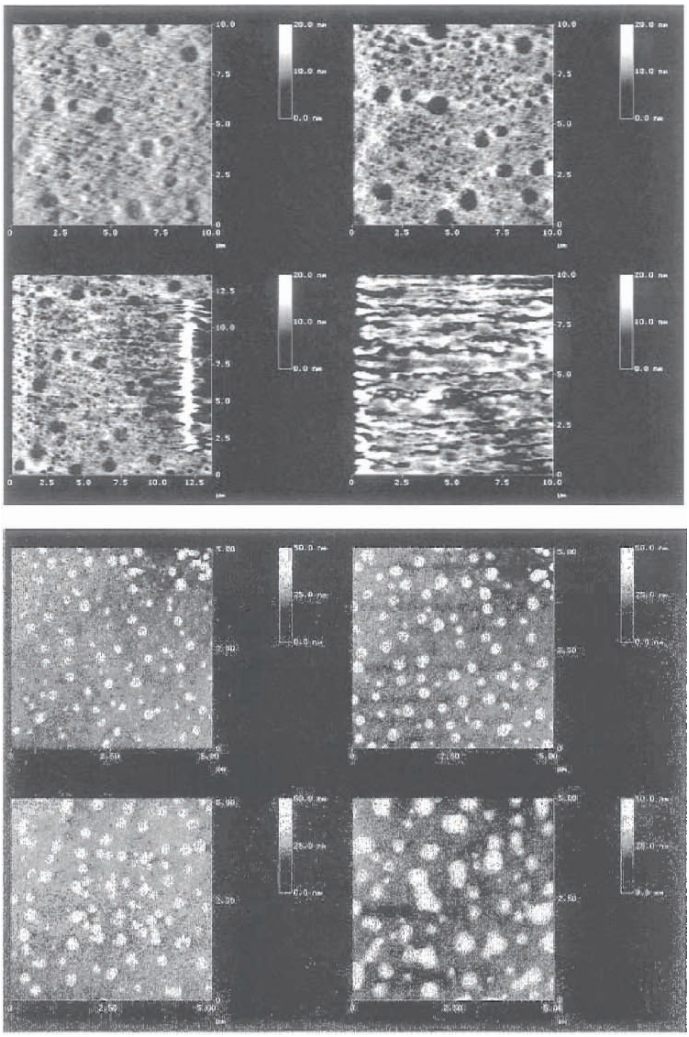

Figure 7.49. Comparative images of contact-mode (top) and tapping-mode (bottom) AFM under an ambient atmosphere. The images represent the surface of freshly cleaved potash–lime–silica glass after the elapsement of time intervals, from upper left to bottom right (top: 150, 264, 264 min (larger scan area), 8 h; bottom: 2, 5, 5 h (larger scan area), 43 h). Humidity-induced pit formation is only observable using contact mode (CM) – note the movement of surface corrosion products by the AFM tip (top, images c and d). In contrast, tapping-mode (TM) revealed round features that became visible after 2 h of exposure time. These surface features (observable only by TM) are likely swelled glass material due to the breakdown of the silicate network through water adsorption and subsequent surface ion-exchange reactions. Contact-mode AFM is not able to image these surface features, since the tip scrapes away the silicate residue during analysis. Reproduced with permission from Schmitz, I.; Schreiner, M.; Friedbacher, G.; Grasserbauer, M. *Anal. Chem.* **1997**, *69*, 1012. Copyright 1997 American Chemical Society.

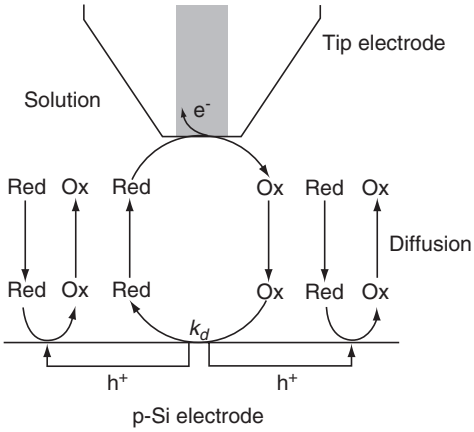

Figure 7.50. Illustration of scanning electrochemical microscopy (SECM). Reproduced with permission from Ghilane, J.; Hauquier, F.; Fabre, B.; Hapiot, P. *Anal. Chem.* **2006**, *78*, 6019. Copyright 2006 American Chemical Society.

being studied (Figure 7.50). Hence, this method offers high chemical selectivity, and is able to correlate localized surface features with their chemical reactivities. [104]

In order to carry out the above applications (as well as standard imaging/force measurements), AFM tips may be selected from among a wide variety of sizes and shapes.[105] A recent discovery that will greatly assist in the characterization of nanomaterials is the fabrication of tips that are terminated with individual gold nanoparticles or single-walled carbon nanotubes (Figure 7.51).[106] These advanced designs will offer significant improvements in resolution (and artifact generation) over conventional tips.[107] Furthermore, analogous tip designs will allow one to probe the physical, thermal, magnetic, and optical properties of individual nanoarchitectures *via* SPM.

7.5. BULK CHARACTERIZATION TECHNIQUES

The majority of characterization techniques discussed thus far have been surface-related, with some capable of analyzing sub-surface depths through *in situ* ion etching. This final section will focus briefly on a selection of common bulk techniques that may be used to characterize as-synthesized materials such as polymers, ceramics, *etc*. More details on these and other techniques not discussed herein may be found in the "Further Reading" section at the end of this chapter. In particular, these additional resources, as well as countless others online, will highlight solid-state characterization techniques such as:

(i) *Solid-state NMR* – chemical environment of NMR-active nuclei; used to obtain physical, chemical, electronic, and structural information about constituent molecules.

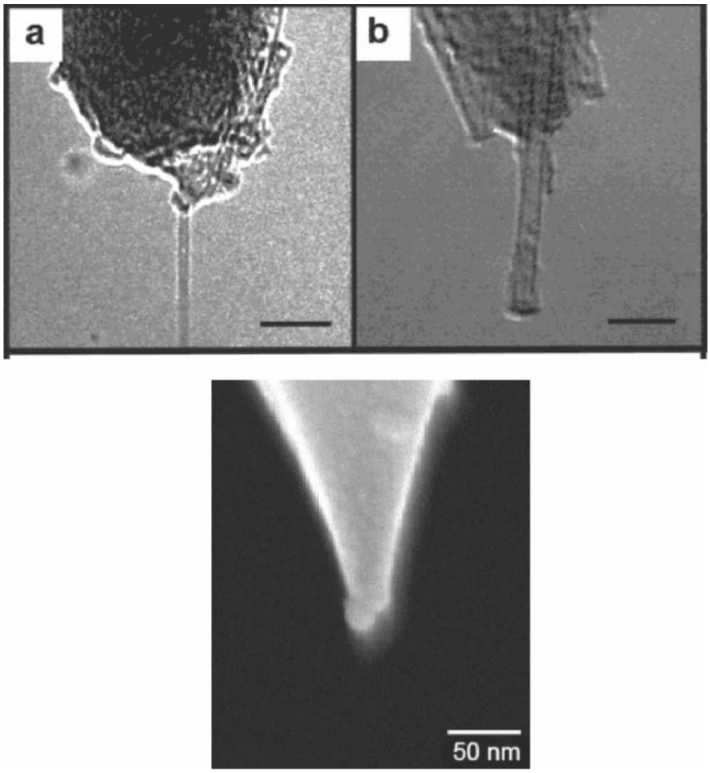

Figure 7.51. Advanced AFM tip designs. Shown (top) are SWNT-terminated AFM tips (scale bars are 10 nm)[106]b and (bottom) an AFM tip terminated with an individual gold nanoparticle (diameter of 14 nm).[106]a

(ii) *Raman spectroscopy* – vibration, stretching, and bending of sample molecules (for the bulk sample, as well as adsorbed surface species); assessing defects in carbon nanotubes.
(iii) *IR spectroscopy* (including surface-characterization modes such as attenuated total reflectance (ATR), diffuse reflectance infrared Fourier transform spectroscopy (DRIFT), and reflection absorption infrared spectroscopy (RAIRS)) – complementary to Raman spectroscopy.
(iv) *UV–Vis spectroscopy* – functional group information; sizes of nanoparticles.
(v) *Mass spectrometry* (MS) – information regarding isotopes, mass, and structure.
(vi) *BET*[108] *surface area analysis* – pore size and surface area of powders.
(vii) *Dynamic light scattering* (DLS) and Coulter counting – particle size.
(viii) *Mössbauer spectroscopy* – chemical environment of ^{57}Fe, ^{129}I, ^{119}Sn, or ^{121}Sb atoms in a sample.
(ix) *Single-crystal and powder X-ray diffraction* – three-dimensional arrangement of atoms/ions/molecules.
(x) Physical testing techniques (tensile strength, flame retardancy, *etc.*).

A primary method that is used to characterize the thermal properties of a bulk material is *thermogravimetric analysis* (TGA). This method provides detailed information regarding the thermal stability and decomposition pathway of a material (*e.g.*, stepwise loss of ligands for an organometallic compound), as well as structural information for complex composites (Figure 7.52). The operating principle of TGA is

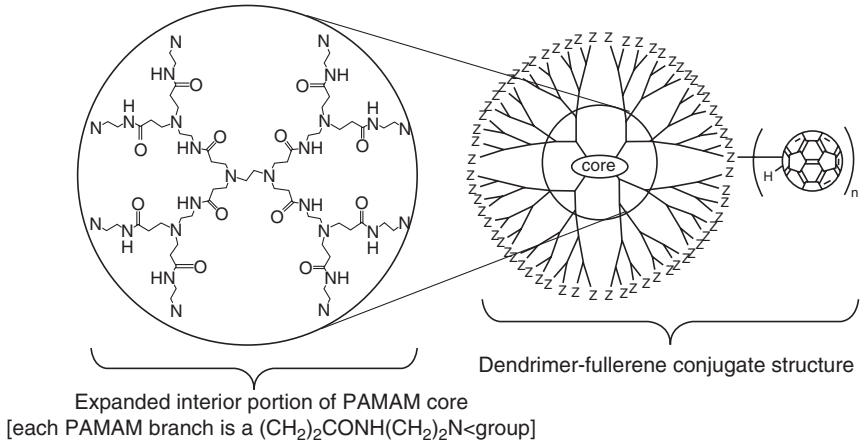

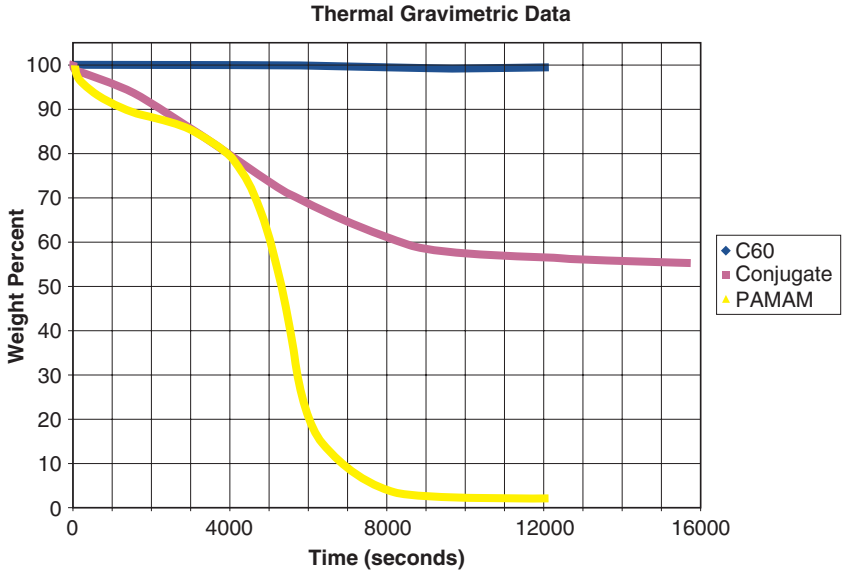

Figure 7.52. Schematic of a PAMAM dendrimer–fullerene conjugate structure (top), with TGA analysis (bottom). Based on the mass loss of the conjugate, it is suggested that each PAMAM dendrimer is surrounded by 30 fullerene units. Reproduced with permission from Jensen, A. W.; Maru, B. S.; Zhang, X.; Mohanty, D. K.; Fahlman, B. D.; Swanson, D. R.; Tomalia, D. A. *Nano Lett.* **2005**, 5, 1171. Copyright 2005 American Chemical Society.

very simple – the solid is placed in a tiny microbalance pan and heated according to preset ramping conditions. The controlled thermolysis of the compound may be carried out *in vacuo*, or in the presence of a carrier gas such as O_2, N_2, or Ar.

In addition to performing simple mass-loss investigations, TGA may also be applied to accurately determine the enthalpy of sublimation (ΔH_{sub}), as well as the sublimation temperature (T_{sub}) of a solid.[109] In these investigations, the mass loss through sublimation (m_{sub}) will be constant at a given temperature, as long as the phase change occurs without appreciable decomposition. Hence, by measuring the mass loss over a variety of isothermal regions, a plot of $\log(m_{sub}T^{1/2})$ *vs.* $1/T$ may be generated, which readily yields values of ΔH_{sub} and T_{sub} from the slope and *y*-intercept, respectively (Eq. 16):

$$\log\left(m_{sub}\sqrt{T}\right) = \frac{-0.0522(\Delta H_{sub})}{T} + \left[\frac{0.0522(\Delta H_{sub})}{T_{sub}} - \frac{1}{2}\log\left(\frac{1,306}{M_w}\right)\right]. \quad (16)$$

A technique that is often used in tandem with TGA[110] is *differential scanning calorimetry* (DSC).[111] This technique monitors the amount of heat that is required to increase the temperature of a sample, relative to a reference. For example, when a sample undergoes an endothermic phase transition (*e.g.*, melting), heat will be absorbed; conversely, an exothermic event (*e.g.*, crystallization) will require less heat to raise the temperature. Accordingly, DSC is used to determine distinct thermodynamic events, as well as subtle changes such as glass transitions that occur during polymer curing (Figure 7.53).

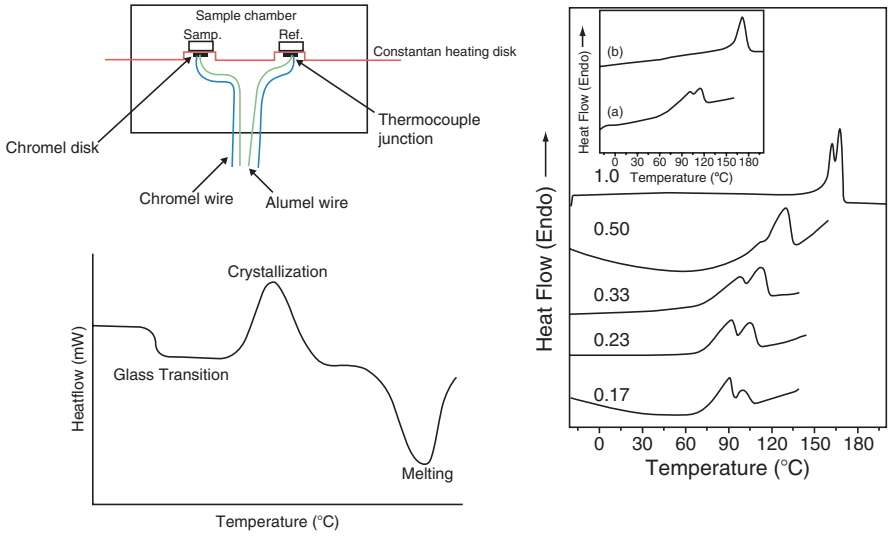

Figure 7.53. Differential scanning calorimetry (DSC). Shown are (a) schematic of the heat-flux sample chamber; (b) an example of a DSC thermogram, showing endothermic events[113]; (c) DSC thermogram of a poly(vinylidene fluoride)–ethyl acetoacetate polymer–solvent system, showing two melting events for the polymer due to its intermolecular interactions with solvent molecules. The inset shows a comparison between the pure polymer (b) and the polymer-solvent (a). Reproduced with permission from Dasgupta, D.; Malik, S.; Thierry, A.; Guenet, J. M.; Nandi, A. K. *Macromolecules* **2006**, *39*, 6110.

The viscoelastic properties of a polymer (high modulus, "glass-like," or low modulus, "rubber-like") may be determined through *dynamic mechanical (thermal) analysis* (DMA or DMTA). This technique involves monitoring the resultant displacement of a polymer following its interaction with an oscillating external force, as the temperature is altered. In addition to readily observing the glass transition, other properties such as stiffness and damping properties are generated from this technique.

Though TGA/DSC and DMA are extremely useful for polymer characterization, these techniques provide no (direct) structural information. As an alternative, structural information such as conformational changes of noncrystalline macromolecules may be determined by *small-angle scattering* (SAS) techniques.[112] This method examines the patterns arising from the elastic scattering of X-rays (SAXS) or neutrons (SANS) from sample components. Whereas SAXS provides information regarding the electron density distribution of the sample, SANS is sensitive toward the sample nuclei. For instance, ^{1}H and ^{2}H (deuterium) exhibit different scattering lengths; hence, many studies perform isotopic labeling to gain additional structural information about the sample.[114] The larger the scattering angle, the smaller the length scale that may be probed; hence, wide-angle X-ray scattering (WAXS) is used to determine structural information on the atomic length scale, and SAXS/SANS are used in the size regime of *ca.* 1–300 nm (Figure 7.54). A wide variety of samples may be analyzed by SAS, most often consisting of powders or solvent suspensions of macromolecules or nanoparticles/colloids.[115]

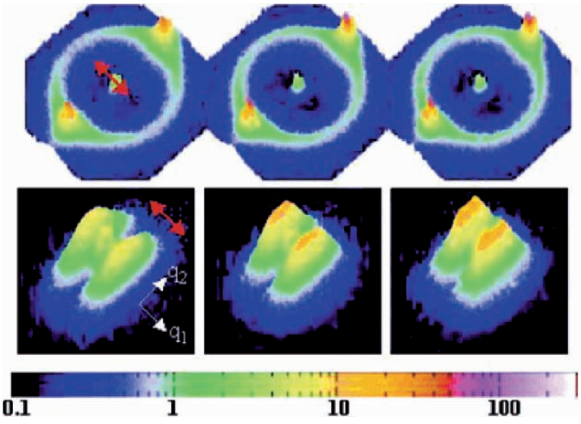

Figure 7.54. Wide-angle (top) and small-angle (bottom) X-ray scattering patterns of drawn polyethylene fibers, annealed for 264 h at 23, 80, and 100°C (from left to right). The red arrows indicate the drawing direction. The peaks in the WAXS pattern remain unchanged during annealing, whereas the pattern changes significantly for SAXS. This is proposed to indicate the preferential orientation of the polymeric chains along the drawing direction, whereas the lamella in the samples exhibit slight shear during annealing. Reproduced with permission from Men, Y.; Rieger, J.; Lindner, P.; Enderle, H. -F.; Lilge, D.; Kristen, M. O.; Mihan, S.; Jiang, S. *J. Phys. Chem. B* **2005**, *109*, 16650. Copyright 2005 American Chemical Society.

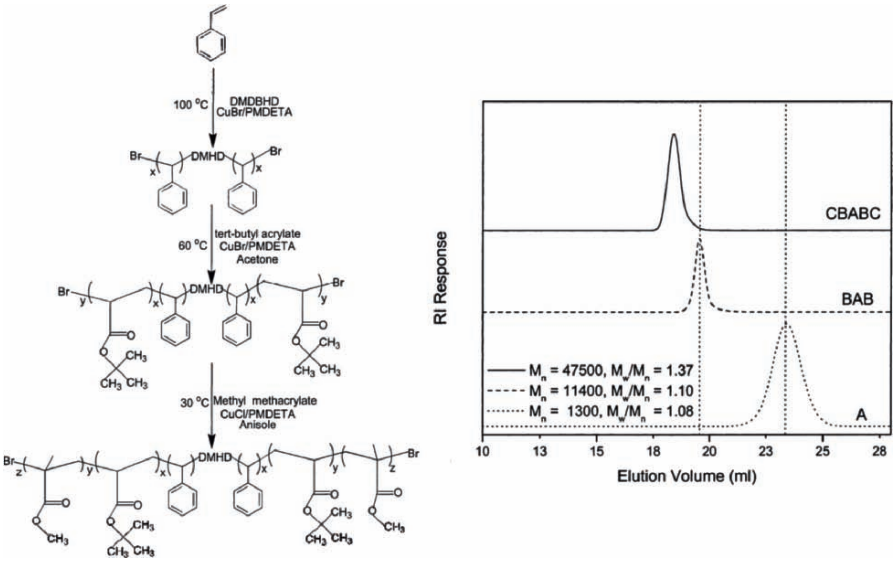

Figure 7.55. Reaction scheme for the room-temperature synthesis of a CBABC pentablock copolymer, and GPC traces of *a*,*z*-dibromo-terminated polystyrene (A, dotted line), poly(*t*BA-*b*-styrene-*b*-*t*BA) (BAB triblock copolymer macroinitiator, dashed line), and poly(MMA-*b*-*t*BA-*b*-styrene-*b*-*t*BA-*b*-MMA) (CBABC, solid line). The GPC data shows evidence of a successful polymerization route – low polydispersity index (PDI), and good control over the number-average molecular weight (M_n). Reproduced with permission from Ramakrishnan, A.; Dhamodharan, R. *Macromolecules* **2003**, 36, 1039. Copyright 2003 American Chemical Society.

An additional method that is used to characterize polymers is *gel-permeation chromatography* (GPC). This technique is a form of *size-exclusion chromatography* (SEC), where components are separated from one another based solely on their sizes (or hydrodynamic volume). GPC is carried out in the same configuration as other HPLC (high-performance liquid chromatography) methods, with a gel stationary phase and a pressurized liquid mobile phase that elutes the dissolved components from the column. Separation occurs as the solution is passed through the gel, which comprises polystyrene crosslinked with divinylbenzene. While the larger molecules pass through the column without significant retention, the smaller molecules are retained by encapsulation within the pores of the gel (*ca.* pore diameters of 100–10^6 nm). The information obtained from gel-permeation chromatographs is mostly used to determine the molecular weight distribution of a polymer, known as the polydispersity index (PDI, Figure 7.55).

IMPORTANT MATERIALS APPLICATIONS VI: SO WHICH ACRONYM SHALL I CHOOSE?!

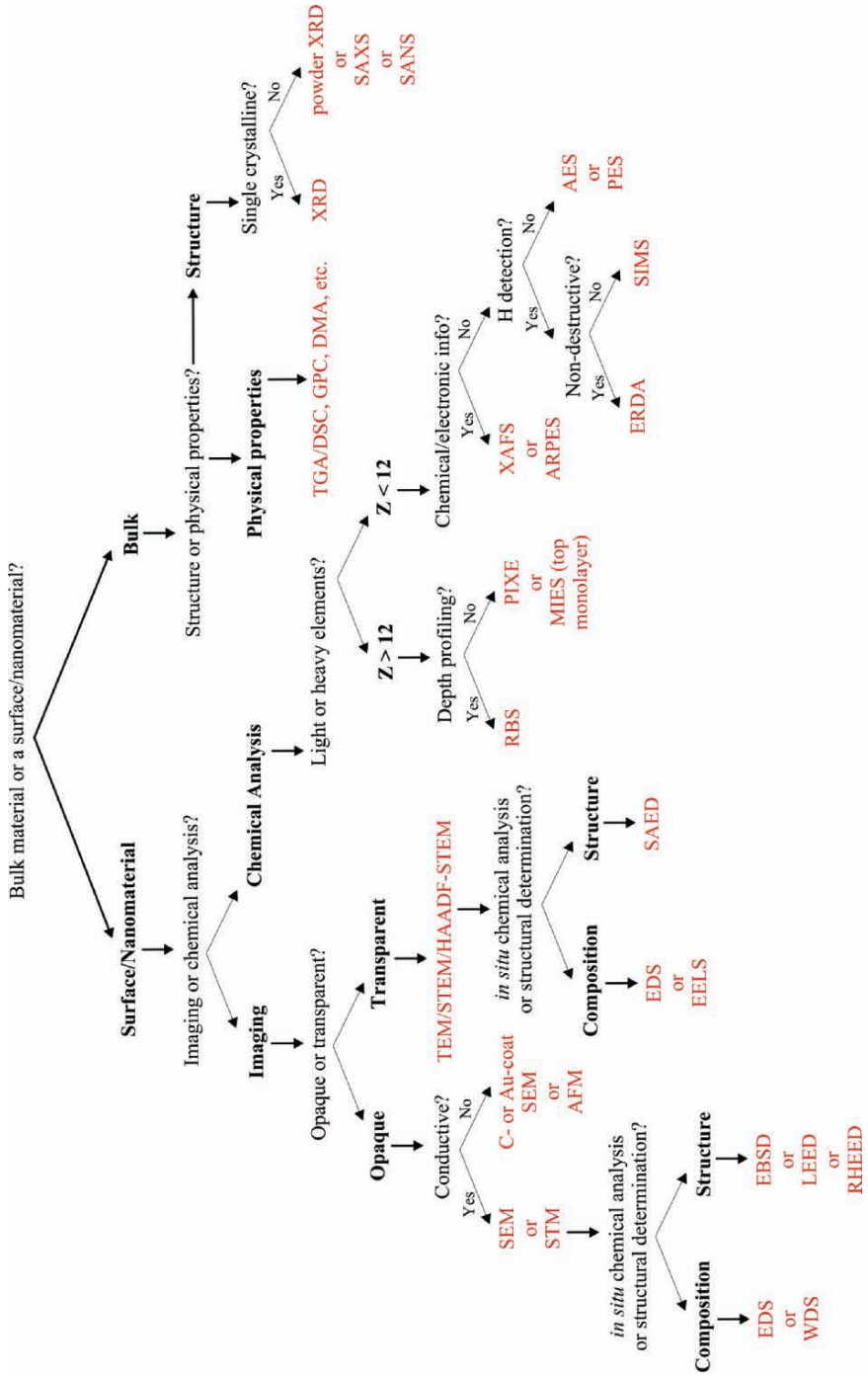

References and Notes

1 More information on the components and operation of reflection microscopes may be obtained from http://www.microscopyu.com/articles/dic/reflecteddic.html

2 Synge, E. H. *Philos. Mag.* **1928**, 6, 356.

3 For a thorough review of NSOM, see: Dunn, R. C. *Chem. Rev.* **1999**, *99*, 2891.

4 Mass of a Golf Ball: http://hypertextbook.com/facts/1999/ImranArif.shtml

5 It is important to note the general trend of decreasing wavelength (and greater resolution) as the velocity of electrons is increased (*i.e.*, higher accelerating voltages).

6 Cremer, J. T.; Piestrup, M. A.; Gary, C. K.; Pantell, R. H.; Glinka, C. J. *Appl. Phys. Lett.* **2004**, *85*, 494.

7 For example, see: http://accelconf.web.cern.ch/AccelConf/p05/PAPERS/WOAC001.PDF

8 O'Dwyer, C.; Navas, D.; Lavayen, V.; Benavente, E.; Santa Ana, M. A.; Gonzalez, G.; Newcomb, S. B.; Sotomayor Torres, C. M. *Chem. Mater.* **2006**, *18*, 3016.

9 Hu, J.; Bando, Y.; Zhan, J.; Zhi, C.; Golberg, D. *Nano Lett.* **2006**, 6, 1136.

10 For an image of the lattice structure and properties of LaB_6, see: http://www.kimphys.com/cathode/catalog_PDF/LaB6_cathode_ES423.pdf

11 Perkins, C. L.; Trenary, M.; Tanaka, T.; Otani, S. *Surface Sci.* **1999**, *423*, L222. Accessed online at: http://www.chem.uic.edu/mtrenary/LaB6.pdf

12 http://www.physics.uc.edu/∼jarrell/COURSES/ELECTRODYNAMICS/Student_Projects/tharanga/review.pdf

13 (a) http://anl.gov/techtransfer/Available_Technologies/Chemistry/uncd_flc.html (b) Krauss, A. R.; Auciello, O.; Ding, M. Q.; Gruen, D. M.; Huang, Y.; Zhimov, V. V.; Givargizov, E. I.; Breskin, A.; Chechen, R.; Shefer, E.; Konov, V.; Pimenov, S.; Karabutov, A.; Rakhimov, A.; Suetin, N. *J. Appl. Phys.* **2001**, *89*, 2958, and references therein.

14 Unless otherwise stated, TEM micrographs are collected as bright-field images.

15 The low-resolution SEM image was reproduced with permission from Li, F.; Zhang, L.; Metzger, R. M. *Chem. Mater.* **1998**, 10, 2470. Copyright 1998 American Chemical Society.

16 The high-resolution SEM image was reproduced with permission from Moon, J. -M.; Wei, A. *J. Phys. Chem. B* **2005**, *109*, 23336. Copyright 2005 American Chemical Society.

17 http://www.microstartech.com/index/cryo.htm

18 The FIB/lift-out technique yields cross sections of both the film and substrate, which maintains the integrity of the interface; in comparison, ultramicrotomy requires the removal of the polymer film and subsequent embedding/sectioning. For a detailed example, see: White, H.; Pu, Y.; Rafailovich, M.; Sokolov, J.; King, A. H.; Giannuzzi, L. A.; Urbanik-Shannon, C.; Kempshall, B. W.; Eisenberg, A.; Schwarz, S. A.; Strzhemechny, Y. M. *Polymer* **2001**, *42*, 1613.

19 Reproduced with permission from Fu, L.; Liu, Y.; Hu, P.; Xiao, K.; Yu, G.; Zhu, D. *Chem. Mater.* **2003**, *15*, 4287. Copyright 2003 American Chemical Society.

20 Reproduced with permission from Liu, Z.; Ohsuna, T.; Sato, K.; Mizuno, T.; Kyotani, T.; Nakane, T.; Terasaki, O. *Chem. Mater.* **2006**, *18*, 922. Copyright 2006 American Chemical Society.

21 Virgilio, N.; Favis, B. D.; Pepin, M. -F.; Desjardins, P. *Macromolecules* **2005**, *38*, 2368.

22 Another way to state this is that for a single crystal, only a few lattice planes will be oriented at their Bragg angle at any one time.

23 An excellent book that contains many high-resolution TEM images and the electron diffraction patterns for a variety of archetypical unit cells see: Sindo, D.; Hiraga, K. *High-Resolution Electron Microscopy for Materials Science*, Springer: New York, 1998.

24 Reproduced with permission from Sun, G.; Sun, L.; Wen, H.; Jia, Z.; Huang, K.; Hu, C. *J. Phys. Chem. B* **2006**, *110*, 13375. Copyright 2006 American Chemical Society.

25 Reproduced with permission from Liu, Y.; Xu, H.; Qian, Y. *Cryst. Growth Design* **2006**, 6, 1304. Copyright 2006 American Chemical Society.

26 An excellent summary of crystallography and systematic absences is given by: http://169.232.130.50/khan/KhanWebClass.ASP?WCI=Nutshell#LAUE%20SYMMETRY%20ANDk%20SYSTEMATIC%20ABSENCES.

[27] The nomenclature for X-ray emission consists of the name of the shell in which the vacancy was created (K, L, M, N), and on the electronic shell that filled the vacancy. For instance, ejection of a K shell electron, filled with a L shell electron is denoted as K_α; if filled with an M shell electron, then K_β is used, and so on. Due to electronic subshells, nomenclature becomes significantly complex, as shown in Figure 7.19.

[28] It should be noted that EDS and WDS are often referred to as EDX and WDX, or XEDS and XWDS, respectively.

[29] The detection limits for EDS are typically 0.1 at% (for elements with $Z > 10$), whereas WDS is able to detect elements present in concentrations of a few ppm.

[30] Electromagnetic lenses suffer from three types of defects: astigmatism, spherical aberrations, and chromic aberrations. Astigmatism may be easily minimized by placing electromagnets, known as stigmator coils, around the column. The current in these coils may be varied, which will reform the distorted electron beam back into a round shape. Chromic aberrations may be reduced by using a field emission source that produces an electron beam with a sharper distribution of electron energies. However, the third type of defect, spherical aberrations (C_s), are not easily circumvented. In fact, this is the primary factor that limits the resolution of electron microscopes to values far below their theoretical values. Recently, techniques have been developed to correct for these defects, often involving the use of multipole lenses (*e.g.*, quadrupole, octapole, *etc*.) with careful control of their fabrication and operation. For a description of techniques used to design a Cs-corrected HRTEM, see: http://www.jeol.com/jeolnews/jeol_news_july2002/htm/02/index.htm

[31] The only atoms with diameters smaller than 1 Å are H and He!

[32] Fahlman, B. D., unpublished results.

[33] Reproduced with permission from Harmer, M. A.; Farneth, W. E.; Sun, Q. *J. Am. Chem. Soc.* **1996**, *118*, 7708. Copyright 1996 American Chemical Society.

[34] Reproduced with permission from Li, Y.; Xiang, J.; Qian, F.; Gradecak, S.; Wu, Y.; Yan, H.; Blom, D. A.; Lieber, C. M. *Nano Lett.* **2006**, 6, 1468. Copyright 2006 American Chemical Society.

[35] Some important precedents that show the utility of Z-contrast imaging: (a) Arslan, I.; Yates, T. J. V.; Browning, N. D.; Midgley, P. A. *Science* **2005**, *309*, 2195. (b) Chisholm, M. F.; Kumar, S.; Hazzledine, P. *Science* **2005**, *307*, 701. (c) Nellist, P. D.; Pennycook, S. J. *Science* **1996**, *274*, 413.

[36] For a recent study that shows the influence of focus, sample thickness, and inner detector angle on the image, see: http://www.jeol.com/jeol_news_july2002/pdf_light/22.pdf

[37] The photon energies for the light elements are: Be(0.109 keV), B(0.185 keV), C(0.282 keV), N(0.392 keV), O(0.523 keV), and F(0.677 keV). Due to these low energies, the emitted X-rays are easily absorbed by the sample or the components of the detector.

[38] Bremsstrahlung is from the German word *bremsen* ("to brake"), and *Strahlung* ("radiation") – thus, "braking radiation." This is characterized by a broad peak that results from deceleration of beam electrons due to scattering from atomic nuclei.

[39] Pronounced: $OH\text{-}zh\bar{a}$.

[40] The energy-dispersing device at the heart of EDS is a semiconducting diode. As an incoming X-ray photon impinges the diode, electron-hole pairs are generated, which yields a measurable electrical current. In order to reduce background noise from photons not originating from the sample, the detector is operated at temperatures of *ca.* 140 K. A protective window comprising Be, or more recently, ultrathin windows of BN, diamond, or a supported polymer (paralene, norvar), is used to prevent the condensation of vapors (*e.g.*, water, organics) onto the cooled diode. A "windowless" detector may also be used for EDS; with careful operation, this modification allows the detection of elements down as far as Be – with a maximum efficiency of only 2%. It should be noted that although UHV conditions are used in a TEM/SEM instrument, there will always be a low concentration of vapors – often originating from the rotary pump fluid, or the sample itself due to beam-induced volatilization/decomposition, residual solvent evaporation, *etc*. The buildup of such a coating on the detector window will reduce the energy of the incoming X-rays, which will drastically reduce the detection sensitivity – especially for low-Z elements.

[41] It should be noted that reflection techniques are also possible through modifying the angle of approach of the incident electron beam of the TEM. Such analysis is referred to as reflection electron microscopy (REM), and accompanying characterizations such as *reflection high-energy electron diffraction* (RHEED) and *reflection electron energy-loss spectroscopy* (REELS)

are also possible, grouped under the umbrella of reflection high-resolution analytical electron microscopy (RHRAEM). (a) For an application of this multifaceted approach to study GaAs(110) surfaces, see: Wang, Z. L. *J. Electron. Microsc. Tech.* **1988**, *10*, 35 (citation found online at: http://www.osti.gov/energycitations/product.biblio.jsp?osti_id=6614173). (b) Additional information may be found in Wang, Z. L. *Reflection Electron Microscopy and Spectroscopy for Surface Analysis*, Cambridge University Press: Cambridge, UK, 1996. (A book synopsis is found online at: http://www.nanoscience.gatech.edu/zlwang/book/book2_intro.pdf)

[42] For a thorough summary/examples of the details generated from EELS spectra, see: (a) Thomas, J. M.; Williams, B. G.; Sparrow, T. G. *Acc. Chem. Res.* **1985**, *18*, 324. (b) http://quasi.nims.go.jp/hrtem/recent/eels-e.html.

[43] (a) Williams, B. G.; Sparrow, T. G.; Egerton, R. F. *Proc. R. Soc. Lond. Ser. A* **1984**, *393*, 409. (b) Sparrow, T. G.; Williams, B. G.; Thomas, J. M.; Jones, W.; Herley, P. J.; Jefferson, D. A. *J. Chem. Soc., Chem. Commun.* **1983**, 1432. (c) Ferrell, R. A. *Phys. Rev.* **1956**, *101*, 554.

[44] For example, see: http://ipn2.epfl.ch/CHBU/papers/ourpapers/Stockli_ZPD97.pdf

[45] A very nice tutorial on XANES and XAFS is found online at: http://cars9.uchicago.edu/xafs/xas_fun/xas_fundamentals.pdf

[46] (top) Reproduced with permission from Gerald Kothleitner (http://www.felmi-zfe.at), *Electron Energy-Loss Spectroscopy (EELS) for the Hitachi HD-2000,* found online at: www.cs.duke.edu/courses/spring04/cps296.4/papers/EELS.method.pdf (bottom) Reproduced with permission from Brydson, R. *Electron Energy Loss Spectroscopy*, BIOS Scientific Publishers: Oxford, UK. Copyright 2001 Taylor & Francis Group.

[47] For a recent application of EELS in determining the nature of C bonding in amorphous carbon nanotubes see: Hu, Z. D.; Hu, Y. F.; Chen, Q.; Duan, X. F.; Peng, L. -M. *J. Phys. Chem. B.* **2006**, *110*, 8263.

[48] For information on the analysis of surfaces by IR radiation instead of electrons, a complimentary technique known as reflection absorption infrared spectroscopy (RAIRS), see: (a) http://www.uksaf.org/tech/rairs.html (b) http://www.cem.msu.edu/∼cem924sg/Topic11.pdf

[49] For example, the development of fibers/fabrics that will actively adsorb and surface deactivate chemical and biological warfare agents – of increasing importance as new modes of terrorist activity continue to emerge. For more information, see: (a) http://web.mit.edu/isn/(Institute of Soldier Nanotechnologies at M.I.T.). (b) Richards, V. N.; Vohs, J. K.; Williams, G. L.; Fahlman, B. D. *J. Am. Ceram. Soc.* **2005**, *88*, 1973.

[50] Simon, C.; Walmsley, J.; Redford, K. *Transmission Electron Microscopy Analysis of Hybrid Coatings*, Proceedings of the 6th International Congress on Advanced Coating Technology, Nuremberg, Germany, April 3–4, 2001. Found online at: http://www.sintef.no/content/page1___5524.aspx

[51] Some of the (potential) energy of the incident electrons is required to release an outer electron from its valence or conduction band, with the remaining being transferred into the kinetic energy of the ejected secondary electron.

[52] For more details, refer to: Goldstein, J.; Newbury, D.; Joy, D.; Lyman, C.; Echlin, P.; Lifshin, E.; Sawyer, L.; Michael, J. *Scanning Electron Microscopy and X-Ray Microanalysis*, 3rd ed., Kluwer: New York, 2003.

[53] For example, see: http://www.edax.com/products/TSL/OIM/OIM-Intro.html

[54] Monte Carlo simulations performed by the author using the program CASINO ("monte CArlo SImulation of electroN trajectory in sOlids"), available free-of-charge on the Internet: http://www.gel.usherbrooke.ca/casino/What.html

[55] Both carbon and gold coating are performed using a sputter-coating PVD method. The film of choice is most often C since it is less costly and is transparent to X-rays (for EDS). Gold is used to coat very uneven surfaces, and is only useful when EDS is not being performed (strong Au signal would mask other elements present in the sample).

[56] An example of a tandem SEM/SAM instrument is the Thermo Microlab 350: http://www.thermo.com/com/cda/product/detail/1,1055,15886,00.html

[57] The effect of charging can be controlled by either altering the position of the sample with regard to the incident electron beam, or using an argon ion (Ar^+) gun to neutralize the charge.

[58] For a historical background of ESEM development, see: http://www.danilatos.com/

[59] For instance, see: (a) http://www.feicompany.com/Portals/_default/PDFs/content/2006_06_SetSTEM_td.pdf (b) http://www.feicompany.com/Products/ProductTypes/SEM/tabid/67/Default.aspx

[60] The SEM image of charging was taken from unpublished work by the author. The gold-coated SEM image is also from the author's research: Vohs, J. K.; Raymond, J. E.; Brege, J. J.; Williams, G. L.; LeCaptain, D. L.; Roseveld, S.; Fahlman, B. D. *Polym. News* **2005**, *30*(10), 330.

[61] Richards, V. N.; Vohs, J. K.; Williams, G. L.; Fahlman, B. D. *J. Am. Ceram. Soc.* **2005**, *88*(7), 1973.

[62] Auger spectra reproduced with permission from Zhu, Z.; Srivastava, A.; Osgood, R. M. *J. Phys. Chem. B* **2003**, *107*, 13939. Copyright 2003 American Chemical Society.

[63] Auger depth profile reproduced with permission from Zhang, Y. W.; Yang, Y.; Jin, S.; Tian, S. J.; Li, G. B.; Jia, J. T.; Liao, C. S.; Yan, C. H. *Chem. Mater.* **2001**, *13*, 372. Copyright 2001 American Chemical Society.

[64] Schematic reproduced with permission from Miller, A. F.; Cooper, S. J. *Langmuir* **2002**, *18*, 1310. Copyright 2002 American Chemical Society.

[65] Reproduced with permission from Rossi, M. P.; Ye, H.; Gogotsi, Y.; Babu, S.; Ndungu, P.; Bradley, J. -C. *Nano Lett.* **2004**, 4, 989. Copyright 2004 American Chemical Society.

[66] In contrast to SEM, EDS, and AES that use incident X-rays of *ca*. 10 keV, XPS is less damaging to beam-sensitive samples due to the use of "soft" X-rays, of much less energy (1–1.5 keV).

[67] A very detailed example of XPS to distinguish among Li salts for Li-ion battery applications is: Dedryvere, R.; Leroy, S.; Martinez, H.; Blanchard, F.; Lemordant, D.; Gonbeau, D. *J. Phys. Chem. B* **2006**, *110*, 12986.

[68] (a) As you may recall from Chapter 4, the energy bands of crystalline solids (*e.g.*, semiconductors) are denoted as parabolas in an E–k diagram, where momentum (p) is equal to ηk. Interactive E–k diagrams for SiGe and AlGaAs are found online (respectively) at: (i) http://jas.eng.buffalo.edu/education/semicon/SiGe/index.html (ii) http://jas.eng.buffalo.edu/education/semicon/AlGaAs/ternary.html (b) In addition to angle-resolve PES, *photoluminescence spectroscopy* is typically used as a nondestructive means to delineate the electronic properties of materials. For more information, see: (i) http://www.nrel.gov/measurements/photo.html (ii) Glinka, Y. D.; Lin, S. -H.; Hwang, L. -P.; Chen, Y. -T. *J. Phys. Chem. B* **2000**, 104, 8652. (iii) Wu, J.; Han, W. -Q.; Walukiewicz, W.; Ager, J. W.; Shan, W.; Haller, E. E.; Zettl, A. *Nano Lett.* **2004**, 4, 647.

[69] Synchrotron radiation is generated by the acceleration of ultrarelavistic (*i.e.*, moving near the speed of light) electrons through magnetic fields. This is accomplished by forcing the electrons to repeatedly travel in a closed loop by strong magnetic fields. The resulting radiation is orders of magnitude more intense than X-rays generated from X-ray tubes, and is widely tunable in energy (from <1 eV to MeVs). A popular source is the National Synchrotron Light Source (NSLS) at Brookhaven National Laboratory, Upton, NY. A Si(111) crystal monochromator is typically used to vary the photon energy incident to the sample.

[70] For an application example of EXAFS, see: Borgna, A.; Stagg, S. M.; Resasco, D. E. *J. Phys. Chem. B* **1998**, *102*, 5077. An example of XPS and XAFS (XANES and EXAFS), see: Chakroune, N.; Viau, G.; Ammar, S.; Poul, L.; Veautier, D.; Chehimi, M. M.; Mangeney, C.; Villain, F.; Fievet, F. *Langmuir* **2005**, *21*, 6788.

[71] For an application example of REFLEXAFS, see: d'Acapito, F.; Emelianov, I.; Relini, A.; Cavotorta, P.; Gliozzi, A.; Minicozzi, V.; Morante, S.; Solari, P. L.; Rolandi, R. *Langmuir* **2002**, *18*, 5277.

[72] Gervasini, A.; Manzoli, M.; Martra, G.; Ponti, A.; Ravasio, N.; Sordelli, L.; Zaccheria, F. *J. Phys. Chem. B* **2006**, *110*, 7851.

[73] Data analysis represents the most essential and time-consuming aspects of these techniques (as well as EELS). Typically, sample spectra are compared to reference samples that contain the probed element with similar valences and bonding motifs. In this example, Cu metal foil was used for the Cu-Cu interactions, and CuO/Cu_2O were used for the Cu-O contributions. A variety of software programs are used for detailed curve-fitting, in order to obtain information regarding the chemical environment of the sample. For example, see: (a) http://cars9.uchicago.edu/~ravel/software/Welcome.html (b) http://www.dragon.lv/eda/ (c) http://www.aecom.yu.edu/home/csb/exafs.htm (d) http://www.xsi.nl/software.html (e) http://www.xpsdata.com/

[74] For information regarding the quantum mechanical description of spin–orbit splitting, see: (a) http://hyperphysics.phy-astr.gsu.edu/hbase/quantum/sodzee.html#c1 (b) http://www.technology.niagarac.on.ca/people/mcsele/lasers/Quantum.htm (c) http://gardenofdestiny.com/Physics%20of%20Destiny.htm

[75] The presence of these satellites are indicative of Cu^{2+}. For instance, see: (a) Espinos, J. P.; Morales, J.; Barranco A.; Caballero, A.; Holgado, J. P.; Gonzalez-Elipe, A. R. *J. Phys. Chem. B* **2002**, *106*, 6921. (b) Morales, J.; Caballero, A.; Holgado, J. P.; Espinos, J. P.; Gonzalez-Elipe, A. R. *J. Phys. Chem. B* **2002**, *106*, 10185. (c) Fuggle, J. C.; Alvarado, S. F. *Phys. Rev. A* **1980**, *22*, 1615 (describes the cause of peak broadening in XPS spectra, related to core-level lifetimes).

[76] Many references exist for MIES studies of surfaces, most often carried out in tandem with UPS (to gain information for both the surface and immediate subsurface of the sample). For example, see: (a) Johnson, M. A.; Stefanovich, E. V.; Truong, T. N.; Gunster, J.; Goodman, D. W. *J. Phys. Chem. B* **1999**, *103*, 3391. (b) Kim, Y. D.; Wei, T.; Stulz, J.; Goodman, D. W. *Langmuir* **2003**, *19*, 1140 (very nice work that describes the shortfall of UPS alone, and the utility of a tandem UPS/MIES approach).

[77] Though conventional RBS is carried out with He^{+} ions (which will backscatter from any atom with a greater Z), heavier ions such as C, O, Si, or Cl may be used in order to prevent background backscattering interactions with the matrix. For example, use of incident O ions to eliminate backscattering from lattice O atoms for the RBS analysis of ceramic oxides.

[78] Simulations for ion scattering techniques such as RBS are typically compared with actual spectra in order to characterize the surface features. There are many such algorithms; for example: (a) Kido, Y.; Koshikawa, T. *J. Appl. Phys.* **1990**, *67*, 187. (b) Doolittle, L. R. *Nucl. Instrum. Methods* **1986**, *B*15, 227 (RUMP program). (c) http://www.ee.surrey.ac.uk/SCRIBA/ndf/(Ion Beam DataFurnace). (d) http://www.ee.surrey.ac.uk/SCRIBA/ndf/publist.html (publications re RBS simulations). (e) http://www-iba.bo.imm.cnr.it/(a nice compilation of software for ion-beam analyses)

[79] http://en.wikipedia.org/wiki/Van_de_Graaff_generator. Manysuch systems exist; some examples include: (a) Western Michigan University (http://tesla.physics.wmich.edu/AcceleratorFacility.php?PG=1). (b) Brookhaven National Laboratory (http://tvdg10.phy.bnl.gov/index.html). (c) National Institute of Standards and Technology (NIST, http://physics.nist.gov/Divisions/Div846/Gp2/graaff.html). (d) Yale University (http://wnsl.physics.yale.edu/)

[80] Also known as forward recoil scattering (FRS) or hydrogen forward scattering (HFS).

[81] Naab, F. U.; Holland, O. W.; Duggan, J. L.; McDaniel, F. D. *J. Phys. Chem. B* **2005**, *109*, 1415, and references therein.

[82] For a very thorough web presentation regarding SIMS see: (a) http://www.eaglabs.com/en-US/presentations/TOFSIMS/Presentation_Files/index.html (b) http://www.eaglabs.com/en-US/research/research.html (other links to SIMS theory, applications, presentations)

[83] For background information and recipes to study a variety of polymers using MALDI, see: http://polymers.msel.nist.gov/maldirecipes/maldi.html

[84] For a thesis that has a nice background on ESI, see: http://www.diva-portal.org/diva/getDocument?urn_nbn_se_uu_diva-2605-1__fulltext.pdf

[85] Typically, the majority of secondary ions are ejected from the top two or three monolayers (10–20 Å) of the sample.

[86] For instance, the ion concentration of the impinging ion beam must be $<1\%$ of the number of surface molecules. If this "static limit" is breached, a residue from molecular fragmentation will build up on the surface, which depletes the signal.

[87] The use of fullerene ion sources represents an area of increasing interest. For example, see: Cheng, J.; Winograd, N. *Anal. Chem.* **2005**, *77*, 3651, and references therein.

[88] Winograd, N. *Anal. Chem.* **2005**, *77*, 142A.

[89] For example, see: (a) Delcorte, A.; Medard, N.; Bertrand, P. *Anal. Chem.* **2002**, *74*, 4955. (b) Delcorte, A.; Bour, J.; Aubriet, F.; Muller, J. -F.; Bertrand, P. *Anal. Chem.* **2003**, *75*, 6875.

[90] Marcus, A.; Winograd, N. *Anal. Chem.* **2006**, *78*, 141.

[91] Images reproduced with permission from Kim, Y. -P.; Oh, E.; Hong, M. -Y.; Lee, D.; Han, M. -K.; Shon, H. K.; Moon, D. W.; Kim, H. -S.; Lee, T. G. *Anal. Chem.* **2006**, *78*, 1913. Copyright 2006 American Chemical Society.

[92] Images reproduced with permission from Verlinden, G.; Janssens, G.; Gijbels, R.; Van Espen, P. *Anal. Chem.* **1997**, *69*, 3772. Copyright 1997 American Chemical Society.

[93] It should be noted that near-field scanning optical microscopy (NSOM) (discussed at the beginning of this chapter) is often grouped alongside other SPM techniques. However, for our discussion, we will focus on AFM and STM since these use *physical* probes to interrogate a surface, rather than focused light.

[94] For example, see: Zhang, J.; Chi, Q.; Ulstrup, J. *Langmuir* **2006**, *22*, 6203.

[95] For example, see: (a) France, C. B.; Frame, F. A.; Parkinson, B. A. *Langmuir* **2006**, *22*, 7507. (b) Li, W. -S.; Kim, K. S.; Jiang, D. -L.; Tanaka, H.; Kawai, T.; Kwon, J. H.; Kim, D.; Aida, T. *J. Am. Chem. Soc.* **2006**, *128*, 10527. (c) Namai, Y.; Matsuoka, O. *J. Phys. Chem. B* **2006**, *110*, 6451.

[96] For a recent precedent, see: Park, J. B.; Jaeckel, B.; Parkinson, B. A. *Langmuir* **2006**, *22*, 5334, and references therein. For a thorough recent review, see: Wan, L. -J. *Acc. Chem. Res.* **2006**, *39*, 334.

[97] For example, see: Alam, M. S.; Dremov, V.; Muller, P.; Postnikov, A. V.; Mal, S. S.; Hussain, F.; Kortz, U. *Inorg. Chem.* **2006**, *45*, 2866.

[98] Examples of some common forces that may exist between a surface and an AFM tip are Van der Waal, electrostatic, covalent bonding, capillary, and magnetic. In addition to providing information regarding the topography of the surface (constant force mode), forces may be applied to understand the morphology of a surface – for example, to determine the frictional force between the tip and surface, or the elasticity/hardness of a surface feature. For instance, see: Tranchida, D.; Piccarolo, S.; Soliman, M. *Macromolecules* **2006**, *39*, 4547, and references therein.

[99] For example, see: O'Dwyer, C.; Gay, G.; Viaris de Lesegno, B.; Weiner, J. *Langmuir* **2004**, *20*, 8172, and references therein.

[100] For a more sophisticated commercial liquid cell AFM system, see: http://www.veeco.com/escope

[101] For example, see: (a) Cho, Y.; Ivanisevic, A. *Langmuir* **2006**, *22*, 1768. (b) Poggi, M. A.; Lillehei, P. T.; Bottomley, L. A. *Chem. Mater.* **2005**, *17*, 4289. (c) Gourianova, S.; Willenbacher, N.; Kutschera, M. *Langmuir* **2005**, *21*, 5429.

[102] For example, see: (a) Takamura, Y.; Chopdekar, R. V.; Scholl, A.; Doran, A.; Liddle, J. A.; Harteneck, B.; Suzuji, Y. *Nano Lett.* **2006**, 6, 1287. (b) Li, Y.; Tevaarwerk, E.; Chang, R. P. H. *Chem. Mater.* **2006**, *18*, 2552.

[103] For example, see: Zhang, J.; Roberts, C. J.; Shakesheff, K. M.; Davies, M. C.; Tendler, S. J. B. *Macromolecules* **2003**, *36*, 1215, and references therein.

[104] For a thorough description of SECM, see: Gardner, C. E.; Macpherson, J. V. *Anal. Chem.* **2002**, *74*, 576A.

[105] For instance, see: https://www.veecoprobes.com/probes.asp

[106] (a) Nanoparticle-terminated tips: Reproduced with permission from Vakarelski, I. U.; Higashitani, K. *Langmuir* **2006**, *22*, 2931. Copyright 2006 American Chemical Society. (b) Nanotube-terminated tips: Reproduced with permission from Hafner, J. H.; Cheung, C. -L.; Oosterkamp, T. H.; Lieber, C. M. *J. Phys. Chem. B* **2001**, *105*, 743. Copyright 2001 American Chemical Society. (c) Nanotube-terminated tips: Wilson, N. R.; Macpherson, J. V. *Nano Lett.* **2003**, *3*, 1365.

[107] That is, an AFM probe responds to the *average* force between the sample surface and a group of tip atoms that are in close proximity to the surface. In order to image individual atoms by SPM, the surface–tip interactions must be limited to the nearest atom(s) on the tip periphery. Hence, an AFM image will not show individual atoms, but rather an average surface, with its ultimate resolution dependent on the sharpness of the tip structure. In contrast, STM is capable of atomic resolution since the tunneling current passes only through the tip atom that is nearest the sample surface.

[108] Named after Brunauer, Emmett, and Teller.

[109] For example, see: Gillan, E. G.; Bott, S. G.; Barron, A. R. *Chem. Mater.* **1997**, *9*, 796.

[110] Tandem TGA/DSC instruments are commercially available, for example: http://www.tainst.com/product.aspx?n=1&id=22

[111] An analogous (older) technique is known as *differential thermal analysis* (DTA), which yields the same information as DSC.

[112] For more information on small-angle scattering, see: (a) http://www.isis.rl.ac.uk/largescale/loq/documents/sans.htm (b) http://www.eng.uc.edu/~gbeaucag/Classes/XRD/SAXS%20Chapter/SAXSforXRD.htm

[113] Schematics (a) and (b) were obtained from the public domain from the website: http://en.wikipedia.org/wiki/Differential_scanning_calorimetry

[114] For a nice example that utilizes SAXS, WAXS, and SANS to determine the structural changes of polyethylene chains following annealing, see: Men, Y.; Rieger, J.; Lindner, P.; Enderle, H. -F.; Lilge, D.; Kristen, M. O.; Mihan, S.; Jiang, S. *J. Phys. Chem. B* **2005**, *109*, 16650.

[115] For an example of a quantitative SAXS study of a block copolymer-solvent system see: Soni, S. S.; Brotons, G.; Bellour, M.; Narayanan, T.; Gibaud, A. *J. Phys. Chem. B* **2006**, *110*, 15157. An example of the use of SAXS to determine the particle size distribution of nanoparticles, see: Rieker, T.; Hanprasopwattana, A.; Datye, A.; Hubbard, P. *Langmuir* **1999**, *15*, 638.

Topics for Further Discussion

1. In our discussion of sample staining for TEM analysis, we mentioned that lead citrate was sensitive to CO_2. What is the balanced reaction for generation of the side-product?
2. What is the difference between XPS and AES?
3. What characterization techniques would be best suited for the following:
   (a) Analysis of a thin film (20 nm thickness) for Na content (very precise value is desired).
   (b) Determination of the Li content of a thin film – comparison of the surface concentration with the Li content at a depth of 100 nm below the surface (diffusion study).
   (c) To image and study the desorption mechanism of SAMs from the surface of Au(111) upon exposure to organic solvents.
   (d) Characterize the film resulting from an attempt to covalently graft poly (ethylene glycol) (PEG) chains on poly(ethylene-*co*-acrylic acid) (EAA) surfaces.
   (e) Characterize the intermediate structures present on a thin film during CVD, at various deposition times.
   (f) Assess whether a new synthetic procedure to grow TiO_2 nanoparticles was successful or not.
   (g) Determine the lattice parameters of metallic ReO_3 nanoparticles.
   (h) Determine the percentage yield and purity for a batch of single-walled carbon nanotubes.
4. What are the differences between STM and AFM, providing examples of their applications?
5. How would you eliminate the presence of "nanobubbles" on Au surface during AFM imaging? Why is the presence of such adsorbates problematic for SPM studies? (hint: see *Langmuir* **2003**, *19*, 10510).
6. What are the benefits of using a liquid cell for AFM studies? Are there any limitations of this technique?
7. What is SECM, and what applications would this technique be used for?
8. Describe what is meant by "charging" during SEM analyses, along with methods that are used to circumvent these effects.
9. Why is the yield of Auger electrons most prevalent for elements with low-Z, relative to heavier elements (where X-ray emission is preferred)?
10. Find literature references for tandem UPS/XPS studies of surfaces. What information is gained from each technique?
11. What techniques are used to prepare thin sample sections for TEM analysis?
12. Find literature precedents for tandem RBS/PIXE surface characterization. What information does each technique yield?
13. What are the differences between EDS and WDS?
14. Why does one need a synchrotron source in order to perform XAFS studies?
15. The Getty museum in Los Angeles has contracted your services to determine if a Monet they recently received is authentic. What techniques, including sample preparation, *etc*. would you use to determine the authenticity of this artwork (handle it carefully!)?
16. You have just discovered a new method to grow carbon nanotubes at incredibly low temperatures. The FESEM and TEM images suggest that the as-grown nanostructures are graphitic, and exhibit very desirable aspect ratios. What other characterization techniques should you perform to fully characterize your product? How would you study the growth mechanism (*in situ* and/or by stopping

the growth at varying stages of growth), assuming that you used a CVD-type reaction with an iron-based nanoparticulate catalyst, at a temperature of 200°C?

17. You have been contracted to design a new polymer that will change its structure in response to temperature changes. What methods would you use to characterize your polymer following its synthesis?
18. You have grown an oxidizable metallic thin film, but must handle it briefly in air before sealing it in a storage container. How would you evaluate the thickness of the native surface oxide, and how deep the oxide diffuses into the thin film, as the sample is annealed?

Further Reading

1. Flegler, S. L.; Heckman, J. W.; Klomparens, K. L. *Scanning and Transmission Electron Microscopy: An Introduction*, W. H. Freeman: New York, 1993.
2. Williams, D. B.; Carter, C. B. *Transmission Electron Microscopy: A Textbook for Materials Science*, Plenum Press: New York, 1996.
3. Egerton, R. F. *Physical Principles of Electron Microscopy: An Introduction to TEM, SEM, and AEM*, Springer: New York, 1986.
4. Goldstein, J.; Newbury, D.; Joy, D.; Lyman, C.; Echlin, P.; Lifshin, E.; Sawyer, L.; Michael, J. *Scanning Electron Microscopy and X-Ray Microanalysis*, 3rd ed., Kluwer: New York, 2003.
5. *Encyclopedia of Materials Characterization – Surfaces, Interfaces, Thin Films*, Brundle, C. R.; Evans, C. A.; Wilson, S. eds., Elsevier: New York, 1992.
6. Campbell, D.; Pethrick, P. A.; White, J. R. *Polymer Characterization*, 2nd ed., Stanley Thornes: Cheltenham, UK, 2000.
7. Criddle, W. J.; Ellis, G. P. *Spectral and Chemical Characterization of Organic Compounds: A Laboratory Handbook*, 3rd ed., Wiley: New York, 1990.
8. Dinardo, N. J. *Nanoscale Characterization of Surfaces and Interfaces*, 2nd ed., Wiley: New York, 2004.
9. *Surface Characterization: A User's Sourcebook*, Brune, D.; Hellborg, R.; Hunderi, O. eds., Wiley: New York, 1997.
10. *Beam Effects, Surface Topography, and Depth Profiling in Surface Analysis (Methods of Surface Characterization)*, Czanderna, A. W.; Madey, T. E.; Powell, C. J. eds., Plenum Press: New York, 1998.
11. *Ion Spectroscopies for Surface Analysis (Methods of Surface Characterization)*, Czanderna, A. W.; Hercules, D. M. eds., Springer: New York, 1991.
12. Brandon, D. D.; Kaplan, W. D. *Microstructural Characterization of Materials*, Wiley: New York, 1999.
13. Pecharsky, V.; Zavalij, P. *Fundamentals of Powder Diffraction and Structural Characterization of Materials*, Springer: New York, 2005.
14. *Concise Encyclopedia of Materials Characterization*, 2nd ed., Cahn, R. ed., Elsevier: San Diego, CA, 2005.
15. *Characterization of Polymers (Materials Characterization)*, Tong, H. -M.; Kowalczyk, S. P.; Saraf, R.; Chou, N. J. eds., Butterworth-Heinemann: New York, 1993.